Politecnico di Torino

ScuDo
Scuola di Dottorato ~ Doctoral School
WHAT YOU ARE, TAKES YOU FAR

Doctoral Dissertation
Doctoral Program in Metrology (36^{th}cycle)

Imaging techniques: new perspectives for the conservation of metallic artefacts

By

Amina Vietti

******

Supervisors:
Prof. Nicola Donato, Supervisor
Dr. Luca Lombardo, Co-Supervisor

Doctoral Examination Committee:
Prof. Yuval Goren, Referee, Ben Gurion University of the Negev, Beer-Sheva, Israel
Prof. Anna Gueli , Referee, Università degli Studi di Catania, Italy
Prof. Attilio Di Nisio, Politecnico di Bari, Italy
Prof. Mirko Marracci, Università di Pisa, Italy
Prof. Guido Perrone, Politecnico di Torino, Italy

Politecnico di Torino
2024

Declaration

I hereby declare that, the contents and organization of this dissertation constitute my own original work and does not compromise in any way the rights of third parties, including those relating to the security of personal data.

Amina Vietti
2024

* This dissertation is presented in partial fulfillment of the requirements for **Ph.D. degree** in the Graduate School of Politecnico di Torino (ScuDo).

In loving memory of my father, who always believed in me.
Until the end.

Acknowledgements

I would like to thank all those who have contributed to this three-year research project with their support, guidance, and encouragement. Without that, this work would not have been possible.

First and foremost, I would like to express my deepest and sincere gratitude to my supervisor, Professor Nicola Donato, who always supported my research activity.

Furthermore, I am deeply thankful to my co-supervisor, Dr. Luca Lombardo, for his mentorship, guidance and valuable suggestions during these three years.

I am sincerely thankful to all the people involved in the INFN-NICHE project. I am deeply grateful to Professor Alessandro Re and Professor Alessandro Lo Giudice (University of Torino) for their assistance and for allowing me to closely follow the progress of the project at the LENA Centre of Pavia. I would like to extend my gratitude to Dr. Francesco Grazzi and Dr. Nicla Gelli, project referents, for their insightful feedback and valuable suggestions during the development of the system and, mostly, for the interpretation of the data. I would like to mention also the staff and resources of the LENA Centre of Pavia for their assistance and access to the facility.

I am also grateful to Professor Paolo Matteis (Politecnico di Torino), who facilitated the execution of this research project, allowing me to use all the metallurgy laboratory equipment to prepare the samples for the metallographic attacks.

I would like to sincerely thank Associazione Italiana di Archeometria for awarding me the "Sportello Giovani grant". The grant partially covered the expenses for participating in the *International Conference on Metrology for Cultural Heritage - MetroArchaeo 2022* held in Rende - Università della Calabria, to share the preliminary results of my research activity with the presentation entitled 'Neutron Imaging for the characterization of Cu-based artefacts'.

I am immensely thankful to my academic advisors, mentors, and collaborators for their invaluable guidance. In particular, I would like to thank Professor Marco Parvis, Professor Emma Angelini and Professor Sabrina Grassini of the COMETA group of the Politecnico di Torino. Their wisdom and expertise have enriched my research activities and propelled me towards the achievement of my research goals. Thank you for the immense opportunity given three years ago.

Lastly, I am grateful to all my colleagues who have provided valuable insights, discussions, and assistance throughout this 3-years journey. Their support has been a source of strength and motivation. I am grateful for all the fun times, the dinners, the conferences, the journeys, the anxiety about deadlines, the moments of discouragement, and the long sleepless nights before the presentations. I will cherish every memory. Some colleagues did not remain simply colleagues but became real friends that I will carry in my heart forever.

I extend my sincere gratitude to my family for their unwavering love, encouragement, and support during these challenging three years.

Thanks to everyone who has been part of this crazy journey.

Abstract

Measurements and Metrology for Cultural Heritage applications must satisfy several requirements (e.g. not invasive, not destructive, low-cost, portable, versatile, etc) making therefore the multidisciplinary approach fundamental. Collaborations among scientists, conservators, archaeologists, and experts in the field of measurement are driving continuous innovation in diagnostic techniques improving resolution, accessibility, experimental methodologies, and data analysis. In this scenario, Imaging techniques play an important role in the diagnostic of Cultural Heritage by providing non-invasive and non-destructive insights into artefacts' composition, structure, and conservation state.
Two main issues were addressed in the dissertation. The first one was the calibration and characterization of the first Neutron Imaging apparatus dedicated to the study of Cultural Heritage objects in Italy. Moreover, developing and validating a low-cost and portable device for UV and VIS Reflectance Transformation Imaging was the second issue. The final main application is devoted to the characterization of metallic archaeological artefacts. These two imaging techniques permit the acquisition of information about the metallic samples in a non-invasive and non-destructive way which is one of the most important requirements for Cultural Heritage diagnostic.

Concerning the Neutron Imaging, a set of copper-based reference samples were produced and characterized in laboratory to calibrate a Neutron Imaging setup. The obtained results are very promising, especially regarding the alloy characterization while further studies are still necessary to identify the corrosion patina. In this perspective, a visible and ultraviolet Reflectance Transformation Imaging (RTI) system was developed to have a portable and low-cost device for the study of the corrosion patina. The simultaneous acquisition of UV and VIS images allows to obtain information both on the surface morphology and the chemical composition of the corrosion products.

Contents

Preface

The research has been focused on the optimization of imaging techniques for the study and characterization of metal artefacts. The potential of two imaging techniques, which can be almost considered complementary in terms of achievable results, was explored: Absorption Contrast Neutron Imaging, a complex technique that provides information regarding the bulk composition of the object under examination, and Reflectance Transformation Imaging (RTI), which is instead a rather simple technique that provides information of the artefact surface.

Most of the work was dedicated to the calibration of a Neutron Imaging station dedicated to the study of Cultural Heritage at the LENA Applied Nuclear Energy Laboratory in Pavia (Italy). The main aim was to provide a set of reference alloys with known chemical composition and microstructure similar to ancient metal artefacts to be able to correlate the information obtained from the image processing, in particular the mass attenuation coefficient, with the composition of the alloy. In fact, having an instrument that allows alloy discrimination would be an important upgrade in the characterization of metals by using neutrons. As will be fully explained in the next chapters, the use of neutrons presents several advantages. In particular, neutrons can penetrate heavy metals (i.e. lead) and can discriminate elements not otherwise discriminable with other techniques. Neutron Imaging is a non-invasive and non-destructive technique which represents a valuable complement and alternative to conventional X-Ray imaging.

The obtained results of the calibration turned out to be quite promising, especially in the discrimination of alloys made up of percentages of different elements (i.e. brass, tin bronze, leaded tin bronze). Additionally, an attempt was made to study the corrosion patina formed on the metallic surface. For this purpose, some metallic references were selected to be artificially aged to obtain corrosion product layers on the surface. The discrimination of the composition of the corrosion products layers

is also a challenge in the safeguarding of metallic objects. In particular, in the case of Cu-based artefacts, corrosion patinas have to be preserved for historical and aesthetic reasons. Implementing the Neutron Imaging resolutions is therefore a fundamental issue.

In advance of the application of Neutron Imaging to historical metal artefacts, it will be necessary to take into consideration the strict radioprotection rules which provide mandatory quarantine (six months) for samples potentially activated by the neutron beam. Until now, this is one of the biggest problems evidenced in anticipation of using this technique with real metal artefacts. Despite this, the calibration was carried out to implement the Neutron Imaging facility.

Eventually, for the study of the morphology, an RTI system was developed in parallel to provide information about the surface. Since Neutron Imaging was unable to provide the necessary information regarding the superficial corrosion layer of the sample, the development of a system that allows the morphological and compositional analysis of the corrosion products became necessary. In this way, it was developed a portable and low-cost system for the characterization of small-sized metal artefacts, to simultaneously obtain morphological and compositional information. This was done by pairing two different types of lighting: visible and ultraviolet. In this way, the acquisition of RTI images in the visible and UV can provide a first characterization of a sample in a totally non-invasive way.

The VIS-UVL RTI system was tested for the analysis of some bronze coins, therefore carrying out an initial chemical characterization using Raman spectroscopy and then comparing the results with the appearance of the surface (more or less fluorescent areas). Even in this case, the results were promising, as will be better explained in the following chapters.

Finally, these two techniques, so different from each other in terms of instrumentation, cost and above all achievable results, appear to be almost complementary. They have proven to be very useful in the characterization of metal artefacts, providing a generally non-invasive and non-destructive tool for the study and conservation of metals. The role of the measurement expert is therefore fundamental in attempting to improve the current limitations so that they can effectively be two independent techniques that can be used in an independent way.

Some case studies were also followed to develop measurement protocols devoted to the study of iron metallic artefacts using Raman spectroscopy. In the first case

study, a protocol was developed and tested on archaeological iron nails to study the corrosion product layers and provide information about the conservation state. The second case study involved the evaluation of long-term effectiveness of different protective treatments applied to archaeological iron nails.

Following this short preface, the outline of the work is briefly presented below:

- **Chapter 1** - This chapter presents a brief overview regarding the measurements for Cultural Heritage, providing details on the difference between non-invasive and non-destructive techniques and focusing the attention on the use of Imaging techniques.
- **Chapter 2** - This chapter provides basic information about Absorption Contrast Neutron Imaging and then the calibration of the proposed system is discussed.
- **Chapter 3** - This chapter describes the Reflectance Transformation Imaging technique and illustrates the developed system, discussing the obtained results.
- **Chapter 4** - This chapter presents some case studies devoted to the development of measurement protocols to characterize artefacts with Raman spectroscopy.
- **Chapter 5** - This last chapter summarises the obtained results of the research activity, in the perspective of conservation of metallic artefacts. The main contributions and the possible future work will presented.

List of Figures

List of Tables

Chapter 1

Introduction

This introductory chapter will present some fundamentals related to measurements and metrology in the Cultural Heritage field. In particular, the requirements that the analytical techniques must satisfy and the protocols used for the analyses will be explained. Shortly after, an in-depth analysis of imaging techniques and metal artefacts, the subjects of the dissertation, will be presented in more detail.

1.1 Measurements for Cultural Heritage

Since the birth of diagnostic applied to Cultural Heritage, in the early twentieth century, it has been clear that many existing techniques could be suitable for the characterization and, in addition, the evaluation of the state of conservation of artefacts [1].

In particular, several techniques with different characteristics and purposes can be employed: spectroscopic techniques which exploit different wavelengths, or analytical methods which use radiation or particles, rather than gravimetric or electrical methods, based on particular effects of the interaction with the matter (such as Auger effect, photoelectric effect, diffraction, diffusion at different angles, etc.) [2].

It is clear how the role of Metrology acquires a fundamental position in the development of new technologies as well as the improvement of existing ones, thus making the multidisciplinary approach fundamental, seeing the close collaboration among scientists and curators [3]. In fact, when developing new techniques or

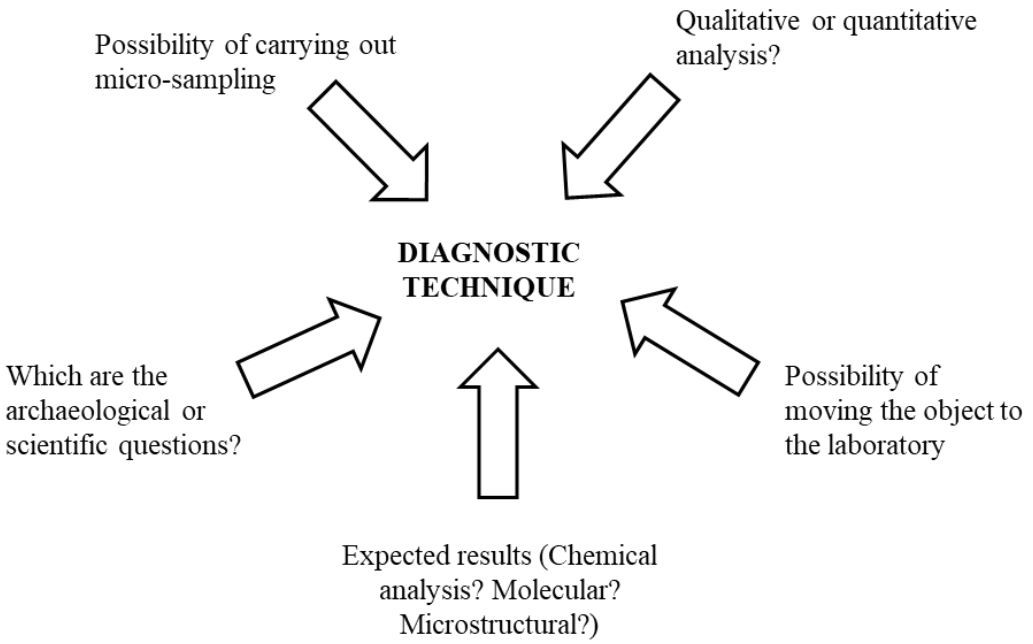

Fig. 1.1 Schematic diagram representing the path used for choosing the diagnostic technique

improving existing ones, it is necessary to take into account that the object of study generally needs to be preserved and, in most cases, does not allow the application of all existing analyses. This is because a diagnostic technique should satisfy some important requirements: it should be as less invasive as possible, non-destructive, possibly low-cost and portable but with high sensitivity and performance [4]. As will be explained later, it is not always easy to comply with all the requirements, so it is necessary to choose one or more techniques that give the best result while respecting the technical exigencies.

The choice of the analytical method always depends, unless there are other constraints (i.e. costs, times, availability), on different factors which in many cases can limit the choice. Below in Figure 1.1 is presented an example diagram of the diagnostic approach used in choosing the most suitable technique.

The technique should answer all the diagnostic questions. This is an important key point because the choice depends on the type of information it is possible to obtain [5]. A list of the major information that can be obtained from an analysis will be presented:

- Composition of the material: qualitative and quantitative analyses, elemental or molecular information;
- Physical characterization: measurement of physical properties of the material (i.e. conductibility, resistance, etc);
- Structure of the material: mineralogical characterization;
- Age of the sample: relative or absolute dating.

Unfortunately, there is no standard protocol and each case must be planned and deeply discussed before starting the analysis. As will be evident, the complementarity of the analyses is of great importance (i.e. the possibility of obtaining complementary results with different analytical methods) avoiding overlaps and redundancies as much as possible, unless they serve as verification of the limits of a methodology. As will be deeply presented below, for example, imaging techniques such as reflectography, radiography and UV analysis are basically complementary, rarely offering the same information: for this reason, only their integrated use, together with photographic recordings, can give back a complete vision of the studied object. Moreover, another aspect that is of fundamental importance is the level at which to carry out an analysis, from atomic level to macroscopic scale [5].

Above all, the choice often falls on the technique that provides better results with less effort. If possible, several measurement techniques are usually used at the same time to make up for some deficiencies or analytical limits. Therefore the analytical approach usually starts with completely non-invasive and non-destructive visual analyses (i.e. imaging), and then to non-destructive analyses (i.e. Raman spectroscopy, X-Ray Fluorescence, etc), and if necessary semi-invasive techniques that need a microsampling possibly from a strategic part (i.e. Chromatography, Scanning Electrons Microscope, etc) [4].

The terms used in the characterization of diagnostic techniques will be briefly explained. In particular, the differences between invasive and non-invasive and, furthermore, the definition of destructive and non-destructive techniques will be explained. A schematic representation of these definitions is presented in Figure 1.2.

Under the definition of **non-invasive** methods are grouped all the techniques that do not cause alteration in the object of analysis. These can be both mechanical

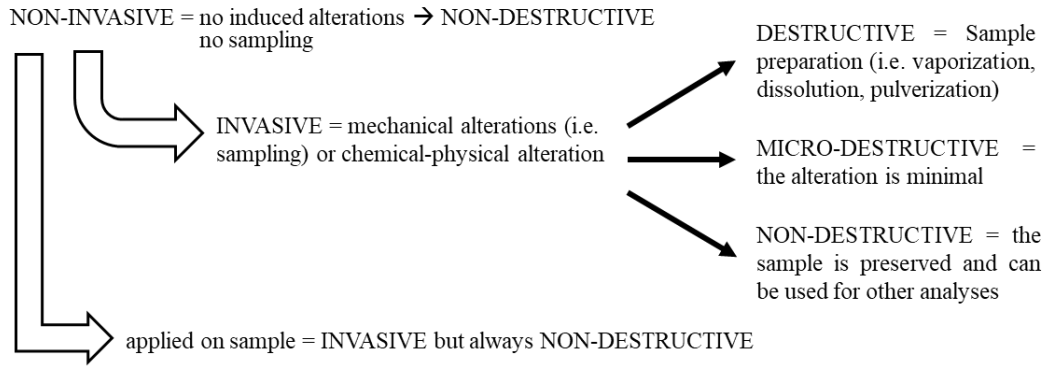

Fig. 1.2 Schematic representation of the difference between invasive, non-invasive, destructive and non-destructive techniques.

alterations (i.e. sampling) and chemical-physical alterations. This implies that a non-invasive method is, consequently, non-destructive. On the contrary, non-invasive analysis can become invasive if used for measurements on fragments and samples, however guaranteeing their non-destruction. Examples of non-invasive techniques are essentially imaging techniques, Raman spectroscopy, X-ray Fluorescence (XRF), and Infrared spectroscopy.

On the other hand, **invasive** methods alter the artefact or a part of it in some way as they involve a sampling, even if very modest. As mentioned above, the damage can be material or even before a variation in its chemical or physical structure, such as the creation of a cavity for internal inspections, the introduction of external materials, the breaking of chemical bonds and the production of molecules different from the original ones. Generally, invasive techniques requires micro samples. Furthermore, invasive methodologies may or may not be **destructive**, where destructive refers to the fact that the sample taken from the work is not preserved before and after the analysis, generally because the analytical procedure required sample preparation (i.e. pulverization, dissolution or vaporization) implying the sample can no longer be used for other analyses and sometimes not even to repeat the same one.

Examples of invasive analyses, because they operate on samples but not necessarily destructive, are optical microscopy on sections, Scanning Electron Microscopy (SEM) or intra-transmissions. Invasive and generally destructive are, for example, X-ray diffraction (XRD), which offers information on the crystalline structure (it requires the pulverization of the samples. Completely destructive are the so-called separation techniques, i.e. chromatography, in which the sample is studied after

separating the different chemical compounds, as happens with gas chromatography (GC) coupled with mass spectrometry (MS), a very powerful technique in identifying organic substances present in a sample, such as colorants of animal or vegetable origin and binder. Also completely destructive are atomic absorption (AAS) and emission spectroscopic (AES), and its ICP variant, which require the sample to be brought to a high temperature and atomized.

Micro-destructive analyses of the sample, sometimes also called micro-invasive, are those in which the alteration is minimal. For example, by making cavities of the order of hundreds of microns, as in the laser ablation techniques, in which a highly collimated high-power laser beam makes a microhole while the matter of the measurement point passes into the gaseous state and is studied through various possible atomic spectrometries that allow elemental analysis with very high precision.

It is therefore easily understandable that it is not always so simple to clearly categorise diagnostic techniques; in this scenario, the study and development of new technologies are of fundamental support to all the professionals involved in the characterization and diagnostic of Cultural Heritage.

To summarize, a hypothetical diagnostic protocol should start from a visual investigation which is non-invasive and non-destructive then continue towards microinvasive but non-destructive techniques with micro sampling, and conclude if necessary with destructive analysis.

1.1.1 Imaging techniques: state of the art

As discussed before, imaging techniques intended as visual investigation are part of the first step of characterising and analysing artefacts with historical and artistic interest. They are non-invasive and non-destructive and can provide a lot of information about: the constituent material, the chemical-physical properties, the internal structure, the preparatory layer or second thoughts in the paintings, and so on [6]. These techniques effectively return an image, either immediately or following scanning of the surface or volume under examination and subsequent processing. This means that they are widely used techniques, and, especially in recent years, they have undergone improvements to extend their applicability to a wider range of materials [7] [8]. The results obtained from this investigation can provide information about the production technique and everything that revolves around it (raw materials, trade

Image-based techniques	
Photographic methods	UV analyses (UVF, UVR)
Infrared reflectography (IRR)	3D laser scanner
Infrared false colour (IRFC)	Hyperspectral imaging (HSI)
Infrared thermography (IRT)	Multispectral imaging (MSI)
Terahertz imaging (THz-TDI)	X-ray radiography/tomography
Neutronic Activation autoradiography	Multibands imaging
Neutron radiography/tomography	Photogrammetry
Reflectance Transformation Imaging (RTI)	

Table 1.1 Selection of imaging techniques widely applied to the study of the Cultural heritage artefacts.

routes, technology), the conservation state and, above all, the characterization of the material in a non-invasive manner.

The use of imaging techniques in the study of Cultural Heritage has a long tradition. In fact, in many cases, the imaging techniques were already widely used for other purposes (for example X-Ray radiography in medicine [9]) and, thanks to technological advances, it was possible to adapt the instruments to a different use, therefore the application on artefacts [6]. The technical advancements in the technology, in sensors and instrumentation, have allowed to obtain numerous diagnostic techniques that permit the analysis of different objects and, moreover, buildings or architectural structures.

Some of the most used imaging techniques are listed in Table 1.1. As is apparent, the imaging techniques are numerous, and they differ from each other generally in the necessary instrumentation (some very expensive), in the type of information obtained from the analysis and, above all, in the type of artefact on which it can be applied.

Before introducing the most commonly used imaging techniques in the field of Cultural Heritage, it is important to underline the internal subdivision of imaging techniques which concerns the spectral band used, i.e. the regions of the electromagnetic spectrum in which the phenomena that each methodology exploits occur (Figure 1.3). Thus it is possible to distinguish analyses carried out in the visible, in the UV, in the x-Ray region, in the infrared or microwaves, and so on.

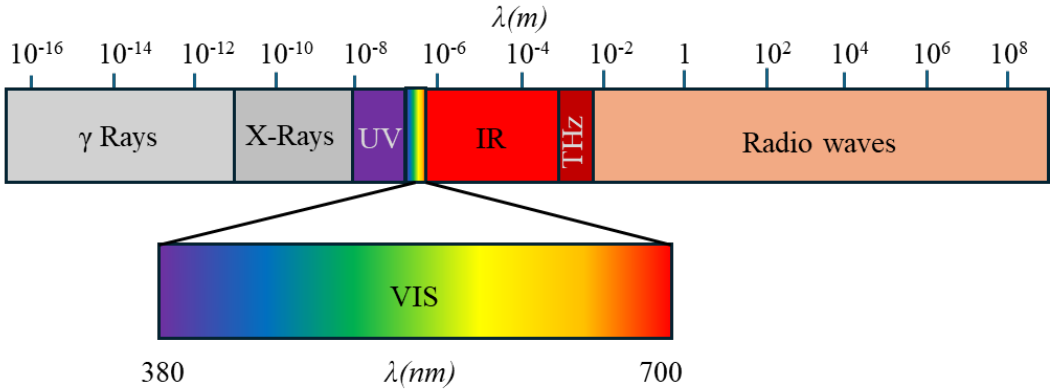

Fig. 1.3 Electromagnetic spectrum: fraction of interest for different imaging techniques for Cultural Heritage analysis.

In the interaction with matter, all incident electromagnetic radiation is absorbed, transmitted or reflected by the object, following the equation of energy conservation law:

$$A(\lambda)+R(\lambda)+T(\lambda)=I(\lambda) \tag{1.1}$$

where I(λ) is the incident radiation, A(λ) is the absorbed radiation, R(λ) is the reflected radiation and lastly T(λ) is the transmitted radiation. As it is evident, this phenomenon strictly depends on the material and, moreover, on wavelength (λ): this is why different imaging techniques are used in a complementary, exploiting different wavelengths to obtain complementary results [6]. However, some of the techniques mentioned above will be briefly presented. For further insights on imaging techniques, see [6] [8] [7].

- X-ray radiography and tomography: it is probably one of the oldest and most widely used imaging methods. It exploits the interaction of x-rays with matter, measuring their transmission which is inversely proportional to the density of the material. Some elements with high atomic numbers (e.g. Hg, Pb) almost completely block transmission and are therefore easily distinguishable, for example on paintings. Computed tomography also allows to study internal part of the object, obtaining a 3D model [10].

- Ultraviolet-induced Fluorescence (UVF): the fluorescence colour depends on the chemical nature of a material illuminated by UVs (λ = 100-400 nm); it is widely used for the distinction between organic and inorganic matter [11].
- Infrared Reflectography (IRR): it works with incandescent lamps which emit in the near-infrared region (λ = 0.7 - 1.1 *mu*m) and permits, for example, the identification of retouches or restoring layers [12];
- Infrared thermography (IRT): it exploits the response of an object to a thermal excitation, recording the different thermal diffusivity; it is widely used to study monuments and historical buildings [13];
- Photogrammetry: it uses the VIS light to obtain precise measurements and 3D models of objects from multiple overlapped photographs taken from different angles to reconstruct the geometry and spatial relationships of the photographed subject [14].
- Multispectral imaging (MSI): it can be considered as an extension of conventional photographic method, with a different acquisition range, which includes UV, VIS and IR [15];
- Hyperspectral imaging (HSI): it uses a broadband source which can illuminate the object, collecting several images at extended interval of wavelengths [16];
- Terahertz imaging (THz-TDI): Terahertz imaging is a technique used to capture and analyze electromagnetic radiation in the terahertz frequency range, which lies between the microwave and infrared regions of the electromagnetic spectrum [17].

The two techniques taken into consideration in this dissertation, Absorption Contrast Neutron Imaging and Reflectance Transformation Imaging, will be deeply presented in the following chapters. These two techniques are very different from each other, both in terms of costs and information obtainable. Despite this, these two techniques have almost been used in a complementary manner in the study of metal artefacts.

1.2 Metallic artefacts

Cultural Heritage metallic artefacts include a wide range of objects crafted from different metals throughout history, spanning various civilizations and cultural contexts. These artefacts provide tangible links to the past, offering insights into technological advancements, artistic expressions, religious practices, economic systems, and societal values. In this brief introduction, the significance of metal artefacts in Cultural Heritage will be explored, explaining why they are so important to be deeply studied, the challenges they present in terms of preservation and interpretation, and the classic methodologies used to characterize them.

Archaeometallurgy is a field that examines the metallic materials of the past, examining in depth all the aspects linked to production - from the extraction of the mineral to the final product - in relation to the historical, cultural and economic context of which they are expression [18]. The discovery of metals and the technologies for extracting them constitutes one of the crucial events in human history, comparable with the revolution constituted by the advent and spread of agriculture and livestock farming in the Neolithic age [19]. These technological advances created relationships between distant populations and different cultures. The presence of metal deposits has influenced the development of some regions, such as Nuragic Sardinia, as well as the location of settlements, which often arose in mining areas or in places where raw materials were exchanged[18].

A metal alloy is a substance composed of two or more metals (or a metal and usually a non-metal), that are combined to create a new material with enhanced properties [20]. These properties can include increased strength, durability, corrosion resistance, conductivity, or other desirable characteristics that may not be present in the individual metal. Alloys are typically created through processes such as melting, mixing, and solidification, resulting in a homogenous mixture of the constituent elements at the atomic level. Among the most widespread binary alloys used in the past (Figure 1.4) are steel (Fe-C), brass (Cu-Zn), and binary (Cu-Sn) and ternary bronze (Cu-Sn-Pb)[18].

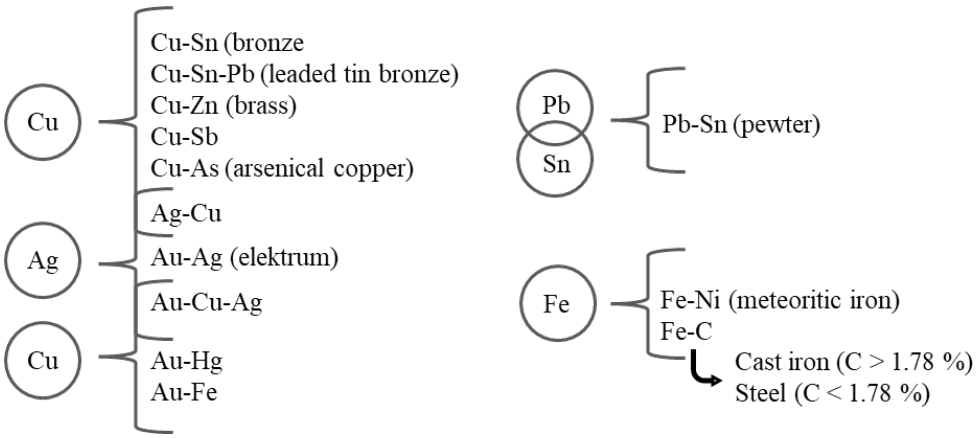

Fig. 1.4 Ancient metals and alloys used in the past.

1.2.1 Corrosion phenomena

The corrosion of metallic artefacts represents a challenge for the preservation and fruition of the Cultural Heritage artefacts. Over time, metals undergo chemical reactions with the environment, leading to degradation and alteration of their physical and chemical properties [21]. This phenomenon can undermine the integrity, aesthetic value, and preservation of archaeological artefacts, historical metallic structures, and other metal objects of cultural significance. Understanding the mechanisms and factors influencing corrosion is essential for developing effective conservation strategies. In this introduction, the causes, types, and consequences of corrosion in metallic artefacts, as well as the importance of corrosion mitigation efforts in Cultural Heritage safeguarding are deeply explored.

Various factors can contribute to the corrosion of metallic artefacts: environmental conditions such as humidity, temperature fluctuations, aggressive agents, the composition and microstructure of the metallic alloy as well as any bulk treatment or surface coating [22]. The consequences can be a severe degradation of the artefact. In fact, corrosion can lead to the loss of surface details, structural weakening, and finally, the complete degradation of the artefact.

Overall, the strategies used for conservation purposes are several, for example controlling the environmental conditions, implementing protective coatings, and employing corrosion inhibitors [23].

There are numerous ways in which corrosion can occur, including superficial corrosion, localized corrosion (such as pitting and crevice corrosion), galvanic

corrosion, and atmospheric corrosion. As mentioned before, the corrosion strictly depends on the environment and the corrosion susceptibility of the metal alloy. As the corrosion of iron will be deeply presented in Chapter 4.1.2, a brief introduction to the corrosion of Cu-based alloys will be presented.

Cu-based alloys, in particular bronze (Cu-Sn, Cu-Sn-Pb) and brass (Cu-Zn) are susceptible to various forms of corrosion due to their composition and environmental exposure [24]. In particular, the corrosion behaviour is influenced by the different corrosion susceptibilities of the alloying metals (Sn, Zn, Pb) and phases. The corrosion layers formed on the surface have been extensively studied, revealing a complex micro-chemical and stratified structure [25]. It is widely recognized that artefacts buried in soil for several years develop at least two distinct types of patina. The first layer, which is primarily composed of Sn and/or Cu oxides is formed directly on the metallic surface and acts as a protective layer. In contrast, the second type of corrosion layer forms under more aggressive corrosive conditions, often involving Cl^- ions which strongly interact with oxygen and humidity [26]. This phenomenon, known as the *bronze disease*, leads to an ongoing corrosion process that can degrade the artefacts. This second patina is thicker and can influence both the readability and the aesthetic qualities of the surface. If left untreated, the *bronze disease* can lead to the complete degradation of the object. Therefore, it is essential to identify and treat it to prevent further deterioration.

1.3 References for Cultural Heritage applications

Certified Reference Materials (CRMs) are essential tools used in different measurement fields, for example in analytical chemistry, quality control, and so on. These materials serve as standards for validating measurement methods, calibrating instrumentation, and ensuring the accuracy and reliability of measurements. CRMs are well-characterized substances with known composition and properties. They are produced and certified by accredited laboratories or organizations using rigorous quality assurance procedures. Validation goeas through an extensive characterization using multiple analytical techniques to determine their composition, homogeneity, stability, and uncertainty. These certified values are in agreement with metrological standards [27].

Concerning the Cultural Heritage field, CRMs are not always available for all types of analyses, especially because the materials examined are often not homogeneous. For this purpose, it was necessary to produce and characterize some alloys in laboratory to be used as references, in order to subsequently calibrate the Neutron Imaging station at the LENA Centre to be able to implement the application of the techniques at real artefacts. In summary, the Cu-based reference alloys are characterized by chemical composition, microstructure and metallurgical features similar to archaeological artefacts. The entire procedure and the consequent characterization are described in detail in 2.

Chapter 2

Absorption Contrast Neutron Imaging

The chapter is dedicated entirely to the Neutron Imaging technique. An explanation of the physical theory is provided after a brief introduction to the method and its applications in the Cultural Heritage field. After that, the methodology used for the calibration of the system is therefore presented, starting from the preparation and characterization of the samples up to the acquisition of the images, with the consequent discussion of the results obtained.

Some of the work described in this chapter has been previously published in [28].

2.1 Introduction and theory

Neutron imaging is a non-invasive and non-destructive analytical technique, which has become increasingly valuable in studying and preserving Cultural Heritage [29]. Its ability to penetrate materials that are otherwise difficult to examine without damaging them makes it highly applicable in this field, for example, for example for the characterization of metal [30], stone [31], wood [32], and other dense substances that are strongly challenging for other techniques. Despite its several advantages, the main disadvantage of this technique is that neutron facilities are limited and expensive, limiting the spread of the technique. The field of Neutron Imaging in Cultural Heritage is dynamic, with ongoing developments aiming to refine techniques,

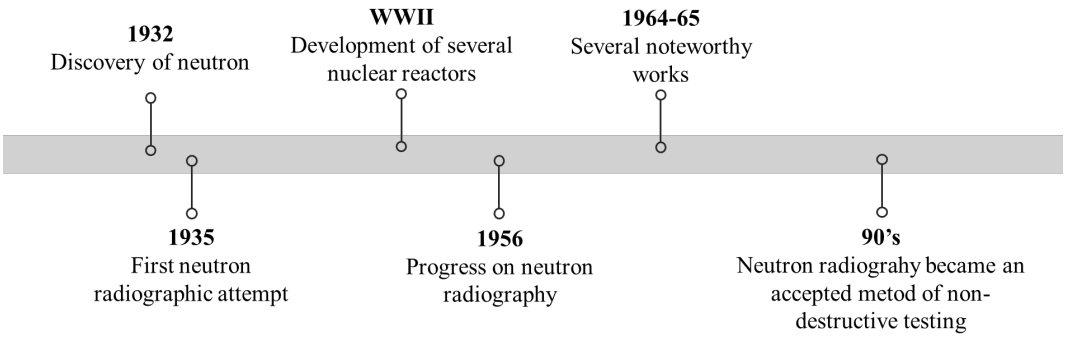

Fig. 2.1 Timeline of development and use of Neutron Imaging as non-destructive techniques for material science studies.

broaden applications, and make this powerful tool more accessible to researchers and conservationists.

The history of this technique (briefly schematized in Figure 2.1) started shortly after the discovery of the neutron in 1932 [33]. The first attempt to use neutrons to make radiographs was made in 1935, but with poor results given the unsuitable characteristics of the neutron source (i.e. weak and not-defined beam). However, it wasn't until the development of nuclear reactors during and after World War II that neutron radiography saw significant advancements. These reactors increased the number of available sources of neutrons which gained also in the intensity of neutron fluxes. Surprisingly, it wasn't until 1956 that further progress on neutron radiography was reported marking a significant milestone in the field. The advancement of neutron radiography progressed slowly over several years until the early 1960s when various researchers documented their efforts in this field. These improvements showed the potential of neutron radiography and paved the way for future developments in applying neutron beams for imaging purposes [34]. However, despite its almost 80-year history, it is only within the past three decades that it has gained prominence as a recognized method of non-destructive analysis for material science. As mentioned above, although the potential of the technique was immediately clear, it did not have a large diffusion as had happened with X-ray radiography which instead was developed and improved very quickly. This was probably caused by the complexity of the apparatus and the numerous hours of exposure that were required to obtain good results.

The setup for Neutron Imaging shares some similarities with X-ray imaging: there is a source that emits a beam that passes through a sample and reaches a detector. The biggest difference lies in the source, which emits a neutron beam. In the interaction with the matter, it interacts with the nuclei of the atoms within that object, unlike X-rays which interact with the electrons. Neutrons can be scattered or absorbed by the atomic nuclei, depending on the neutron energy and the properties of the material: this attenuation of the neutron is strongly dependent on the density and composition of the object. A detector system captures the transmitted neutrons recording their intensity and spatial distribution. The recorded data is then processed and reconstructed into an image using algorithms. The resulting image provides information about the internal structure, composition, and density variations within the object [35] [34].

A neutron is a subatomic particle that is one of the constituents of the atomic nucleus, along with protons (nucleons) [33]. Unlike protons, which have a positive electrical charge, neutrons have no net electrical charge. This neutrality means that electromagnetic forces do not influence neutrons and are therefore electrically neutral [36]. In the interaction with the matter, neutrons do not interact with the electrons of the atomic shells (e.g. photons) but instead, they interact with the nuclei, as schematized in Figure 2.2. This difference causes a nonlinearity in the relationship between the atomic number Z and the probability of the interaction, described by the microscopic cross-section: this is the main difference with X-ray Imaging. The particular interaction of neutrons with nuclei allows the differentiation of several elements like hydrogen, carbon, nitrogen, and oxygen [35].

Neutrons are often generated through nuclear reactions either in reactor sources (through fission or spallation) or in particle accelerators. This is the reason why the

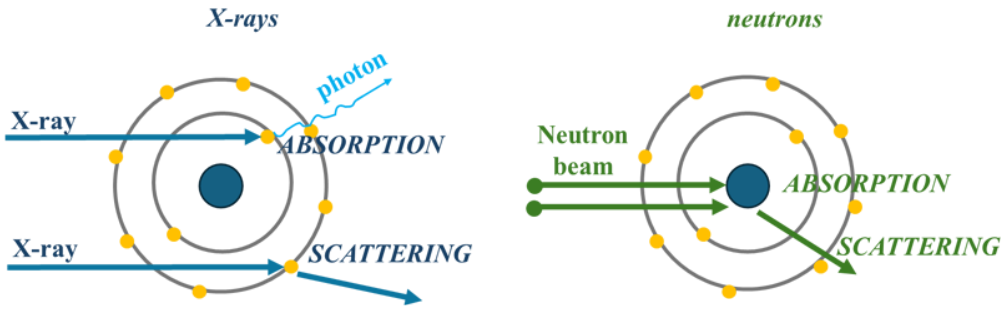

Fig. 2.2 Difference between the interaction of X-rays (left) and neutrons (right) with atoms.

Table 2.1 Nomenclature of neutrons divided according to their energies

Neutrons	Energy (meV)	Velocity (m/s)
Ultracold	0.00025	6.9
Cold	1	437
Thermal	25	2187
Epithermal	1000	13832

technique is not so widespread. However, the energy of the resulting neutron beam is too high to be suitable for imaging purposes. To decrease the energy of the neutrons by inelastic scattering are often used moderators (H_2O or D_2O) which thermalize the neutron beam. Neutrons can be divided into different classifications based on their energy. The details of the classifications are shown in 2.1.

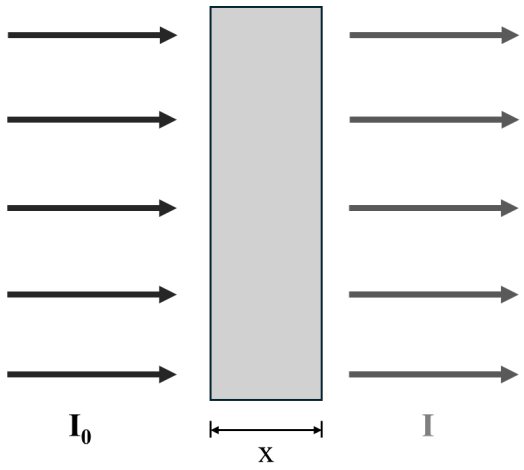

Fig. 2.3 Schematic representation of the interaction of an incident neutron beam (intensity I_0) with an object (thickness x); the result is a decrease in the intensity (I).

As already mentioned before, the neutron beam can be attenuated by absorption or scattering by matter. This attenuation can be expressed as an exponential function which correlates the incident neutron intensity (I_0) and the resultant transmitted neutron intensity (I) (Figure 2.3). The relationship is described by the simple attenuation law:

$$I = I_0 e^{-\Sigma x} \tag{2.1}$$

where I_0 is the initial intensity of the neutron beam, I is the resulting intensity after the interaction, x is the thickness of the sample and Σ is the linear attenuation coefficient. This coefficient includes the total microscopic cross section of an element (σ_t) that represents the probability of interaction between neutrons and matter. It is possible to express the Σ also with the following equation:

$$\Sigma = \frac{N_A \rho}{atwt} \times \sigma_t \tag{2.2}$$

where Σ is the attenuation coefficient, N_A is the Avogadro number and ρ and *at wt* are respectively the density and the atomic weight of the chemical element. The total cross section σ_t which takes into account the cross sections correlated to the scattering and absorption effects is described as follows:

$$\sigma_t = \sigma_s + \sigma_a \tag{2.3}$$

where σ_t is the total microscopic cross section, σ_s represents the scattering cross section and σ_a is the absorption cross section. The measurement units for the microscopic cross section are *barns*, and 1 barn = 10^{-24} cm^2.

To simplify comparisons across different aggregate states with complex chemical compositions, it can be used the ratio between Σ and ρ, known as the mass attenuation coefficient. This value varies depending on different factors such as neutron energy and the composition of the material. Overall, the mass attenuation coefficient (Σ/ρ) is not linearly dependent on the atomic number of the chemical elements (Figure 2.4). As mentioned before, this attenuation property can be exploited to study light elements and, moreover, neighbouring elements in the periodic table. Calculating the mass attenuation coefficient knowing the neutron energy implies that it is possible to characterize the type of material.

To better understand the advantage of using Neutron Imaging, the difference between the attenuation coefficients for neutrons and x-rays is given as an example in Figure 2.5. As can be seen from the figure, the trend of grey levels essentially follows the periodic table for x-rays (top) while neutrons (bottom) do not follow linearity. This is very useful, especially in the case of analysis of artefacts made up of elements close together in the table (for example Cu, Zn or Sn) which present grey level variations in intensity compared to x-rays [37].

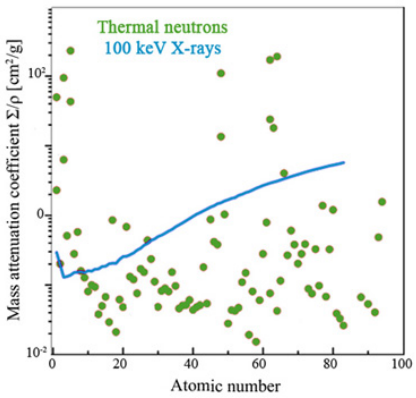

Fig. 2.4 Comparison between the mass attenuation coefficients for thermal neutrons (green points) and X-rays (light blue line).

Attenuation coefficients for thermal neutrons (cm^{-1})

1a	2a	3b	4b	5b	6b	7b	8			1b	2b	3a	4a	5a	6a	7a	0
H																	He
3.44																	0.02
Li	Be											B	C	N	O	F	Ne
3.30	0.79											101.60	0.56	0.43	0.17	0.20	0.10
Na	Mg											Al	Si	P	S	Cl	Ar
0.09	0.15											0.10	0.11	0.12	0.06	1.33	0.03
K	Ca	Sc	Ti	V	Cr	Mn	Fe	Co	Ni	Cu	Zn	Ga	Ge	As	Se	Br	Kr
0.06	0.08	2.00	0.60	0.72	0.54	1.21	1.19	3.92	2.05	1.07	0.35	0.49	0.47	0.67	0.73	0.24	0.61
Rb	Sr	Y	Zr	Nb	Mo	Tc	Ru	Rh	Pd	Ag	Cd	In	Sn	Sb	Te	I	Xe
0.08	0.14	0.27	0.29	0.40	0.52	1.76	0.58	10.88	0.78	4.04	115.11	7.58	0.21	0.30	0.25	0.23	0.43
Cs	Ba	La	Hf	Ta	W	Re	Os	Ir	Pt	Au	Hg	Tl	Pb	Bi	Po	At	Rn
0.29	0.07	0.52	4.99	1.49	1.47	6.85	2.24	30.46	1.46	6.23	16.21	0.47	0.38	0.27			
Fr	Ra	Ac	Rf	Ha													
	0.34																

	Ce	Pr	Nd	Pm	Sm	Eu	Gd	Tb	Dy	Ho	Er	Tm	Yb	Lu
*Lanthanides	0.14	0.41	1.87	5.72	171.47	94.58	1479.04	0.93	32.42	2.25	5.48	3.53	1.40	2.75
	Th	Pa	U	Np	Pu	Am	Cm	Bk	Cf	Es	Fm	Md	No	Lr
**Actinides	0.59	8.46	0.82	9.80	50.20	2.86								

Attenuation coefficients for thermal X-rays (cm^{-1}) (150 kV)

1a	2a	3b	4b	5b	6b	7b	8			1b	2b	3a	4a	5a	6a	7a	0
H																	He
0.02																	0.02
Li	Be											B	C	N	O	F	Ne
0.06	0.22											0.28	0.27	0.11	0.16	0.14	0.17
Na	Mg											Al	Si	P	S	Cl	Ar
0.13	0.24											0.38	0.33	0.25	0.30	0.23	0.20
K	Ca	Sc	Ti	V	Cr	Mn	Fe	Co	Ni	Cu	Zn	Ga	Ge	As	Se	Br	Kr
0.14	0.26	0.48	0.73	1.04	1.29	1.32	1.57	1.78	1.96	1.97	1.64	1.42	1.33	1.50	1.23	0.90	0.73
Rb	Sr	Y	Zr	Nb	Mo	Tc	Ru	Rh	Pd	Ag	Cd	In	Sn	Sb	Te	I	Xe
0.47	0.86	1.61	2.47	3.43	4.29	5.06	5.71	6.08	6.13	5.67	4.84	4.31	3.98	4.28	4.06	3.45	2.53
Cs	Ba	La	Hf	Ta	W	Re	Os	Ir	Pt	Au	Hg	Tl	Pb	Bi	Po	At	Rn
1.42	2.73	5.04	19.70	25.47	30.49	34.47	37.92	39.01	38.61	35.94	25.88	23.23	22.81	20.28	20.22		9.77
Fr	Ra	Ac	Rf	Ha													
	11.80	24.47															

	Ce	Pr	Nd	Pm	Sm	Eu	Gd	Tb	Dy	Ho	Er	Tm	Yb	Lu
*Lanthanides	5.79	6.23	6.46	7.33	7.68	5.66	8.69	9.46	10.17	10.91	11.70	12.49	9.32	14.07
	Th	Pa	U	Np	Pu	Am	Cm	Bk	Vf	Es	Fm	Md	No	Lr
**Actinides	28.95	39.65	49.08											

Fig. 2.5 Attenuation coefficients correlated to grey levels; on the top, attenuation coefficients for thermal neutrons and on the bottom, attenuation coefficients for x-rays, from [35].

2.2 The system developed: the NICHE project

INFN-CHNet is the network of the National Institute of Nuclear Physics whose mission is mainly to develop and apply measurement techniques in the Cultural Heritage field [38]. In particular, in April 2021 started the NICHE project (where NICHE stands for Neutron Imaging for Cultural HEritage), which involved the development of the first Neutron Imaging station for Cultural Heritage purposes at the Applied Nuclear Energy Laboratory (LENA) of Pavia (Pavia, Italy) [39]. Before starting the installation of the line dedicated to Neutron Imaging, the reactor was subjected to different preliminary tests and simulations to study and check the beam proprieties that can affect the quality of the analyses (i.e. neutron flux, beam size, and so on) showing very promising results despite some limitations [40].

The imaging station is therefore installed on the TRIGA-MARK II reactor's thermal beam port (channel B). The reactor is used for different purposes, for example, the determination of trace elements (Neutron Activation Analysis and Prompt Gamma-ray Activation Analysis), medical use for radiotherapy (Boron-Neutron Capture Therapy), medical diagnosis, characterization of materials [41] [42]. In this scenario, the entire setup must be easily assembled and disassembled between one measurement campaign and another to permit the use of channel B for other applications.

The TRIGA MARK II is a 250 kW thermal power reactor (in steady state). The maximum neutron flux (central channel) is 1.8×10^{13} cm^{-2} s^{-1}. Neutrons are slowed down to thermal energies with moderators (HZr, H_2O) to be suitable for Neutron Imaging analyses. Between the core and the experimental setup are placed different filters (bismuth and sapphire) to eliminate the contribution of non-thermal neutrons and γ-rays. The resulting thermal flux of channel B is 1.6×10^{7} cm^{-2} s^{-1} [43]. As already mentioned, different studies were conducted before performing this last chapter of the experiment. In particular, all the configurations (constituent materials, working distance, etc) were tested to optimize the results. For further details, refer to [40] [43] [44].

Briefly, the components of the experimental setup (presented in Figure 2.6 and deeply explained in [44] and [43]) will be presented:

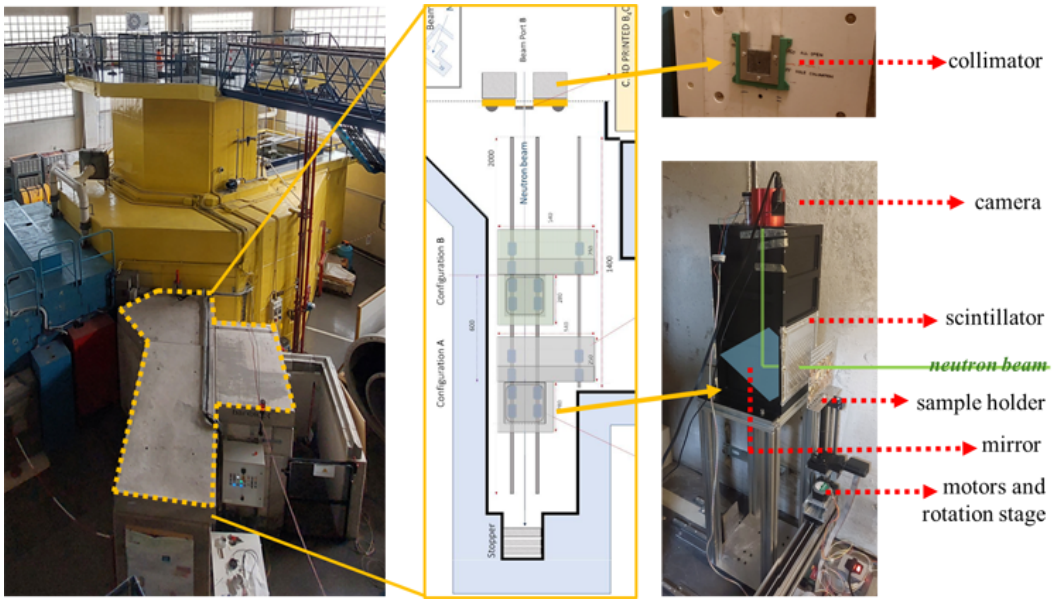

Fig. 2.6 The imaging station developed at the Applied Nuclear Energy Laboratory LENA of Pavia (Italy). On the left, the TRIGA MARK II reactor and the shielded room around port B where is installed the imaging station; in the middle, the schematic top view of the imaging station; on the right, visualization of the main components of the imaging station.

- **Remote controllers**: the system (motors, camera) is remotely controlled by an ARDUINO Mega via LabView 2018 SPI with a dedicated developed code which permits acquiring images in sequence;
- **Collimator**: removable B_4C plate in aluminium and Polylactic Acid 3D printed holder. The collimator is removable and exchangeable according to the application. The different available pin-hole diameters are from 5 mm to 50 mm;
- **Motors and rotation stage**: two motors that allow the movement along the z-axis and x-axis (perpendicular to the neutron beam) are performed with stepper motors; a PI M-060 stage makes the rotation around the y-axis. All the motors are remotely controlled to move the sample holder to align the sample and, in case, to rotate the sample to perform 3D tomography;
- **Detector**: it is placed inside a dedicated neutron dark camera box and is constituted of different components. The **scintillator** is argent doped ^{6}LiF/ZnS (Tritec) with a thickness of 300 μm and dimensions of 200 mm $\times$ 200 mm. A 45° inclined **mirror** deviates the signal to the camera and limits the radiation

damage to the acquisition camera. The **camera**, equipped with a 35 mm optical lens (f/1.6), is a digital ZWO ASI 2600 MM CMOS 16 bit. Each pixel corresponds to an area of 30 μm $\times$ 30 μm of the scintillator. The resultant **FOV** (Field of View) is 180 μm $\times$ 120 μm. The camera box is cooled by a double thermoelectric Peltier **refrigeration system**.

All the parameters used for image acquisitions will be deeply presented in subsection 2.4.1.

2.3 Cu-based reference alloys: production and characterization

The main progress of the setup involved the use of imaging to carry out the characterization of metals, as a precise analysis of the constituent alloy. This required the production of a set of Cu-based reference samples made up of different metal alloys, with compositions similar to real artefacts, to calibrate and characterize the beam. The main goal was to obtain information regarding the composition of the alloy after the image processing. In addition, some references have been artificially aged to obtain superficial corrosion patinas which present a chemical composition different from the metal alloy. The following subsections describe how the various alloys and patinas were obtained, followed by chemical and metallurgical characterization of the samples.

2.3.1 Production of Cu-based reference alloys

"A large set of Cu-based reference alloys with metallurgical features and microstructure similar to ancient bronze artefacts were produced in laboratory [45] [46]. The selected chemical composition is ascribed to the material classes Cu-Sn, Cu-Zn and Cu-Sn-Pb. In particular, Cu-Sn and Cu-Zn alloys were produced by increasing the concentration of Sn and Zn in the range of 4-12 wt% and 5-25 wt%, respectively; the ternary alloy, Cu-Sn-Pb, was produced with a fixed amount of Sn (6 wt%) and by increasing the concentration of Pb in the range of 4-16 wt%."[28]. The selected chemical compositions are presented in Table 2.2.

Sample name	Cu (wt%)	Zn (wt%)	Sn (wt%)	Pb (wt%)
CuZn5	95	5	-	-
CuZn10	90	10	-	-
CuZn15	85	15	-	-
CuZn20	80	20	-	-
CuZn25	75	25	-	-
CuSn4	96	-	4	-
CuSn6	94	-	6	-
CuSn9	91	-	9	-
CuSn12	88	-	12	-
CuSn6Pb4	90	-	6	4
CuSn6Pb8	86	-	6	8
CuSn6Pb12	82	-	6	12
CuSn6Pb16	78	-	6	16

Table 2.2 Nominal chemical composition of the different alloys produced in laboratory.

"The alloys were produced by using a Lindberg Blue STF54434C tube furnace. Alumina cylindrical crucibles (Al_2O_3 99% purity, diameter of 2.5 cm, height of 7 cm) coated inside with graphite to avoid metal oxidation were used for metal melting. The alloys were melted under an inert atmosphere (Ar, 99% purity) in the tube furnace according to the following protocol: heating ramp from room temperature to 1250°C in 2 hours, maintenance of temperature for 1 hour, cooling ramp from 1250 °C to room temperature in 5 hours."[28] The obtained ingots were sectioned obtaining disks of 4 mm thick by using a QATM Qcut 200A precision cut-off machine, equipped with a silicon carbide (SiC) wheel under a constant refrigerant flow. A sequence of the preparation of the samples is presented in Figure 2.7.

2.3.2 Characterization of Cu-based reference alloys

Firstly, the thickness of each sample was measured with a calibre. This measure will be fundamental in the calculation of the mass attenuation coefficient. After all, the Cu-based reference samples were deeply studied using Optical Emission Spectroscopy (OES) for the chemical characterization and metallographic examination to underline the alloys' microstructure.

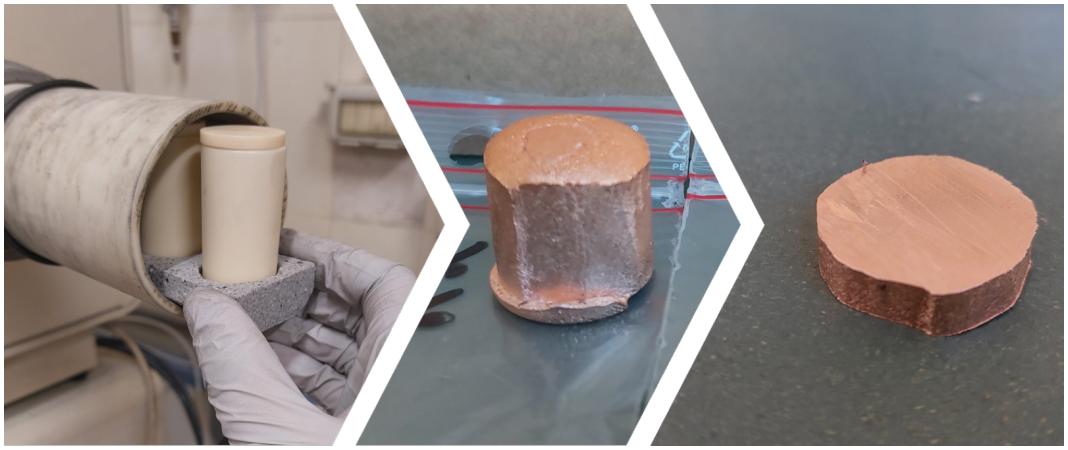

Fig. 2.7 Preparation of Cu-based reference samples: from the left, alumina cylindrical crucibles before being put in the tube furnace, example of obtained ingots and lastly, the sample after precise cutting.

Optical Emission Spectroscopy

The chemical composition of the Cu-based reference samples was quantitatively determined post-melting through Optical Emission Spectroscopy (OES), employing an S7 Metal Lab Plus Quantometer for the analysis. In OES, the sample is subjected to a high-energy heat source causing the emission of characteristic wavelengths of light that depends on the atoms in the sample. These emitted wavelengths are then analyzed using a spectrometer to determine the elemental composition of the sample. The results for the main elements (Cu, Zn, Sn, and Pb) of OES measurements with their associated uncertainties are presented in Table 2.3.

As is evident from the comparison between Table 2.2 and Table 2.3, some samples do not have precise correspondence between the nominal composition and the effective composition after the melting. This is more evident in the samples with lead, which are more subjected to non-homogeneous diffusion and segregation of lead at the expense of copper. The plausible explanation lies in the big difference in the melting temperature of these two metals (Cu = 1085 °C; Pb = 327.5 °C) forces this non-homogeneous behaviour [47]. Despite that, the results obtained from OES will be used for the theoretical calculation of the density of each sample for imaging processing.

Sample	Cu (wt%)	Zn (wt%)	Sn (wt%)	Pb (wt%)
CuZn5	94.7 ± 0.8	5.1 ± 0.8	-	-
CuZn10	90.9 ± 0.9	9.0 ± 0.9	-	-
CuZn15	85.6 ± 0.9	14.3 ± 0.9	-	-
CuZn20	81.5 ± 1.1	18.4 ± 1.1	-	-
CuZn25	78.6 ± 1.5	21.3 ± 1.5	-	-
CuSn4	95.2 ± 0.4	-	4.7 ± 0.4	-
CuSn6	93.5 ± 0.5	-	6.5 ± 0.5	-
CuSn9	90.2 ± 0.4	-	9.8 ± 0.4	-
CuSn12	88.8 ± 0.5	-	11.1 ± 0.5	-
CuSn6Pb4	89.0 ± 0.6	-	6.1 ± 0.2	4.8 ± 0.5
CuSn6Pb8	84.2 ± 1.2	-	5.9 ± 0.3	9.8 ± 0.9
CuSn6Pb12	79.6 ± 1.1	-	6.3 ± 0.1	14.0 ± 1.1
CuSn6Pb16	73.9 ± 1.6	-	5.0 ± 0.4	21.0 ± 1.4

Table 2.3 Composition of the Cu-based reference alloys determined by OES.

Microstructure characterization

Furthermore, the metallographic examination of the reference samples was conducted to deeply analyze the alloy's microstructure also to verify any segregation of the samples with Pb. A sample for each type of alloy was embedded in acrylic resin and meticulously mirror polished (from 500-grid SiC paper to 1 μm diamond paste). Subsequently, chemical etching of the transversal section was performed submerging the samples for 15 s in an Iron(III) chloride solution (1 g $FeCl_3$, 10 mL HCl, 100 mL distilled water), as per the *Standard Practice for Microetching Metals and Alloy*s protocol [48]. The samples were rinsed in ethanol and dried with hot air before being observed under the metallographic microscope. The sections were examined using a Reichert-Jung MeF3 optical microscope at different magnifications (5×, 10×, 20×, 50×).

As can be seen from Figure 2.8, the microstructures of the alloys are heterogeneous, consisting of various phases and structural features. The most representative observations will be discussed below:

- Figure 2.8A) shows the microstructure of CuZn15 alloy (brass) that is basically a single-phase alloy, containing a solid solution of Zn and α-Cu. In the formation of the alloy, the α-Cu phase is the first to solidify (at low concentration of

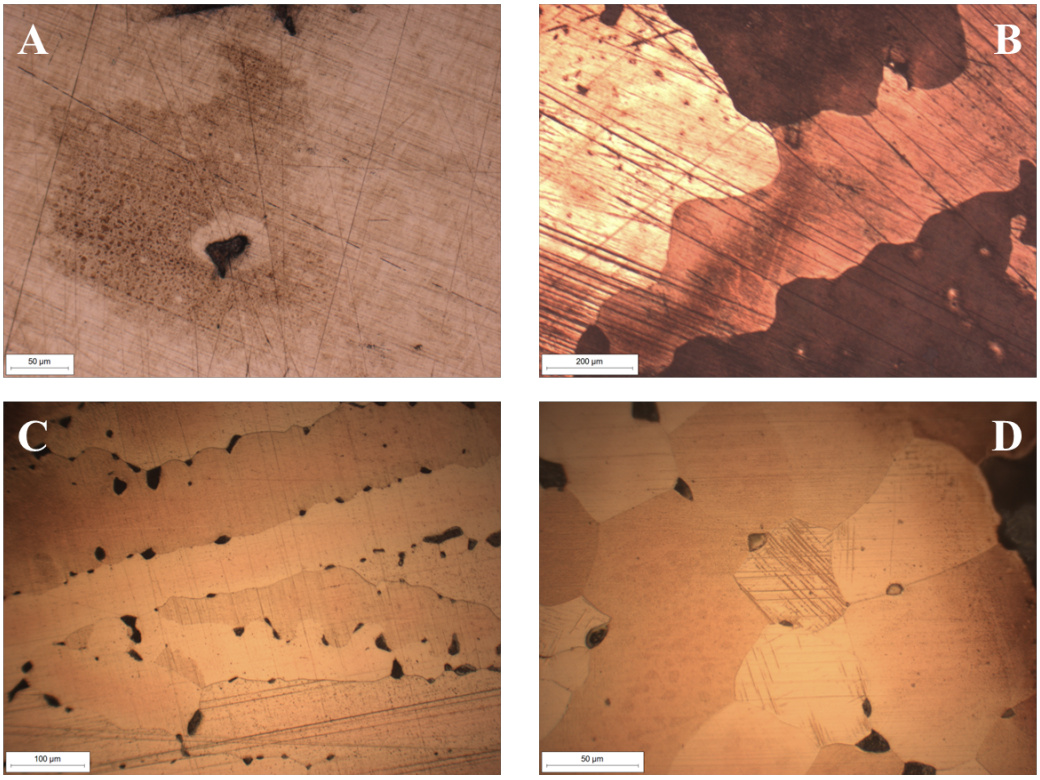

Fig. 2.8 Metallographies of different Cu-based reference samples etched in $FeCl_3$ solution. A) CuZn15 at 20× magnification, B) CuSn6 at 5× magnification, and CuSn6Pb4 at C) 10× and D) 20× magnification.

Zn, up to 35%); then an enrichment of Zn occurs, becoming a mixture of Cu and Zn. The resulting microstructure consists of equiaxed grains of α-brass.

- Figure 2.8B) shows the microstructure of a binary alloy CuSn6 (tin bronze). The structure presents α grains and γ eutectoid at the grain boundaries. This microstructure remains until 15.8% of Sn. The differences in colours in the metallography represent the different grain orientations, which are almost equi-axed.

- Figure 2.8C) and D) show the microstructures of ternary alloy CuSn6Pb4 (leaded tin bronze). The microstructure is similar to tin bronze, with α and δ phases. Being practically insoluble in solid Cu, Pb solidifies predominantly as pure Pb within the grain boundaries. As it is possible to see from the metallographies, the grains are large and elongated compacting towards the edges of the section.

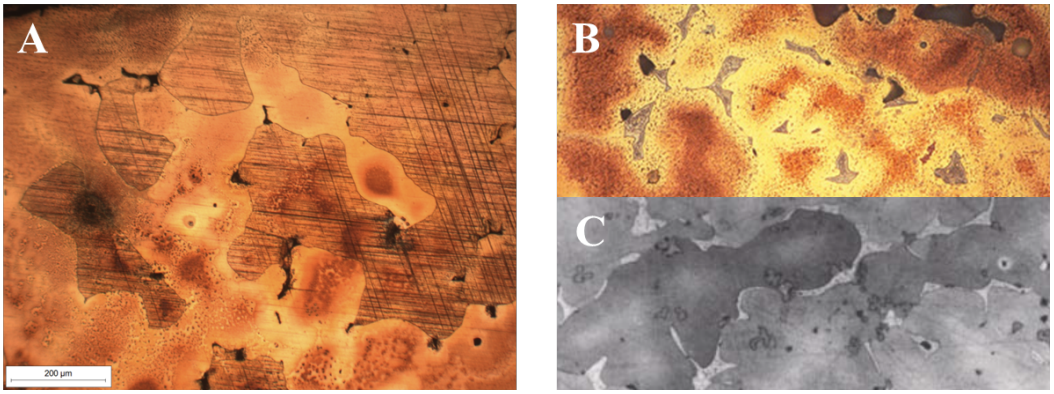

Fig. 2.9 Comparison of A) the microstructure of sample CuSn12 after etching with $FeCl_3$ and microstructure of B) Cu88-90Sn10-12 cast alloy [47] and C) ancient tin-bronze artefact [48].

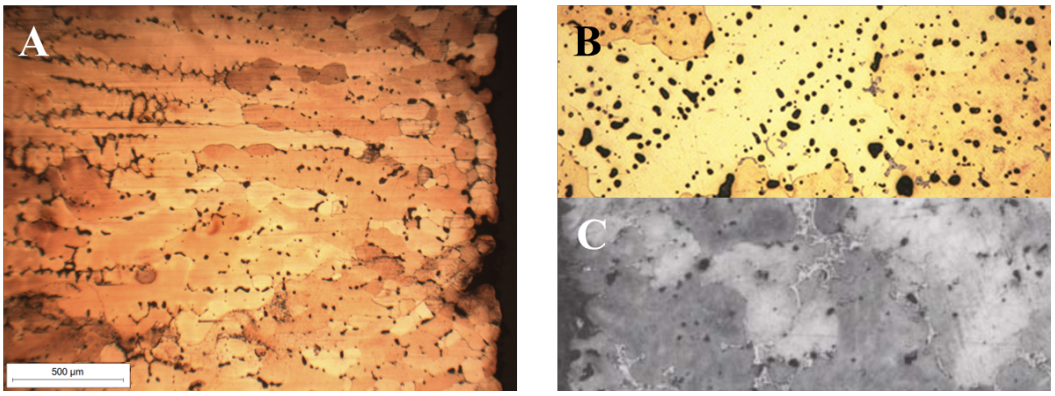

Fig. 2.10 Comparison of A) the microstructure of sample CuSn6Pb8 after etching with $FeCl_3$ and microstructure of B) Cu81-85Sn6-3Pb6-8 cast alloy [47] and C) ancient Cu90Sn7Pb3 bronze artefact [48].

To evaluate the consistency of the samples, the metallographies of the Cu-based reference alloys were compared with some metallographies from the literature [49] [50].

As can be seen in Figure 2.9, the obtained microstructure of CuSn12 sample (A) is comparable with the other microstructures from the literature (B and C). The equiaxed structure is evidenced, while the main difference is the absence of δ Sn-rich eutectoid in the boundaries probably due to a rare enrichment in Sn. The grains are globular, representing the solid solution between Cu and Sn.

Lastly, is evident in Figure 2.10 the microstructure of the presented sample (A) is comparable to the metallographies from the literature (B and C). The main difference

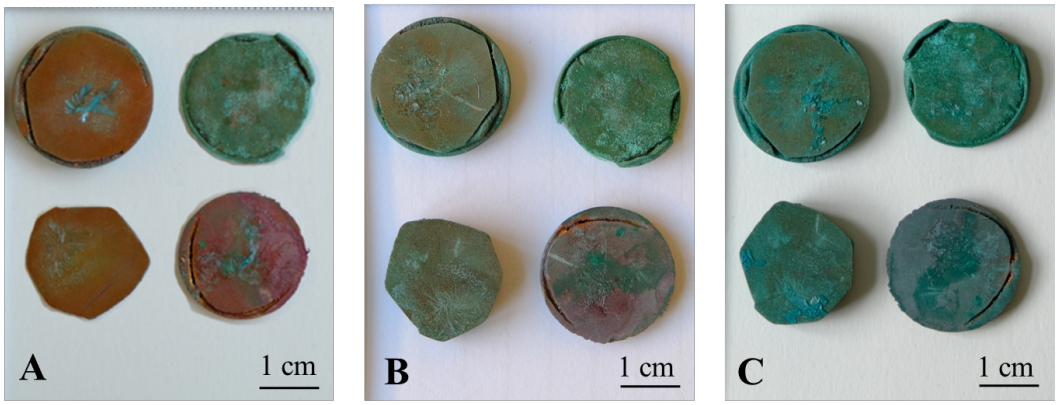

Fig. 2.11 Photographic documentation of sulphates-induced patina growth in immersion A) after 5 days, B)after 10 days and C) after 15 days.

is the dimension of the grains, which are elongated due to the cooling conditions. The small black inclusions are coherent with the diffusion and segregation of Pb in the grain boundaries.

2.3.3 Artificial ageing of Cu-based reference alloys

As mentioned before, Cu-based artefacts rarely appear free of corrosion patina because metals undergo natural corrosion modifying the composition of the surface. In this scenario, a set of references were artificially corroded to add the variable of superficial corrosion patina for calibration purposes, to evaluate the influence of layers of different chemical compositions from the alloys. Along these lines, a set of Cu-based reference alloys underwent polishing using 500 to 4000-grid SiC paper, followed by rinsing in ethanol in an ultrasonic bath for 5 minutes and thorough drying. Subsequently, two types of artificial patinas were developed on the metal surface: sulphates-induced patina and chlorides-induced patina.

The sulphates-induced patina was obtained through chemical synthesis in aqueous solutions containing copper sulphate ($CuSO_4$, 50 mM). The samples were immersed in the solution for 15 days [51]. Every 5 days, the samples were removed from the solution, allowed drying and photographed using an XT-Fujifilm camera to assess any colour alterations and patina growth (Figure 2.11).

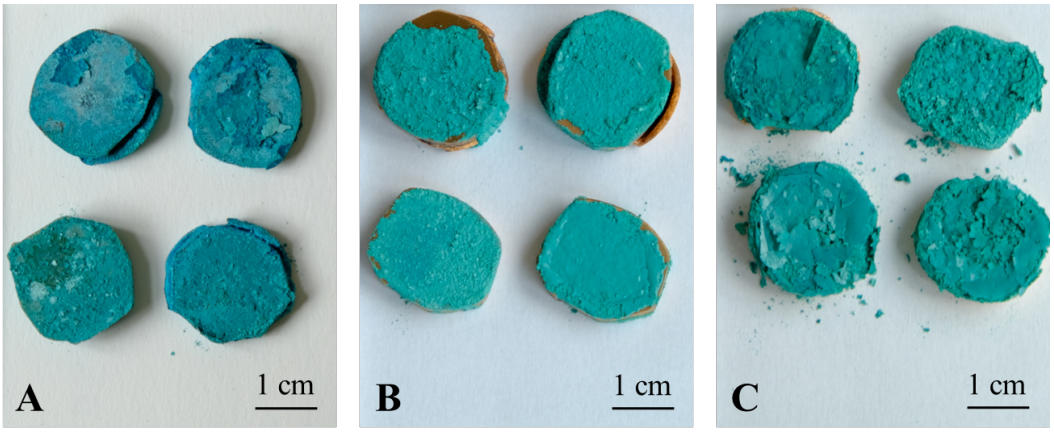

Fig. 2.12 Photographic documentation of chlorides-induced patina growth obtained by A) immersion for 7 days, B) dripping and C) brushing.

The chlorides-induced patina was obtained through chemical synthesis in aqueous solutions containing ammonium chloride (NH_4Cl, 33 wt%) [52]. Three different applications were tested:

1. **Immersion**: the samples were immersed in the solution with periodic drying intervals of 24 hours, for 1 week;
2. **Dripping**: the solution was applied continuosly for 1 day to the surface via dripping, allowing each application to dry before the next;
3. **Brushing**: the samples were frequently brushed with the solution for 1 day, letting the surface dry between one brushing and another.

At the end of the treatments, all the samples were photographed to document the patina growth. A close inspection of Figure 2.12 underlines how some applications were more effective than others. In particular, immersion was the best system of application while the dripping application returned a very thick and non-cohesive patina to the surface of the sample. Also, the samples obtained by dropping the solution on the surface were discarded due to their fragility. For this reason, the samples thus obtained (brushing and dripping) were not used for Neutron Imaging purposes.

2.3.4 Characterization of artificial aged reference alloys

The characterization of the obtained patina was necessary to obtain the chemical composition, surface morphology and, subsequently, patina thickness. All this information was evaluated by using different analytical methods: Raman spectroscopy and X-Ray Diffraction (XRD) for chemical composition and Field Emission Scanning Electron Microscopy (FESEM) for the surface morphology and patina thickness.

Raman spectroscopy

The first analysis involved the Raman characterization of the corrosion products. Briefly, Raman spectroscopy is a spectroscopic technique used to study the vibrational modes of molecules. It is a non-invasive and non-destructive analytical technique widely used in Cultural Heritage field. It provides detailed information about the molecular composition and structure of materials. When a monochromatic light source, typically a laser in the VIS range interacts with a sample, two scattering phenomena may occur: the first, known as Rayleigh scattering, where the scattered photons have the same energy (frequency) as the incident photons; the second, known as Raman scattering, where a small fraction of photons undergo inelastic scattering, losing or gaining energy due to interactions with vibrational modes of the molecules in the sample. The scattered photons are collected by a spectrometer which separates the scattered light into its different wavelengths (or frequencies), allowing the discrimination of Raman-shifted photons corresponding to specific vibrational modes of the sample. The obtained spectrum is in effect a fingerprint of the molecule.

Concerning the Raman measurements, the instrument is a "BWTEK i-Raman plus spectrometer equipped with a 532 nm excitation laser source, a CCD sensor with high quantum efficiency and wide dynamic range assisted by a cooling system and connected with an OPTEKA microscope equipped with different optics (4×, 20×, 40×, and 80×). All spectra were collected in the range between 150 cm^{-1} and 4200 cm^{-1} with a resolution of 5 cm^{-1}. The laser power was modulated to avoid chemical degradation of the sample due to laser radiation according to literature [53]. The acquisition parameters were set before measurement: 5 s integration time, 5 repetitions and laser power of 20%."[28]

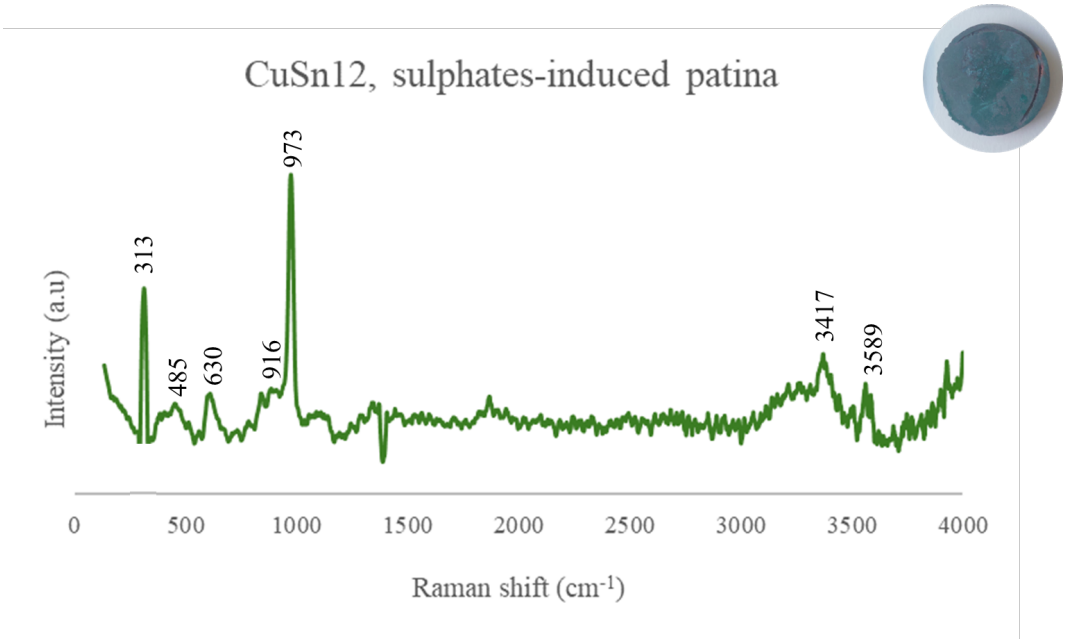

Fig. 2.13 Raman spectrum obtained on CuSn12 sample with sulphates-induce patina; the main peaks of brochantite ($Cu_4SO_4(OH)_6$ are evidenced.

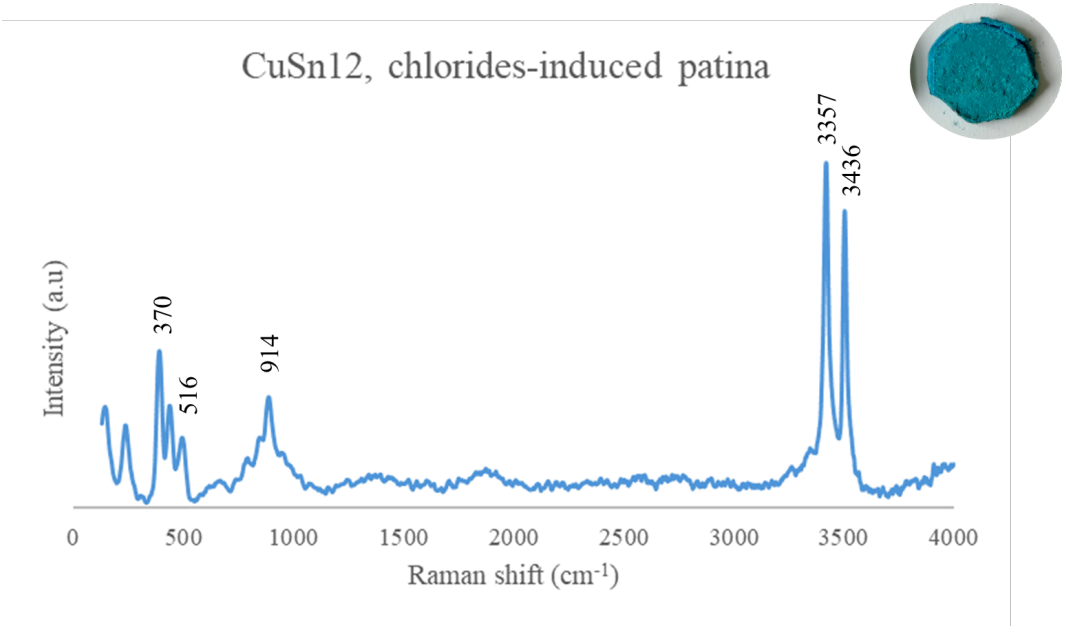

Fig. 2.14 Raman spectrum obtained on CuSn12 sample with chlorides-induce patina by immersion; the main peaks of atacamite ($Cu_2Cl(OH)_3$ are evidenced.

The spectra were acquired by using BWSpec software and subsequently processed with a dedicated asymmetric least squares smoothing [54]. The processed spectra were compared with those present in literature [55] [56] [57] with the assistance of Crystal Sleuth software [58]. Some examples are presented below. In particular, in Figure 2.13 is presented a spectrum obtained on the surface of a CuSn12 sample after immersion in sulphates solution. It should be noted that the main corrosion product is brochantite with its characteristic Raman peaks (313, 485, 630, 916, 976, 3417, 3589 cm^{-1}). Some areas gave back also the presence of cuprite (Cu_2O) and the presence (from the constituent alloy) of Sn. In Figure 2.14 is presented the spectrum obtained on CuSn12 sample treated with chlorides. The characteristic Raman peaks (370, 516, 914, 3357, 3436 cm^{-1}) evidenced the presence of atacamite.

X-ray diffraction

Additionally, to better distinguish polymorphs XRD analysis was performed in a non-invasive and non-destructive way, analyzing directly the corrosion products on the surface of the reference samples without sampling. Briefly, X-ray diffraction (XRD) provides information about the structure of crystalline materials by analyzing the diffraction patterns produced when X-rays interact with the atomic lattice. This is possible because the wavelengths of X-rays are comparable to the interatomic distances in crystals. In fact, the obtained diffraction pattern (intensity in function of the diffraction angle 2Θ) contains information about the arrangement of atoms in the crystal, giving the possibility to distinguish even polymorphs, thanks to the measurement of the angles and the intensities of the diffraction peaks. The diffractometer consists of an X-ray source, a monochromator, a sample stage and a detector.

The XRD measurements were carried out by using a "Panalytical X'pert PRO diffractometer equipped with a Cu-anode. XRD analysis were performed by setting the tube current and the tube tension at 40 mA and 40 kV, respectively. Diffractograms were acquired in the range of $8°2\theta$ to $90°2\theta$ with a measure step of $0.026°2\theta$."[28]

The corrosion products were identified through the utilization of HighScore Plus software. Some representative results are presented below, in particular, the XRD pattern of the two CuSn12 samples previously analyzed with Raman spectroscopy (Figure 2.14 and Figure 2.13) are presented. In Figure 2.15 is presented the diffraction

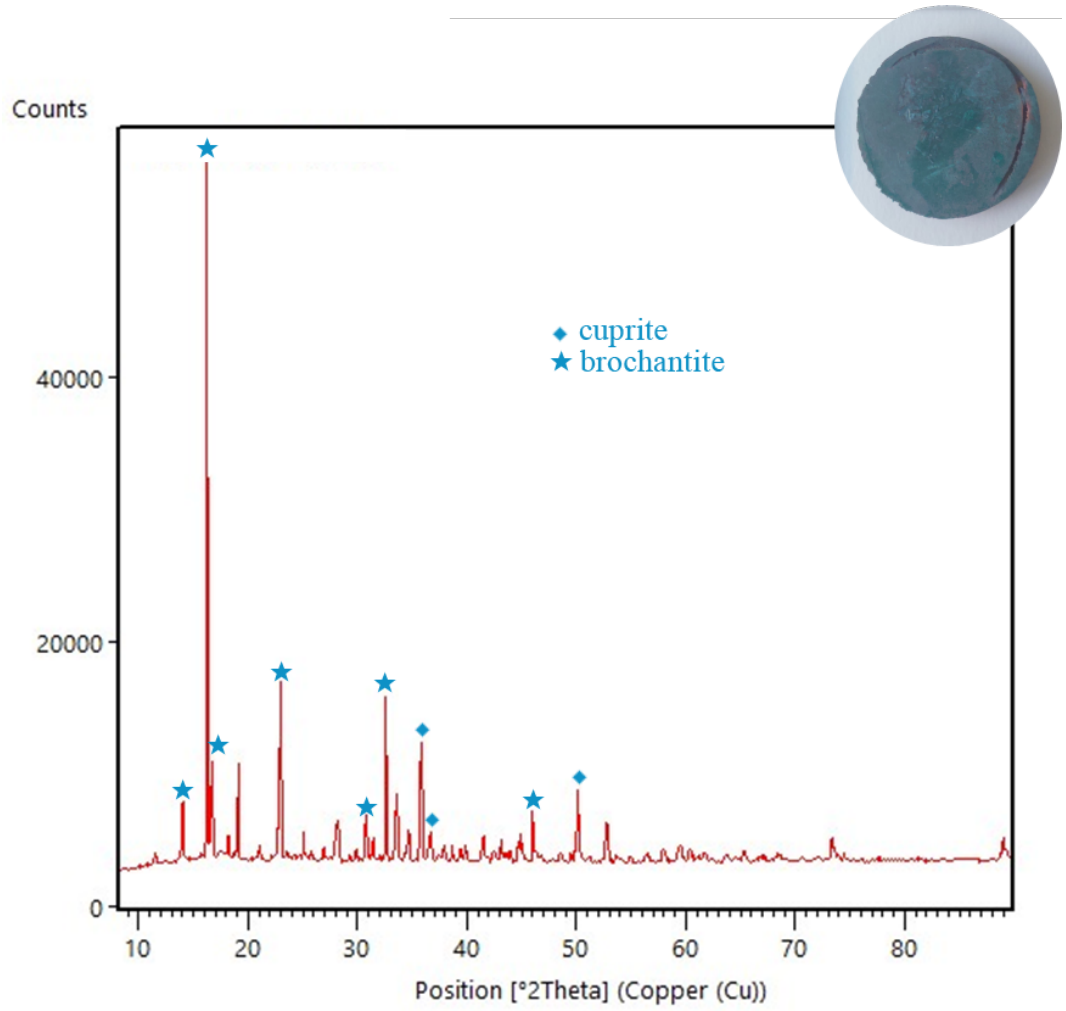

Fig. 2.15 Diffraction pattern obtained on CuSn12 sample coated by sulphates-induce patina; analyzing the main diffraction peaks, the presence of brochantite ($Cu_4SO_4(OH)_6$ and cuprite (Cu_2O) is highlighted.

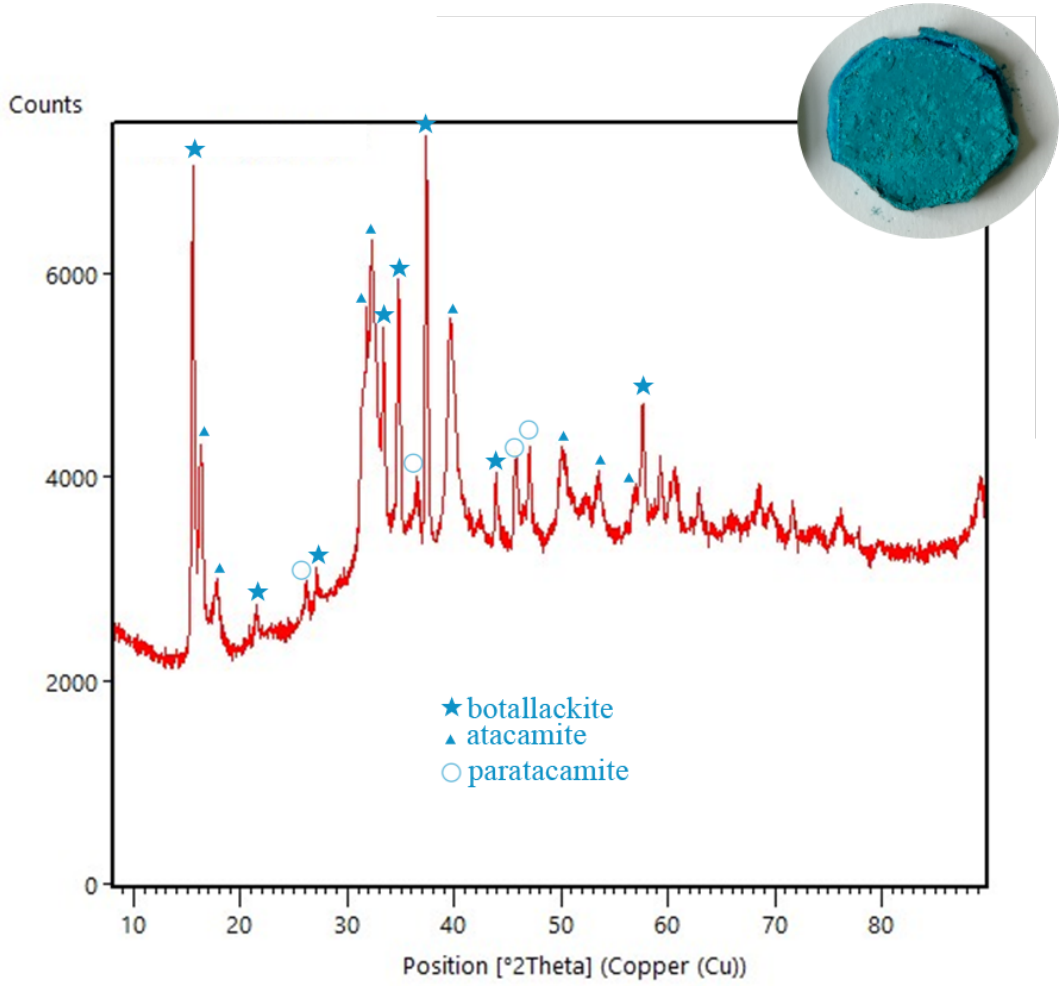

Fig. 2.16 Diffraction pattern obtained on CuSn12 sample coated by chlorides-induce patina by immersion; analyzing the main diffraction peaks, the presence of atacamite, paratacamite and botallackite ($Cu_2Cl(OH)_3$) is evidenced.

pattern obtained on the corrosion patina on CuSn12 reference sample, which confirms the Raman results highlighting the presence of brochantite and cuprite. In Figure 2.16 is reported the diffraction pattern of the corrosion layers on CuSn12 reference sample. The main corrosion products are atacamite, paratacamite and botallackite.

Field Emission Scanning Electron Microscopy

The last characterization was carried out by Field emission scanning electron microscopy (FE-SEM) to observe firstly the morphology of the surface and, moreover, to examine the longitudinal section. Briefly, FE-SEM is an advanced microscopy technique used to obtain high-resolution images of surface exploiting a field emission electron source to achieve superior resolution compared to conventional SEM. In fact, this source can produce a highly coherent and narrow electron beam which is focused on the sample. In the interaction, different phenomena may occur, including elastic and inelastic scattering and secondary electron emission. FESEM can be equipped with different detectors which provide unique information about the sample (i.e. secondary electrons, backscattered electrons, x-rays, and so on). The result is basically an image which highlights the surface morphology and the microstructure of the sample.

"The surface morphology was observed by means of a Zeiss Supra 40 FESEM microscope with secondary electron detector. The FESEM images were acquired using an acceleration voltage of 5 kV and an aperture size of 30 μm. The magnification was modulated depending on the dimension of the crystals."[28] The most relevant results are presented below. In Figure 2.17, A) and B) show the morphology of the surface. Basically, the corrosion patina is a well-crystallized hydrated copper sulphate; it has a compact and uniform aspect. The thickness of the resultant corrosion layer is about 20 μm, and is presented in C) and D). This could be a limit for the calibration of the system given that the resolution of the system is 150 μm. However, an attempt was made to characterize it with Neutron Imaging.

Considering the chlorides-induced patina, Figure 2.18 shows the more significant results. As it is possible to see in Figure 2.18, A) and B) show the surface's cracks. The surface exfoliates, creating some area without the corrosion layers forcing a non-homogeneous distribution. Essentially the layers are characterized by copper chloride hydroxides. The average thickness (C and D) of the corrosion patina is about 150 μm, almost at the resolution limit.

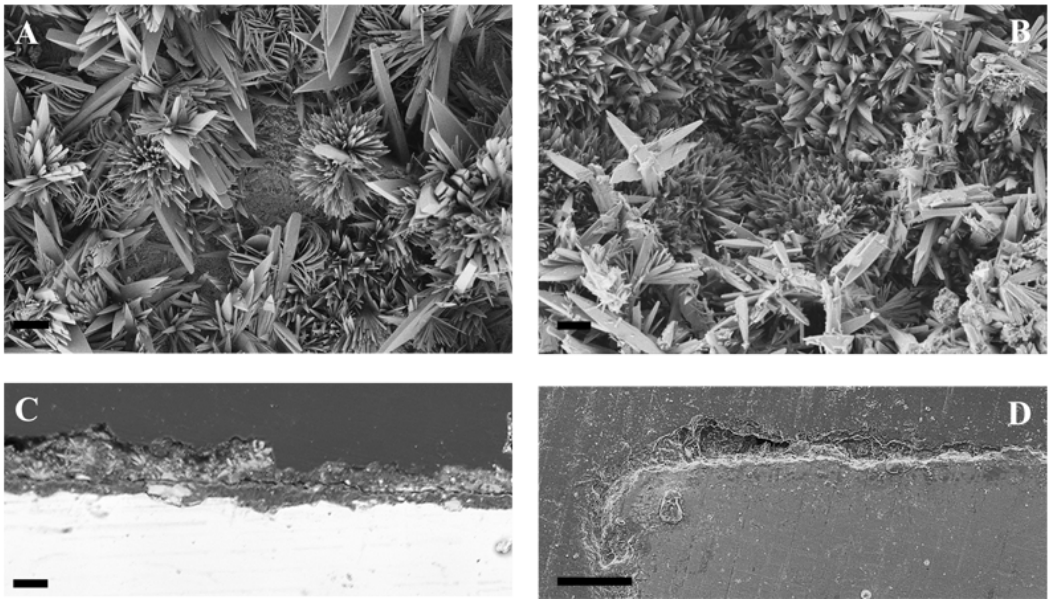

Fig. 2.17 FESEM high-resolution images of sulphates-induced patina growth on CuSn12 reference sample; A) and B) are morphological images of the surface, C) is the longitudinal section of the sample evidencing the thickness of the patina and D) is the longitudinal section taken at the external angle of the sample evidencing the thickness and the shape of the patina. Metric bars: A) and B) 10 μm, C) and D) 20 μm.

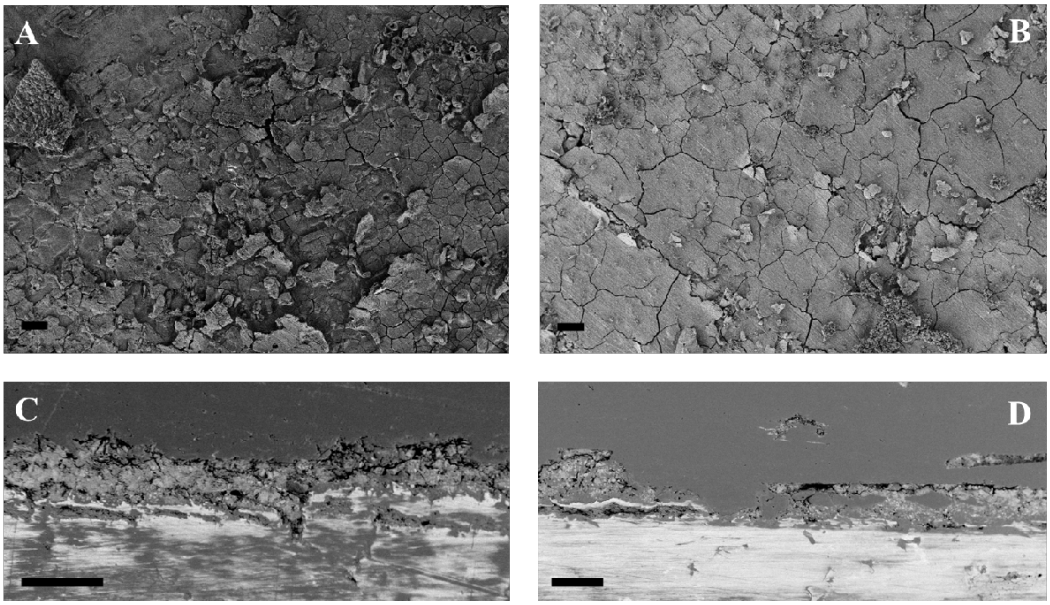

Fig. 2.18 FESEM high-resolution images of chlorides-induced patina growth on CuSn6Pb4 reference sample; A) and B) are morphological images of the surface, C) and D) are the longitudinal sections where is evident the thickness of the patina. All metric bars are 100 μm.

2.4 Calibration of the Neutron Imaging station

The calibration of the Neutron Imaging station installed at the LENA centre was necessary to perform the characterization of metals, as a precise analysis of the constituent alloy. As mentioned above, this calibration required the production and characterization of a set of Cu-based reference samples. The following subsections describe the acquisition of the images and the post-processing, followed by the presentation and discussion of the obtained results.

2.4.1 Acquisition and post-processing

Several measurement campaigns were carried out, also in compliance with the limited daily measurement time (6 hours per day, 4 days per week [40]). Starting from the equation 2.1 previously explained at the beginning of this chapter, all the parameters needed for the calculation of the mass attenuation coefficient will be explained in detail before the image processing. Simplifying the equation by replacing the simple attenuation coefficient with the mass attenuation coefficient, the equation becomes:

$$\frac{\Sigma}{\rho} = \frac{-\ln \frac{I}{I_0}}{x\rho} \tag{2.4}$$

where Σ/ρ is the mass attenuation coefficient that needs to be calculated, I/I_0 is the value obtained from the elaboration of the grey levels from the acquired images, x is the thickness of each sample measured with calibre and ρ is the density of the sample.

Concerning the density of the samples, is described as the sum of the individual density of each element

$$\rho_{\text{tot}} = \sum_j \rho_{\text{j}} \tag{2.5}$$

where the density of each element is calculated starting from the chemical composition obtained from OES measurements. The density of the alloy can be written as follows:

$$\rho_{\text{alloy}} = \sum \rho_{\text{element}} \times wt\%_{\text{element}} \tag{2.6}$$

The tabulated densities of the chemical elements used for the calculation of the resultant alloy density are listed in Table 2.4.

Density of Cu ($g/cm^{3)}$)	Density of Zn ($g/cm^{3)}$)	Density of Sn ($g/cm^{3)}$)	Density of Pb ($g/cm^{3)}$)
8.92	7.14	7.31	11.34

Table 2.4 Density of the main constituent elements of Cu-based reference samples, from *The National Library of Medicine NIH*.

Regarding the associated uncertainty, since the density is an intrinsic characteristic of the element it does not present indeterminacy; the calculation of the uncertainty on the total density of the alloy is as follows:

$$\Delta\rho_{\text{alloy}} = \rho_{\text{element}} \Delta wt\%_{\text{element}} \tag{2.7}$$

Proceeding towards image acquisition, the positioning of the samples represents a key moment before the acquisition of the images. This configuration on the aluminium sample holder (Figure 2.19) allows simultaneous multiple sample acquisition. The samples are fixed with hot glue to the holder, leaving the central part of the sample without glue. This ensures that the central area of the sample is free from any external interference during the measurement and, moreover, for the image processing. In addition to single disk samples and those with patina, greater thicknesses were analyzed by recomposing the ingot (therefore not only with the same chemical composition but also belonging to the same initial ingot) in order to also study the influence of the thickness on the coefficient.

The parameters set for the acquisition (with 10 mm pin-hole collimator aperture) of images are listed below:

- Collimator-sample distance: 1400 mm;
- Sample-scintillator distance: 40 mm;
- Resulting L/D coefficient: 140;
- Best spatial resolution: 150 μm;

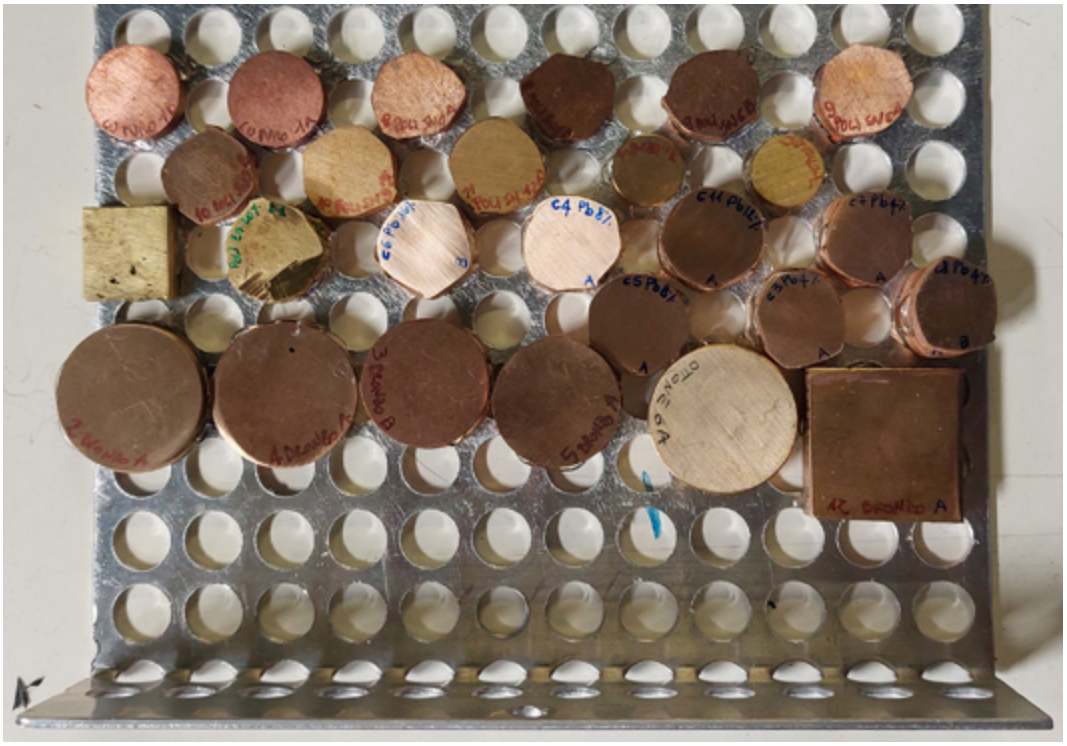

Fig. 2.19 Cu-based reference samples attached (with hot glue) to the sample holder. The sample holder is in aluminium which does not interfere with the analysis.

- Acquisition time: 300 s;
- Best signal-to-noise acquisition time: 1200 s.

Before acquiring images of the samples it is necessary to collect two fundamental parameters which will be used for the image processing: the dark and the white. Basically, the dark is the acquisition of an image with the beam off while the white is the acquisition with the beam turned on.

The image processing was performed using ImageJ (open-source software) in order to obtain the value of the mass attenuation coefficient of each sample from the grey levels of the obtained image. As mentioned before, the first fundamental correction is the dark and white subtraction, thus obtaining the final image to be processed:

$$Final\,image = \frac{raw\,image - dark}{white - dark} \tag{2.8}$$

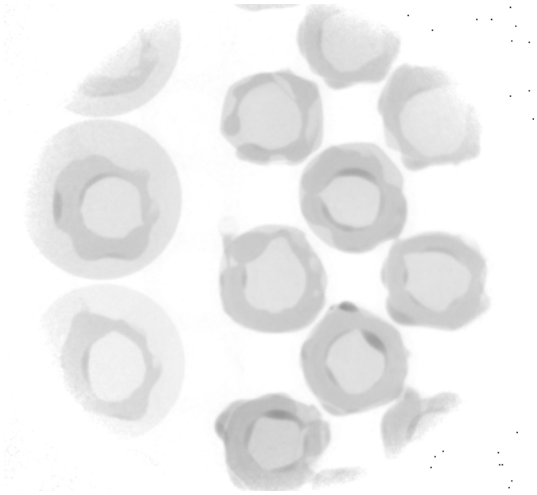

Fig. 2.20 Neutron radiography as it is acquired after the image processing presented in Equation 2.8; the sample holder is moved and the image acquisition continues along the horizontal axis.

The average grey level value for each sample was calculated by considering a 50×50 pixel region of interest (ROI) from the final image (Figure 2.21) in the middle of the sample. Subsequently, the attenuation law (2.4) was used to obtain the mass attenuation coefficients.

According to Equation 2.4, Table 2.5 summarizes all the calculated and measured parameters necessary to obtain the coefficient value for each sample.

In the final uncertainty calculation, all the uncertainties (instrumental and/or associated with the measurement) are taken into consideration so as to be able to propagate the error and calculate an uncertainty associated at each coefficient value.

Parameters needed for the calculation of $\frac{\Sigma}{\rho}$

Symbol	Name	Measured or calculated	Uncertainty
x	thickness	measured by calibre	instrumental
ρ	density	calculated from Eq.2.6	Eq.2.7
$\frac{I}{I_0}$	Intensity ratio	measured from grey level	standard deviation

Table 2.5 summary of the parameters necessary for calculating the mass attenuation coefficient, with their associated uncertainties.

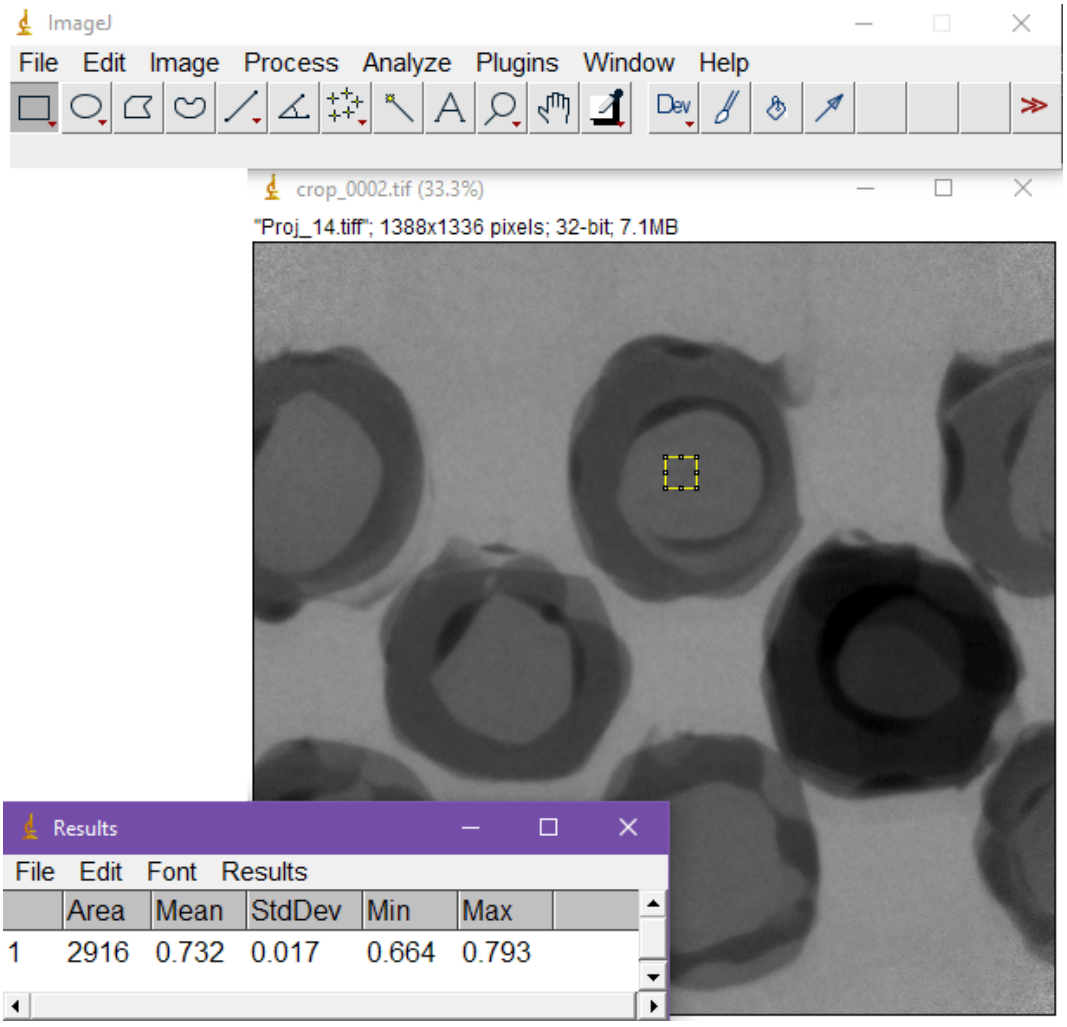

Fig. 2.21 ImageJ interface for the elaboration of images. In yellow is evidenced the ROI of 50×50 pixel in the middle part of the sample. The darker area on the edge of the sample is due to the hot glue used to fix it to the holder during the acquisition of image.

2.4.2 Results and discussion

The technique was employed to analyze various Cu-based reference samples, starting from the specimens without the artificial corrosion patina. Unfortunately, the analyses conducted on the artificially corroded samples did not return good results regarding the evaluation of the influence of the surface corrosion patina. This is because, as already underlined during the characterization of the corrosion layer in subsection 2.3.4, the thickness was lower than the resolution of the system (150 μm) and therefore they were not revealed in the image. The coated samples analyzed in this way were, however, considered in the analysis of the metallic bulk because the patina did not have any influence on the mass attenuation coefficients of the alloys.

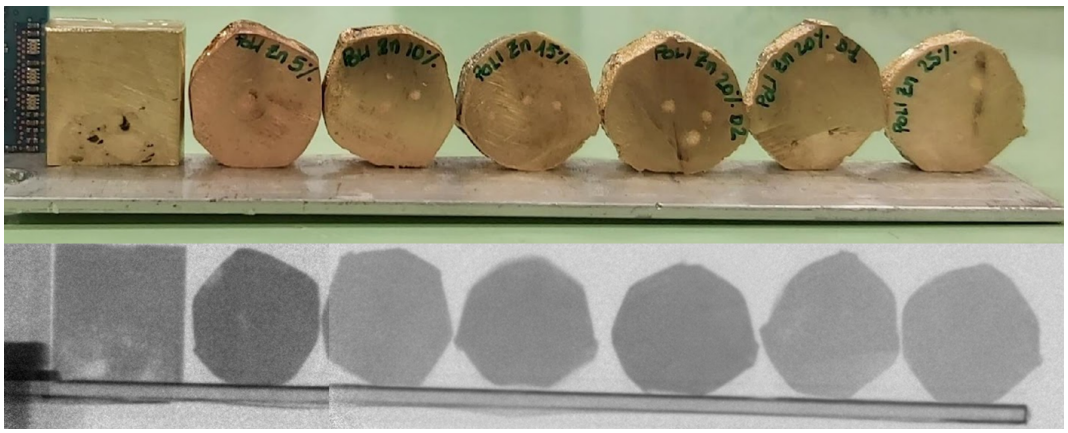

Fig. 2.22 CuZn-reference samples before the analysis (on the top) and the obtained neutron radiograph (on the bottom). In this case, the samples were positioned along a horizontal sample holder then replaced by the aluminium one.

Starting from brass (showed in Figure 2.22), the CuZn specimens show a variance in the attenuation coefficient compared to pure Cu. In the graph (2.23) are rapresented the mass attenuation coefficients in function of the percentage of Cu, having the set of CuZn samples (with a Cu range of 78.6 and 94.7 wt%) and a pure copper sample (Cu 100 wt%). Given that the dominant contribution to the attenuation coefficient comes from Cu rather than Zn, a decrease in the coefficient value was anticipated with higher Zn content in the alloy. As evident from the graph, the discrimination between samples belonging to the CuZn class with an increasing difference of 5% in zinc is not possible at the moment. Also and above all, due to the high associated uncertainty. In fact, further refinement is necessary to minimize errors related to the results and draw more accurate conclusions.

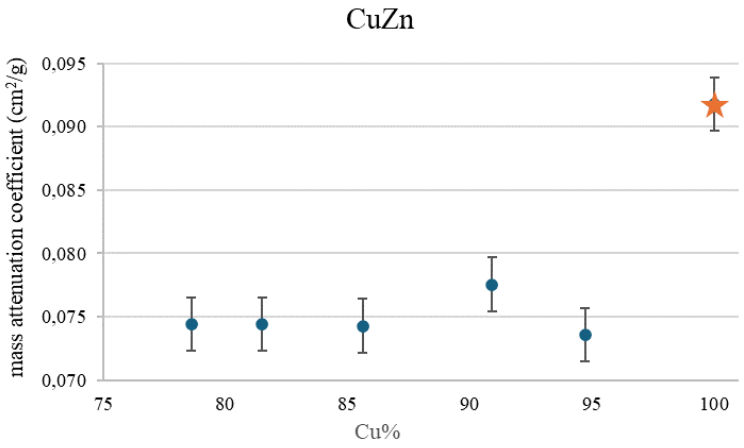

Fig. 2.23 Correlation between Σ/ρ values (expressed in cm^{-2}/g and the percentage of Cu in the samples. The blue points represent the CuZn samples made of crescent percentage of zinc (5, 10, 15, 20, 25 wt% Zn); the orange star is pure copper (100 wt% Cu) used as a comparison.

Concerning tin bronze, the CuSn specimens exhibit an increasing attenuation coefficient value in function of the percentage of Cu. Graph (2.24) represents the mass attenuation coefficients in the function of the percentage of Cu, having the set of CuSn samples (with a Cu range of 88.8 and 92.2 wt%) and a pure copper sample (Cu 100 wt%). Given that the dominant contribution to the attenuation coefficient comes from Cu rather than Sn, is evident a decrease in the coefficient values according to the Sn percentage. It seems to be easier to discriminate between samples belonging to the same CuSn class with a variable increasing difference of 5% in tin. Also and above all, due to the high associated uncertainty it is not possible for example to discriminate samples with small differences, such as CuSn9 and CuSn12 which have a real difference of 2wt% of Cu in the alloy.

Lastly, the leaded tin bronze, the CuSn6Pb specimens present increasing values of mass attenuation coefficient according to the increasing percentage of Cu. As evident from the graph (2.25), where is represented the mass attenuation coefficients in function of the percentage of Cu, the dominant contribution from Cu rather than Pb and Sn induces an increasing value according to the percentage of Cu. As for the CuSn-reference samples, it seems to be easier to discriminate between samples belonging to the same class despite the high uncertainty associated. Moreover, as said above, further refinements will be necessary to minimize uncertainties related to the results and draw more accurate conclusions.

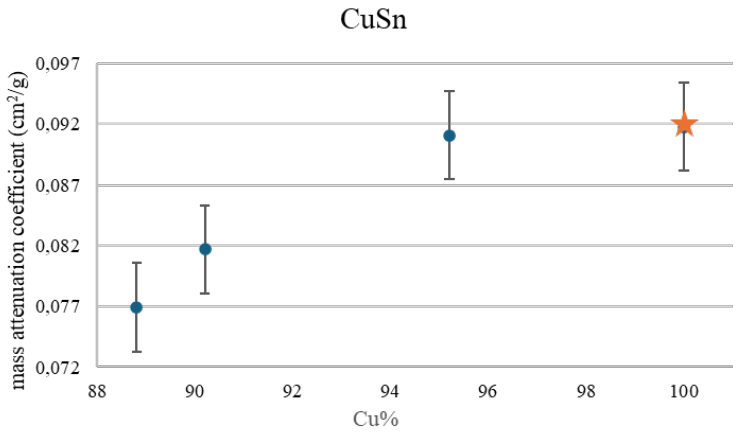

Fig. 2.24 Correlation between Σ/ρ values (expressed in cm^{-2}/g and the percentage of Cu in the samples. The blue points represent the CuSn samples made of crescent percentage of tin (4, 9 and 12 wt% Sn); the orange star is pure copper (100 wt% Cu) used as a comparison.

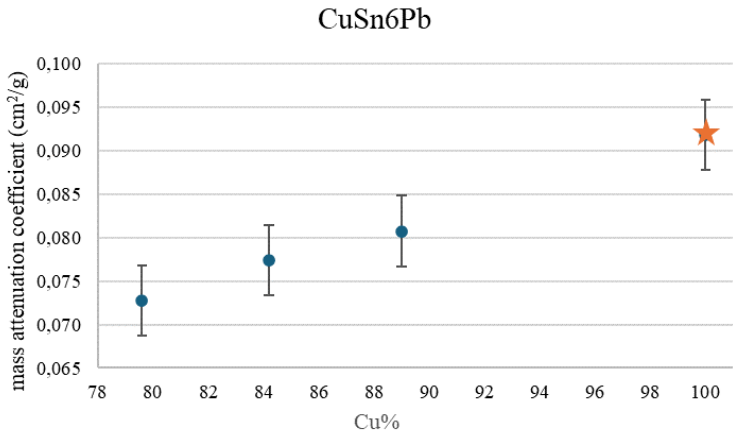

Fig. 2.25 Correlation between Σ/ρ values (expressed in cm^{-2}/g and the percentage of Cu in the samples. The blue points represent the CuSn6Pb samples made of a fixed percentage of tin (6 wt% Sn) and crescent percentage of lead (4, 8 and 12 wt% Pb); the orange star is pure copper (100 wt% Cu) used as a comparison.

Limited analysis was also conducted on artificially corroded samples (Figure 2.26), showing no influence of the corrosion patina on the results. This is evident in graph 2.27, where are reported the mass attenuation coefficients of pure Cu, CuZn20 and three CuSn6Pb4 samples: one of them, is not patinate while the other two have respectively one chlorides-induce patina and one sulphates-induced patina. The radiographic data does not allow for distinguishing between the composition

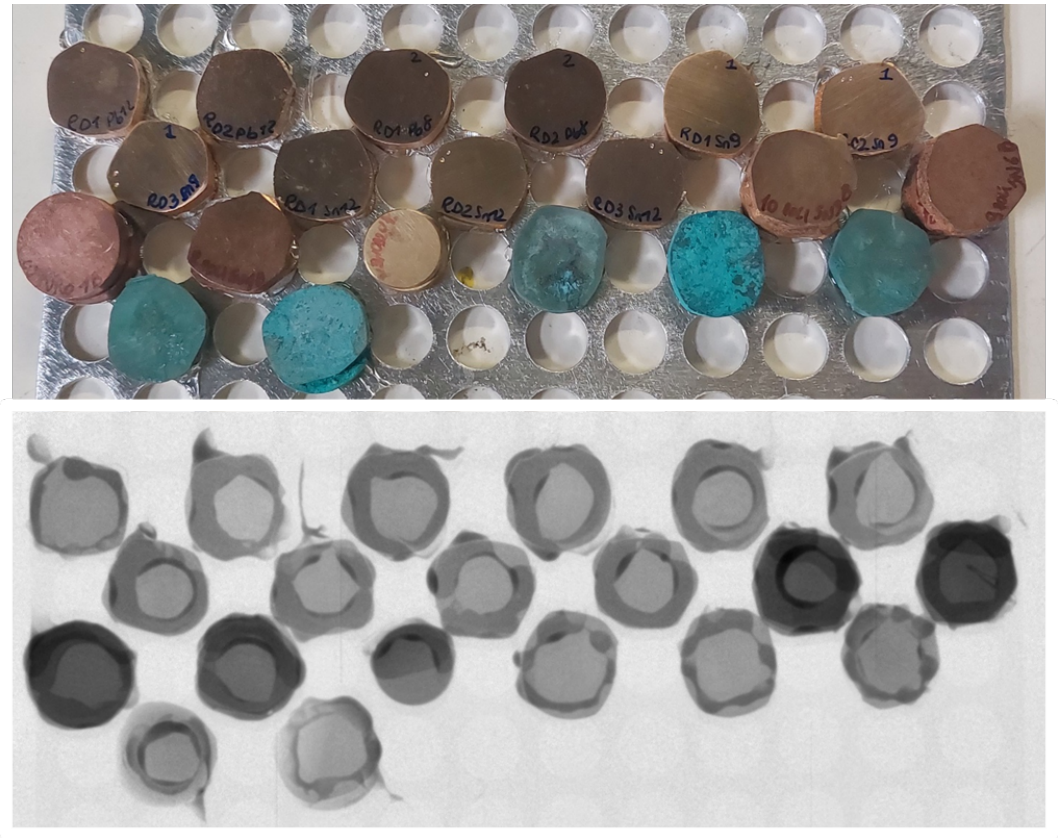

Fig. 2.26 Processed Neutron image of Cu-based reference alloys, as cast and artificially aged. In particular, it is evident that the corrosion prducts layers do not affect the grey level coming from the bulk.

of the patina and the bulk material. Until now, only the distinction of samples with high differences in component percentages is possible. Afterwards, to address this limitation tomographic analyses are planned for the near future to assess the influence of the patina on a 3D model. Thus, conducting 3D tomography is essential to assess the influence of the corroded surface on image quality and to determine the thickness and composition of both the patina and bulk material. The minimum required thickness of 150 μm will be considered for tomography, especially crucial for coated samples with very thin layers of corrosion products, such as those obtained with aqueous solutions containing copper sulfate.

With these results, it would still be interesting to use the Neutron Imaging station to study archaeological metallic artefacts after this preliminary calibration, so as to be able to correlate the mass attenuation coefficient with the chemical composition of the sample. This will be a key point in the future for the development and definitive

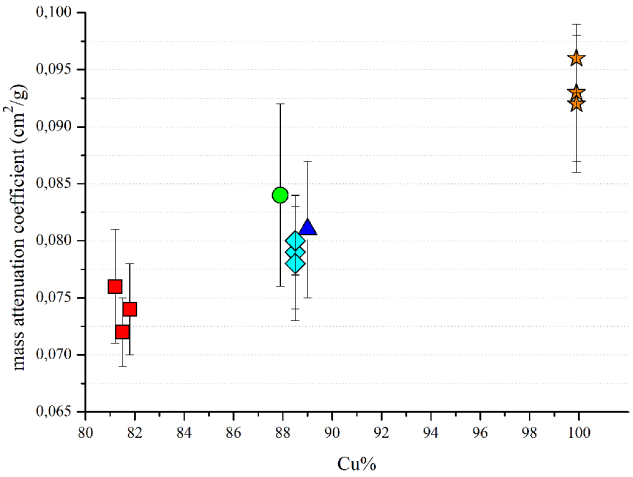

Fig. 2.27 Correlation between Σ/ρ values (expressed in cm^{-2}/g and the percentage of Cu in the samples. The three discriminated groups are represented by CuZn20 (red square), the pure Cu (orange star) and three samples of CuSn6Pb4: coated by sulphate patina (green), coated by chloride patina (blue) and without coating (light blue).

implementation of the imaging station dedicated to Cultural Heritage at the Applied Nuclear Energy Laboratory LENA of Pavia (Italy).

2.5 Conclusions

In conclusion, Neutron Imaging shows promise in characterizing binary CuSn and CuZn, and ternary CuSn6Pb samples, but further investigation is needed for corroded samples. Nevertheless, there would be a need to carry out many more measurements and acquisitions to try to reduce the associated uncertainty to allow discrimination even at low concentration differences. This large uncertainty is due to the wide propagation of the error that occurs starting from different experimental and theoretical measurements, which therefore increases the error associated with the final value (the mass attenuation coefficient).

A separate discussion must be made for artificially corroded samples, which require a preparation that induces a more consistent layer on the surface to be comparable with the resolution of the instrument. As already mentioned above, it

could be interesting to carry out tomographies to try to evaluate not only the influence of the layer but also the resulting morphology.

The main limitations underlined are essentially the following: the limited time of measurements which certainly affected the number of images acquired on the samples, the high value of associated uncertainty which does not allow a precise discrimination of low difference of composition. This could be overcome adding new set of Cu-based reference alloys to acquire a greater number of samples to decrease the associated uncertainty, being able to discriminate small differences in the composition.

Unfortunately, for now, it is impossible to carry out measurements on real artefacts, since the radioprotection regulations are very stringent and it would be necessary to carry out a quarantine of six months for the artefact. In fact, the current legislative Decree D.Lgs 101/2020 and subsequent additions have made heavy changes as well as improvements in radioprotection, especially regarding the management of objects irradiated by ionizing radiation. Although neutrons are not ionizing, they can effectively activate materials, thus inducing the production of ionizing radiation (such as α-, β- and γ-radiations).

In this way, objects analyzed with neutrons are treated as radioactive and must undergo a rather long quarantine (which depends on the constituent material, on average six months) before they can be brought back. This could be a huge limitation, especially in the study of archaeological artefacts, which should remain in quarantine for a long time after the analysis.

Chapter 3

Reflectance Transformation Imaging

This chapter provides an overview of the Reflectance Transformation Imaging technique, its principles, applications, and significance in the field of Cultural Heritage preservation and research. Right away, the methodology used for the development and the test of the UVL-VIS system is therefore presented, starting from the design of the 3D printed dome and development of the LED control system up to the acquisition of the images, with the consequent discussion of the results obtained.

Some of the work described in this chapter has been previously published in [59].

3.1 Introduction and theory

Reflectance Transformation Imaging (RTI) is an imaging technique that has revolutionized the way of documenting and analyzing the surface details of Cultural Heritage artefacts, including not only objects but also architectural features and buildings. Since its discovery in the early 2000s [60] it has been widely used for documentation and has undergone continuous improvements to adapt to the demanding needs and, above all, the technological enhancements. "RTI imaging is nowadays very promising due to the possibility to develop cheap and portable instrumentation for *in situ* measurements even if the technique is still not characterized in terms of correlation and a repeatability analysis of the acquired images."[59]. The fact that it is a non-invasive and non-destructive technique has led to a widespread use, allowing it to be used on a wide range of materials and conditions [61]. "In the last decades the technique was widely used for the study and documentation of different

Cultural Heritage materials: cuneiform tablets [62] [63], fossils [64], use-wear on prehistoric bones tools and lithics [65], numismatics [66][67], rock art [68], graffiti [69], statuary [70], metallic artefacts [71], textiles[72] and so on."[59] Moreover, the possibility of creating interactive and 3D visualizations of the surface allows the manipulation of the virtual replica revealing texture variations, intricate surface features and, sometimes, hidden details.

As will be explained in more detail later, the underlying principle of RTI is the acquisition of a series of digital photographs of an object varying in the direction of incident light recording the different surface responses using a fixed camera. These images are then processed using specialized software to generate a virtual replica that can be interactively manipulated by the viewer, changing the direction of the incident light.

The basic setup of RTI includes a digital camera and a light source. Based on the conformation, some setups may have mechanisms for rotating the object, fixed or moving lights (i.e. LEDs or flashlights), dome or arches where to fix the light, and so on. Precisely because it is a technique that is always improving, it is not easy to define a standard setup. Despite that, some setups are shown in Figure 3.1. Both the systems have a fixed camera orthogonal to the sample; in the highlight-based system, the acquisition is made by moving the light (i.e. a camera flashlight) around the sample designing a hemisphere and the position of the light is detected thanks to a black-sphere [73] positioned near the object while the dome-based system has numerous fixed lights positioned on the arches of a dome. The digital images captured from multiple lighting angles are processed using mathematical algorithms to calculate the surface normals and reflectance properties of each pixel, resulting in a detailed and interactive representation of the surface of the object, highlighting the shape, possible reliefs and roughness. Nevertheless, the ongoing enhancements are aimed at the multispectral setups that can perform the acquisition of multispectral images obtaining different information.

To better understand how the technique works it is necessary to make a brief introduction on the interaction of light (above all, visible and Ultra Violet) with matter and, subsequently, explain the reflection phenomena which are fundamental for the acquisition of this type of images. The most complete description of the interaction between an opaque surface and light is given by the Bidirectional Reflectance Distribution Function (BRDF). BRDF is basically used to describe how light is

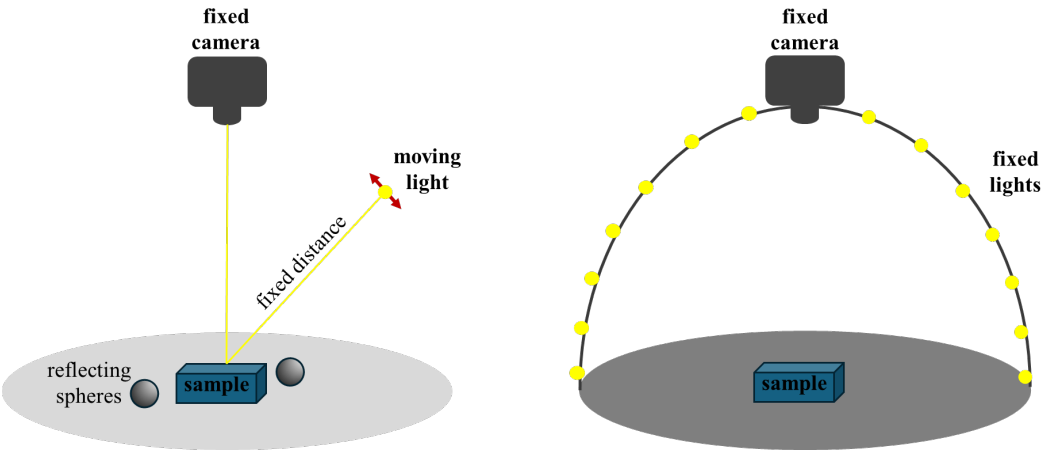

Fig. 3.1 Example of the most used RTI system: highlight-based (left) and dome-based (right) systems. The biggest difference between the two is the lighting: the first one has a movable light that moves on a hypothetical hemisphere at a fixed distance while the second one is equipped with several fixed lights on the arches of a dome.

reflected from a surface in relation to both the direction of incoming light and the direction of outgoing reflected light.

BRDF depends on various factors, including the surface material properties (e.g., reflectivity, roughness), the incident light spectrum and polarization, and the surface geometry. BRDF can be obtained by using sophisticated measurement devices (i.e. gonioreflectometer [74]) thus making the measurement extremely long, expensive and above all the luminance is acquired in a single point. Despite that, this modelization permitted to develop and improve new methodologies [75] [76] and algorithms to describe the interaction between light and objects. These advances have led to the development of new techniques, such as RTI, which exploit this relationship between luminance and light reflection to study the morphology of the surface.

The angular component of reflectance is parameterized by correlating per-pixel luminance with the incident light. Various implementations of the Reflectance Transformation Imaging (RTI) method are documented in the literature, facilitating data processing. The most commonly used functions include Polynomial Texture Mapping (PTM) and Hemispherical Harmonics (HSH).

"The PTM method developed in 2001 [62] uses a bi-quadratic polynomial equation described in Eq. (3.1) to calculate the luminance (L) for each pixel representing the object:"[59]

$$L(x,y;l_x,l_y) = a_0(x,y)l_x^2 + a_1(x,y)l_y^2 + a_2(x,y)l_xl_y + a_3(x,y)l_x + a_4(x,y)l_y + a_5(x,y) \tag{3.1}$$

"where l_x and l_y are the components of light direction obtained by projecting the normalized vector on a reference plane; the a_0 to a_5 bi-quadratic luminance coefficients are obtained using a multiple regression from the acquired images. In each photograph, each pixel has six descriptors which allow to calculate the light direction from a finite set of images."[59]

"Instead, the HSH method [77] improves the PTM method by adding a space based on hemispherical harmonics described as H^m_l:"[59]

$$H_l^m(\theta,\phi) = \begin{cases} \sqrt{2}K_l^m cos(m\phi)P_l^m(cos\theta) \\ \sqrt{2}K_l^m sin(-m\phi)P_l^{-m}(cos\theta) \\ K_l^o P_l^o(cos\theta) \end{cases} \tag{3.2}$$

"where l is the order and m is the degree of the harmonics, ϕ and Θ are respectively the angles between the view direction and the light direction and the angle between the projection of the luminance of a pixel characterized by x and y coordinates; P^m_l is the Legendre's polynomial. Using this model it is possible to calculate the contributions in the space of harmonics."[59]

As mentioned before, the reflectance properties are described by BDRF [78] that permits to obtain a virtual replica of the object, that can be re-lighted to enhance some particular. The information about the morphology of the surface comes from the correlation of the contribution to reflected radiance to incident irradiance.

The advantages of RTI method are several:

- non-invasive and non-destructive technique which allows to obtain an interactive virtual replica of the object;
- provides a precise and clear representation of the surface;
- the virtual model can be used for a deeper study of the object, without the need of the object itself. This point is fundamental for the documentation of artefacts;

- it can be used *in situ* avoiding moving the object.

3.2 Development of innovative UVL-VIS RTI system

To perform at the same time both visible and ultraviolet RTI imaging, a dome-based system was developed. This is a great upgrade as it is possible to have information about the substrate (e.g. past restorations, texture, subsequent modifications, composition) other than the surface aspect. As will be explained later, the setup manages to maintain a fairly low cost, it is easily transportable and, in the future, a further upgrade will be made with the infrared acquisition. In the next paragraphs, all the steps for the development of the dome-based system will be explained.

3.2.1 3D printed dome

The first step involved the design and subsequent 3D printing of the dome. The software used to develop the dome was the OpenScad open-source software, designing a dome with a diameter of 20 cm and an apical opening (suitable for the camera during the acquisition of images) of 5 cm. The small dome size allows to easily move the system, but at the same time permits to acquire images only on small objects (less than 10 cm). The project is shown in Figure 3.2. Finally, the dome was printed in laboratory by using a single-extruder 3D printer (model WASP2040, WASP) in black polylactic acid (PLA). The black PLA permits to obtaining a dome suitable for the acquisition of VIS and UV images.

3.2.2 Visible and ultraviolet LEDs

The fixed lights, consisting of eighteen white LEDS and eighteen ultraviolet LEDS, were positioned in the following arrangement: twelve arches (one arch VIS, one arch UV, alternatively) and three rings with twelve LEDs per ring (six VIS, six UV). In Figure 3.3a is presented the schematic representation of the developed setup with indications on the positioning of the LEDs. The result of the arrangement of all the LEDs is shown in Figure 3.3b. regarding the camera, the main aim was to maintain a low cost of the system and in parallel to obtain images with a good resolution for the

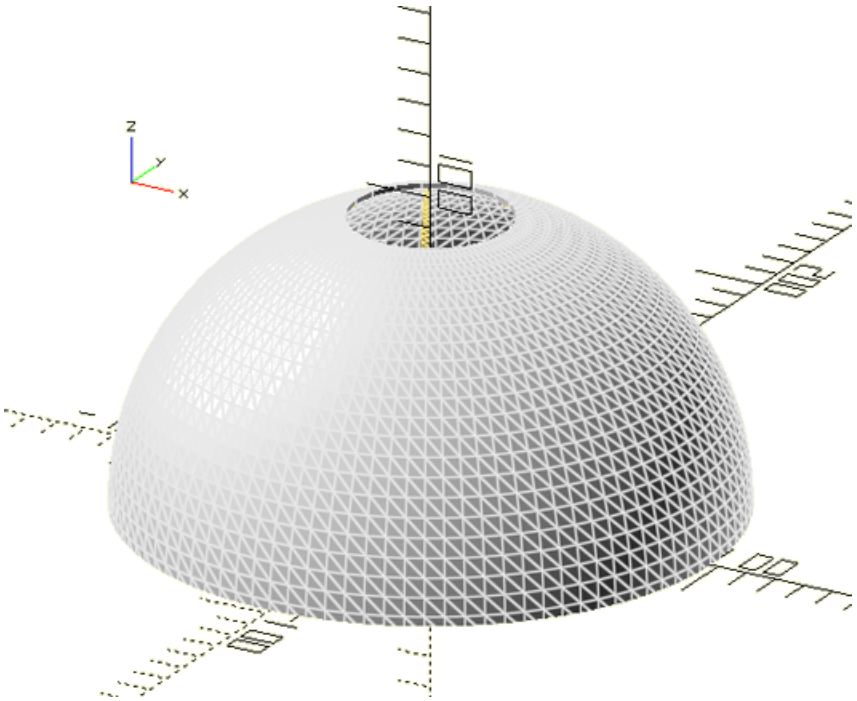

Fig. 3.2 Dome project for the RTI acquisition from OpenScad opensource software

processing. For this purpose, an ordinary smartphone was chosen. The camera has a resolution of 64 MP, f/1.8 and can be easily remotely controlled.

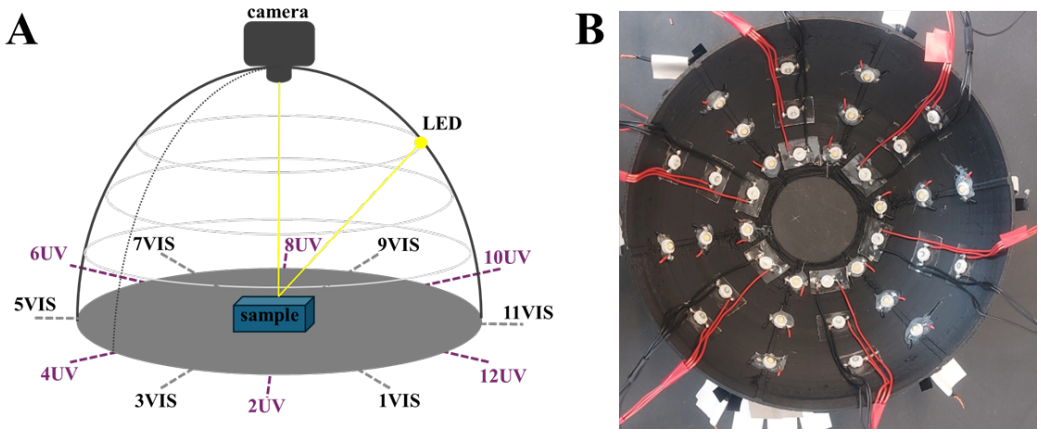

Fig. 3.3 A) Schematic representation of the dome-base system and B) disposition of the LEDs inside the dome.

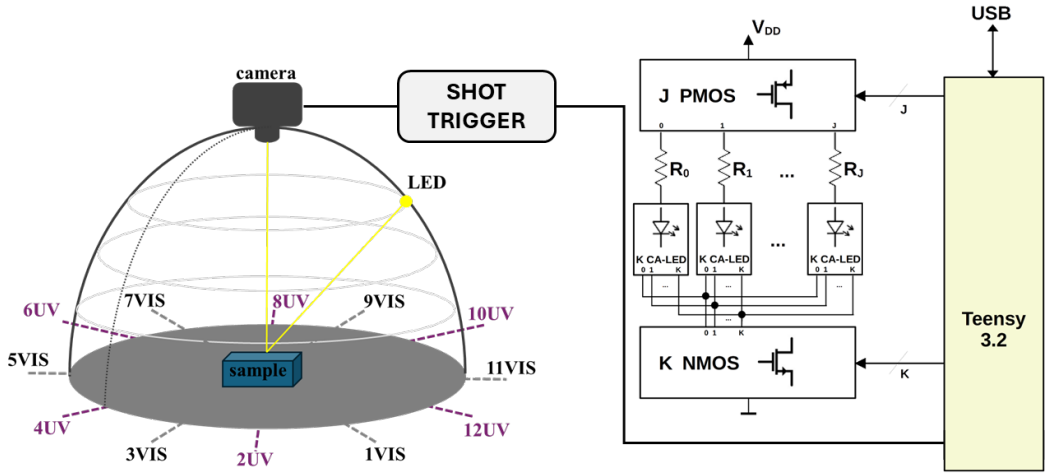

Fig. 3.4 Schematic circuit of the LEDs control system linked to the dome-based system.

3.2.3 Control system

"In order to easily control the state of each single LED a dedicated LEDs Control System was developed. This simple system allows to individually switch on and off the LEDS and automatically send a shot trigger to the employed camera, thus making the whole process of taking several photos straightforward and effortless. The system, shown in Figure 3.4, is arranged around a Teensy 3.2 microcontroller board [79], a small but powerful development board which features a rich set of peripherals and quite good computing performance."[59]

"The LEDs employed as light sources inside the dome were connected following their displacement as rings and arches. In particular, the LEDs connected in one ring have their anodes connected together, while the cathodes are connected according to the arch. This creates a J×K matrix-like connection for the LEDs which simplifies the wiring and reduces the number of switches required to control the LEDs. The control of each LED is carried out by using J PMOS switches connected to the common anodes of the rings and K NMOS switches connected to the cathodes of each arch. The activated LED is therefore the one seeing the corresponding couple jk of switches activated. The current flowing in the LED is controlled by the series resistors Rj and the Vdd voltage is provided by an external power supply (Vdd = 5 V)."[59]

"Generally, given a dome with J rings and K arches, the number of switches required to control the J×K LEDs is equal to J+K, thus reducing significantly the

number of devices required to control the LEDs, especially when the number of LEDs is larger."[59] The developed system has 3 rings and 12 arches, so J=3 and K=12. The number of MOS switches is 15, turning on and turning off a total of 36 LEDs. The proper current needed to correctly work at the 80% of the rated power is about 250 mA, having the used LEDs with a power rating of 1 W.

"The firmware onboard the Teensy microcontroller periodically cycles turning on a single LEDs each time and sending a shot trigger signal to the camera as soon as the selected LED has been turned on. Thus, the camera takes a photo of the artefact. After a few seconds, the LED is switched off and the cycle repeats LED by LED until all photos have been taken. In general, the shot trigger circuit depends on the specified camera employed in the setup. For cameras supporting mechanical remote shot buttons, the system is basically composed of a single open drain MOS which is directly connected to the camera shot input. Instead, for smartphone cameras, the system is realized by hacking a commercial Bluetooth selfie stick so that the shot button on the handle is replaced by the shot trigger MOS connected to the Teensy. The designed system is easily scalable to different LEDs configuration and allows the operator to quickly acquire a large set of photos without manually switching the LEDs."[59]

3.2.4 Acquisition of images and post-processing

All images have been acquired using the same fixed camera parameters. The parameters set for the acquisition of the RTI images are listed in Table 3.1.

Camera acquisition parameters		
ISO	shutter speed (s)	aperture
500	1/25	f1.8

Table 3.1 Camera parameter used for the acquisition of RTI images.

The sample is positioned under the camera aperture and photographed first under VIS light and then under UV light. The whole system is automated so the sample does not need to be moved between one acquisition and another, thus allowing the comparison of the images obtained with VIS and UV lights. Before taking the photos of the sample, a first measurement is carried out with a reflecting black sphere (without the sample) to obtain the exact position of the lights during the acquisition to

facilitate image reconstruction. This allows to have a precise position of the lighting source without having to derive it at a later time. The light position file can be loaded directly into the software before the post-processing.

Afterwards, for each selected sample a total of 18 VIS images and 18 UVL images were acquired. To colour balance the images, a calibrated colour reference (Calibrite ColorChecker classic, x-rite) was used before image acquisition 3.5. This image processing will be carried out on each image with RawTherapee open-source software before using the software to build the RTI model.

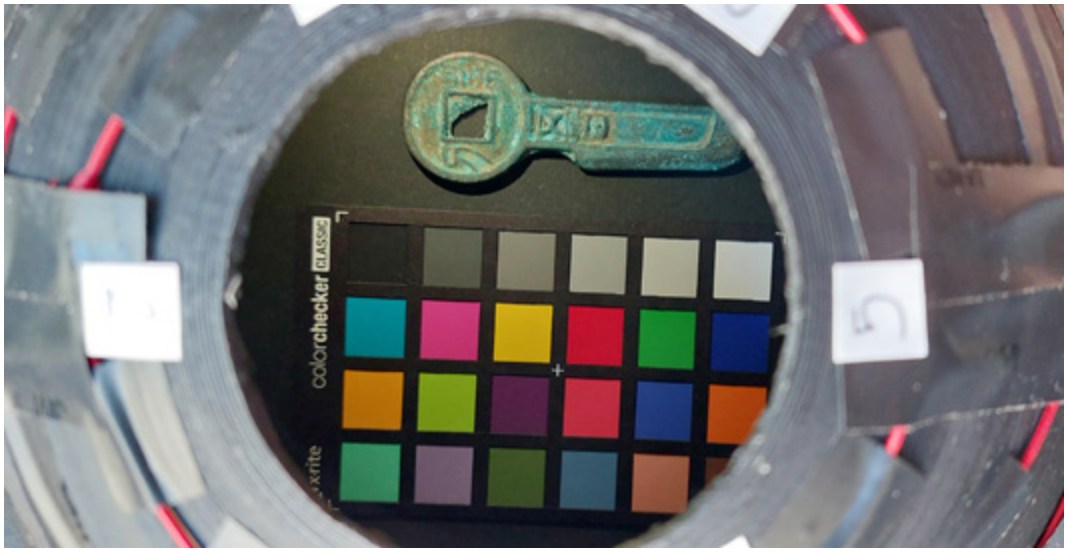

Fig. 3.5 Top view of the dome from the apical camera aperture. Particular of the acquisition of a sample with the reference to balance the final colour.

The RTI virtual model is assembled with RTIBuilder open-source software (CHI, Cultural Heritage Imaging). As mentioned before, the precise position of the LEDs was acquired by using the black reflective spheres; the position file was loaded in the software before the processing. Then the 18 acquired images were loaded on the software, which processes all the data applying Equation 3.1 for the PTM algorithm and Equation 3.2 for the HSH algorithm described in Section 3.1 leaving the choice to the user as to which algorithm to use.

The RTI model can be opened and manipulated with RTIViewer open-source software (CHI, Cultural Heritage Imaging) (Fig. 3.6). In fact, as can be seen in Figure the software enables the interactive control of the model. The operator can manipulate the scene by changing firstly the light directions (moving the cursor on a

hemisphere) and then the surface characteristics can be arranged to obtain specific image effects.

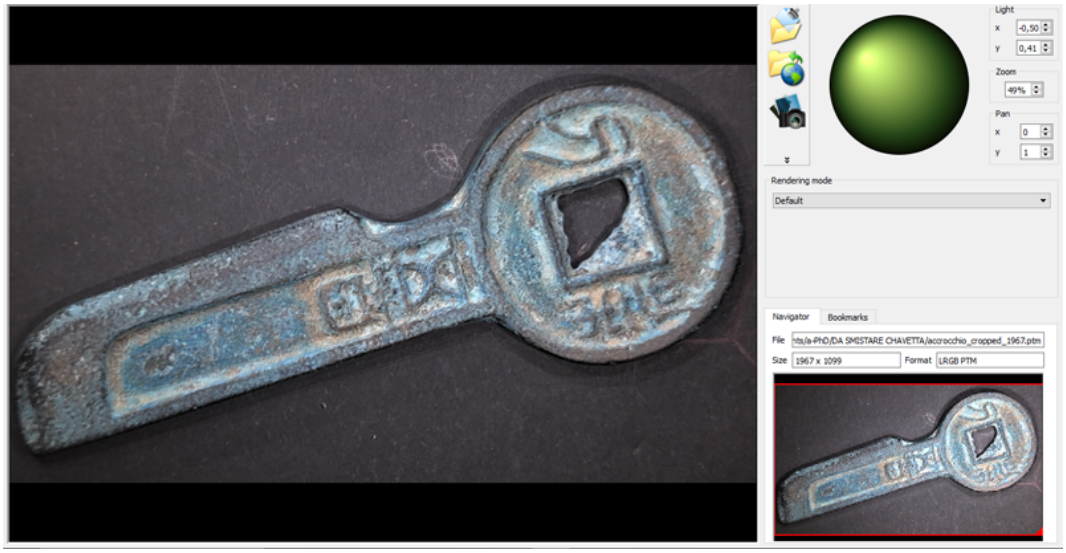

Fig. 3.6 RTIViewer interface used for the manipulation of the RTI model. The green light on the sphere represents the incident light which can be moved along the hemisphere.

These arrangements are possible because each normals value in the image is correlated to a precise point on the object which is characterized by the angle of reflectance of light recorded from any direction. The enhancement tools are mathematical transformations to the surface normals and not to the colour information.

This arrangement allows the improvement of the examination of the surface enhancing details and shapes. The available rendering modes will be explained below:

- Default: no mathematical enhancement;
- Specular enhancement: can separate the contribution of different specular reflections;
- Diffuse gain: enhances the perception of surface shape features, increasing the directional change of normals directions. Above all, it increases the perception of roughness;
- Normal unsharp masking: enhance the high-frequency details and increase the edge contrast of the image, looking for discontinuities in the data that indicate edges in the image;

- Normals visualization: creates a false-colour rendering that represents the pixel-by-pixel surface orientation. The normal direction at each pixel is characterized by a particular colour which indicates a different orientation.

A bulleted summary list with the main steps for the correct acquisition of images is presented below.

1. Measurement of the light positions by using the black reflecting sphere;
2. Acquisition of image with the sample for colour balance (pre-processing);
3. Acquisition of 36 images at different light positions (18 VIS and 18 UV);
4. Post-processing with RTI builder software;
5. Opening of RTI model with RTI viewer software.

3.3 Case study: Chinese bronze coins

In consideration of the testing of the developed RTI setup, some Chinese bronze coins were selected for the purpose (Figure 3.7). An introduction to the samples will be briefly given below. Ancient Chinese bronze coins hold a significant place in the history of Chinese civilization and numismatics, offering valuable insights into the economic, social, and political dynamics of ancient China. This introduction provides an overview of ancient Chinese bronze coins, their evolution, significance, and cultural importance considering the lack of information about the provenance of the samples.

China presents some of the earliest documented instances of metal coinage. Historical evidence suggests that cowrie shells were utilized in some capacity as exchange currency. Subsequently, these shells had been supplemented with imitations crafted from materials such as bone, jade, and, notably, bronze. In some regions, was also employed gold coinage. During the later pre-imperial era of China, alongside the conventional circular coins, various other forms of coinage were in circulation. Among these, the earliest known form is the Hollow Handled Spade, resembling an agricultural tool. Another distinctive form of pre-Qin coinage is knife and spade money, which mimics the shape of knives. Several types of knife are present,

Fig. 3.7 Samples selection for the RTI acquisition.

depending on the region. Lastly, the circular coin, often featuring a square hole at its centre, represents the final major category of pre-Imperial coinage. A notable feature of Chinese copper alloy coinage is its method of production. In contrast to contemporary coinage found elsewhere in Eurasia, Chinese coins were cast in moulds, with any inscriptions being incorporated into the moulding process [80] [81].

Today, ancient Chinese bronze coins are highly prized by historians and collectors. They are sought after for their historical value, artistic beauty, and rarity. Collecting and studying ancient Chinese bronze coins provides a unique window into the rich tapestry of Chinese history and culture, spanning thousands of years of continuous civilization.

3.3.1 Raman spectroscopy

Before the acquisition of the RTI images, Raman spectroscopy analyses were carried out on the surface of the bronze samples to map the corrosion products. All the Raman acquisitions and subsequent processing were made by using the same protocol previously presented in Chapter 2. However, some acquisition parameters were adapted to the morphology of the sample; the parameters are summarized in Table 3.2

Raman 532 nm				
Acquisition range (cm^{-1})	Resolution (cm^{-1})	Integration time (s)	Repetition (time)	Laser power (mW)
150-4200	5	15	5	15

Table 3.2 Parameter set for the acquisition of Raman spectra, by using BWTEK iRaman Plus 532 nm.

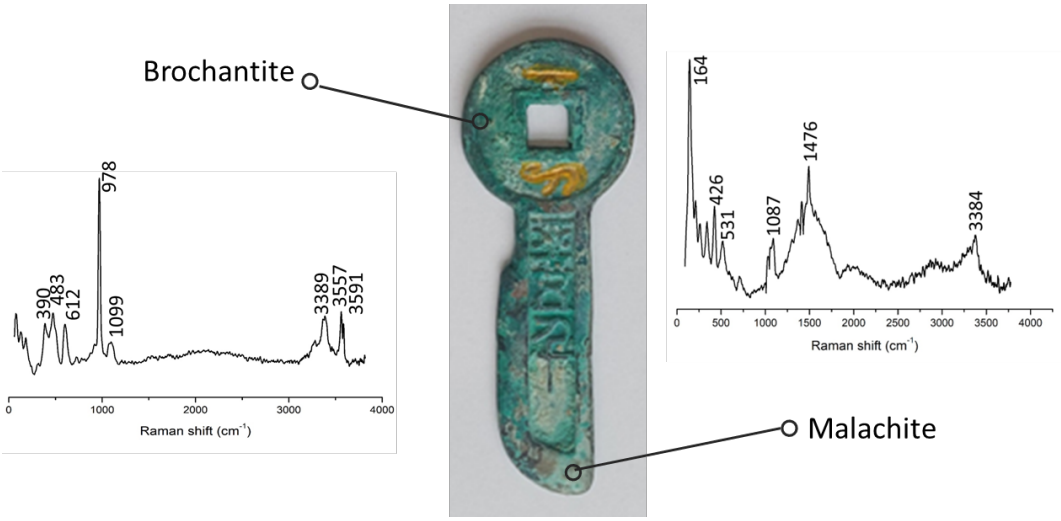

Fig. 3.8 Results of Raman spectroscopy on sample M03. The spectra of brochantite and malachite are shown near the point of analysis.

Some examples are presented below. In particular, in Figure 3.8 are presented the spectra obtained on a bronze "knife" coin (sample M03). The analisis underlined the presence of two main corrosion products: brochantite with its characteristic Raman peaks (313, 485, 630, 916, 976, 3417, 3589 cm^{-1}) and malachite, which is a copper carbonate hydroxide with its characteristic Raman peaks (164, 426, 531, 1087, 1476, 3384 cm^{-1}.

3.3.2 UVL-VIS RTI images acquisition

All the samples were photographed under the dome, acquiring the 18 VIS + 18 UVL images to reconstruct the VIS and UV models. Starting from the acquisition in visible light, the RTI models obtained have good precision and quality of the images. The surface can be easily manipulated to obtain the expected effects. In particular,

in Figure 3.9 are presented the most significant results obtained as VIS RTI images, acquired at the same light position.

As it is possible to observe, all the available rendering modes were used to see the effect on the surface aspect. The surface's roughness is enhanced and it was possible to highlight particular which were not particularly visible. "All the shapes are well-highlighted, even the less marked ones. The default image is optimal for surface documentation. The other transformations are useful for a deep study of the surface. In the diffuse gain, the depth and height of the shapes are increased, forming a black-and-white image. In the specular enhancement, the diffuse/specular effects are improved in order to make more visible the texture of the surface. The normal unsharp masking increases the surface edges, combining the surface data and the edge contrast. Lastly, the normals visualization can provide information about the dimensions of the surface shapes, using color changes. These RTI results show how the use of a low-cost setup with only three LEDs per arc is sufficient to create precise images of the surface. The PTM method, having fewer complex parameters, showed grainy images, especially in those created by normals vectors (normals visualization)."[59]

Close inspection of Figure 3.10, reveals how the UVL acquisition can improve the information on the surface of the samples. In fact, in addition to all the information already highlighted by the VIS light, it is possible to see areas that are more or less luminescent. This luminescence is induced from the UV lights depending on the composition of the surface. In agreement with previous Raman acquisitions, it was possible to state that the luminescent areas present a greater presence of malachite. In contrast, those that are not luminescent are essentially made up of brocantite.

This last point is of fundamental importance as the virtual UVL RTI model, in addition to providing information on the morphology of the surface, may be able to provide information on the surface composition. It is important to underline that before applying the method to different materials, it is necessary to acquire a database that correlates the surface luminescence with the chemical composition (using Raman spectroscopy or other methodologies).

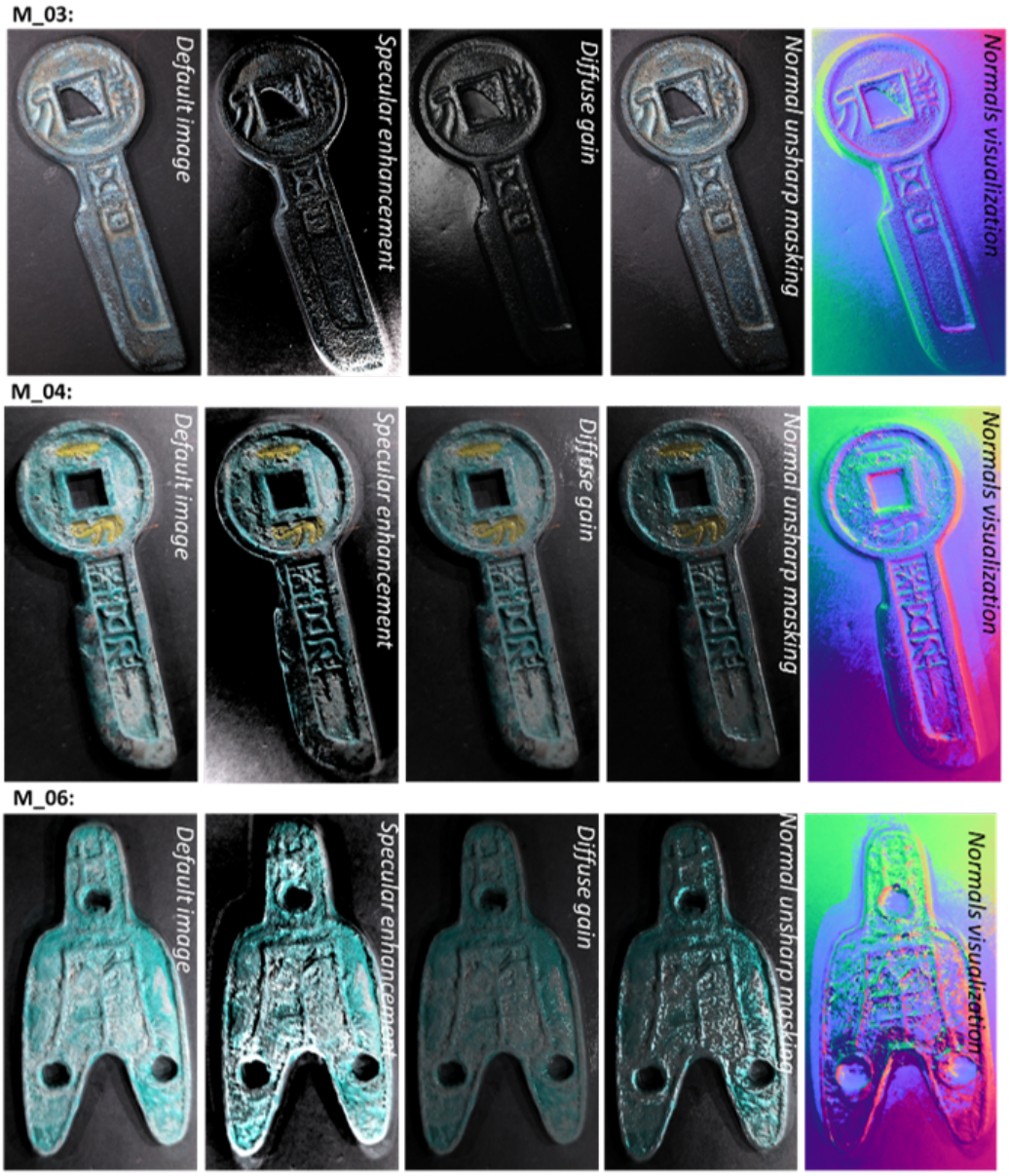

Fig. 3.9 VIS RTI models of three different samples.

Fig. 3.10 UVL RTI model

3.4 Conclusions

A low-cost and portable system to perform both VIS and UVL RTI imaging was developed with very promising results. The system, consisting of a 3D-printed dome with 36 LEDs (18 VIS and 18 UV) was able to provide very good RTI models, in terms of quality of images and surface characterization. The subsequent virtual manipulation of the light allows to document the morphology of corrosion layers and, in addition, to study the surface of the artefact. The system, after a proper testing, is potentially usable for dimensional purposes, adding this type of information at the complex RTI system.

Despite the numerous positive aspects (i.e. non-invasive and non-destructive, low-cost, portable, automatic) the system presents some limitations. In particular, the main limitation depends on the dome size which allows the analysis of samples with dimensions up to about 10 cm, taking into account also the camera focus problem. This limitation should be able to be improved, for example increasing the diameter of the dome, thus losing the easy portability of the system.

It is important to underline that the use of a black dome makes possible the improvement of the system to a multispectral acquisition, adding infrared acquisition. In this case, the cost would increase as it would require a camera with a sensor suitable for IR acquisitions.

What it has turned out until now, is that the system has high potential in the creation of RTI virtual models where surface morphological details and chemical compositions are available together, especially with regard to the characterization of the sample surface intended as a corrosion surface. Before being able to apply the system to different materials, it will be necessary to create a database to have precise data available for sample identification.

Chapter 4

Case studies

In this chapter, two works carried out at the early beginning of the doctoral period will be presented. Mainly, the use of Raman spectroscopy is used for the assessment of the conservation state of several metallic artefacts. In particular, in 4.1 the development of a measurement protocol to characterize several archaeological iron nails from Tharros (Sardinia, Italy) will be presented. Afterwards, in 4.2 Raman spectroscopy is used to evaluate the effectiveness of protective treatments after the artificial ageing process.

Some of the work described in this chapter has been previously published in [82] and [83].

4.1 Characterization of iron archaeological artefacts

When a metal artefact is extracted from the archaeological excavation, where it has remained buried for a long time and where it has potentially reached an equilibrium with the environment, there is the risk that the corrosion process can be reactivated leading to a rapid and inevitable deterioration of the artefact. As already widely discussed in the previous chapters, is fundamental to study the artefact to understand the type of corrosion it has undergone and, above all, evaluate a strategy to safeguard the object by preventing it from further degradation.

As already extensively discussed in the Introduction 1, the choice of diagnostic investigation depends on the type of information you want to obtain, and above all,

on the type of material being analysed. Concerning the study of archaeological iron, there are numerous studies that use Raman spectroscopy as an analysis methodology to characterize corrosion products [84] [85] [86].

In this scenario, it was tried to develop a dedicated measurement protocol that permitted the identification of a sort of "map of corrosion products" without causing any damage to the chemical structures of the patina [53]. In this case, a non-invasive technique such as Raman spectroscopy has been transformed to all intents and purposes into an invasive technique, carrying out an invasive preparation of the sample to study the internal part of the artefact. Obviously, in the case of an artefact of broad historical and artistic interest, this could not be possible. The fact of being able to study in depth some artefacts which are of little archaeological value allows us to advance hypotheses regarding the corrosion phenomena of contemporary artefacts, perhaps of more archaeological importance.

In this case study, a series of iron nails from an archaeological site located in Sardinia were deeply analyzed to fully characterize the iron corrosion products. For this purpose, different Raman spectra were acquired at the same point of analysis to obtain the best measurement parameters subsequently used to characterize the samples. The archaeological site and the burial conditions are explained below.

4.1.1 The archaeological site

Tharros is an ancient city on the north-western coast of Sardinia island (Italy). Specifically, it is situated on the Sinis Peninsula, near the town of Cabras in the province of Oristano. Thanks to its strategic position overlooking the Mediterranean Sea it has always been an important centre for maritime trade and cultural exchange in the ancient Mediterranean, also thanks to the important mining resources [87]. Today, Tharros is a UNESCO World Heritage Site representing an important evidence of Sardinia's history.

The Phoenicians founded Tharros in the 8th century BC on a pre-existing nuragic settlement. Later, the city was dominated by the Carthaginians, becoming one of the largest Punic cities in the Mediterranean until the Roman conquest, around the 3rd century BC [88]. As a result, Tharros became an economically powerful city, in the middle of the trade route between Marseille and the Iberian Peninsula. As a result of these multicultural influences, the structure of the city results in being complex and

Fig. 4.1 Example of the encrusted and corroded iron nail from the archaeological site of Tharros (Sardinia, Italy)

strongly overlapped. Unfortunately, the story of the city ends in 1071 AD; in fact, Tharros was completely abandoned after a slow and progressive depopulation due to the Empire crisis and the numerous Saracens and Vandals incursions [88].

Following numerous clandestine incursions, the first systematic excavation started in the 50's. The general plan of the excavation area is presented in Figure. Over the years, the excavations have revealed the complex stratigraphy and have uncovered a wide variety of archaeological finds, including architectural remains, necropolises, pottery, inscriptions, sculptures, metallic finds, commonly used objects such as nails and coins, jewels, and funerary artefacts [89]. These discoveries provide valuable insights into the daily life, economy, religion, and social organization of the ancient inhabitants of Tharros, as well as their interactions with other civilizations. Many of these objects are now part of important museum collections, and their study and conservation are of fundamental historical importance.

Concerning the metallic artefacts taken into consideration, they all come from the Phoenician-Punic necropolises. Among all the excavated objects (i.e. jewels, amulets, coins, nails), some iron nails (Figure 4.1) were selected to carry out all the analyses. "They have been buried for a long time in an aggressive marine soil (rich in P, S, Cl) [90], which induced, in dependence of the electrochemical nobility of the metallic material, corrosion phenomena of different entity on the artefacts." [83]. Some fundamentals will be briefly exposed to fully understand the corrosion mechanisms of iron and consequently, the corrosion products which are the subject of this study will be presented.

4.1.2 Corrosion of buried iron artefacts

The archaeological iron artefacts buried in soil undergo a complex degradation process which is strictly influenced by different parameters linked to the surrounding environment: oxygen availability linked to the soil permeability, water quantity, temperature, soil composition (pH, chemical elements, texture), the presence of organic compounds, aggressive agents and microorganisms [91]. The corrosion products (mainly iron oxides and hydroxides) stratify in different layers characterized by different chemical stability. Depending on the burial conditions and the parameters described above, different mineralogical phases are subsequently formed: magnetite (Fe_3O_4), hematite (α-Fe_2O_3), maghemite (γ - Fe_2O_3), goethite (α -FeOOH), akaganèite (β-FeOOH) and lepidocrocite (γ-FeOOH) [92] [93]. All the factors mentioned above can induce the formation of one corrosion product rather than another. Once the corrosion process has started, the progression of degradation phenomena depends on the presence of stable or active phases. In fact, the iron artefact can reach an equilibrium or, on the contrary, can be irreversibly damaged even reaching the point of losing the initial metal core.

The corrosion starts from the surface and can continue to the innermost part of the artefact, creating a series of layers with different characteristics. It is possible to evidence a stratigraphy of the corrosion layers, describing the corrosion system. Below, a short description of the corrosion system is provided and subsequently, the sequence of the different layers is presented in Figure 4.2. Conventionally, accordingly with [94], the different corrosion zone (from outside to inside) are represented by:

- Soil (S): is represented by incrustations of the surrounding soil which is not always present;
- Transformed Medium (TM): this layer contains corrosion products slightly less mineralized and markers from the surrounding soil (i.e. quartz and mineral grains);
- Dense Product Layer (DPL): this layer is in strict contact with the metal core and it is constituted only by well-crystalized corrosion products;
- Metal core (M): if present, it has the composition and characteristics of the initial constituent metal.

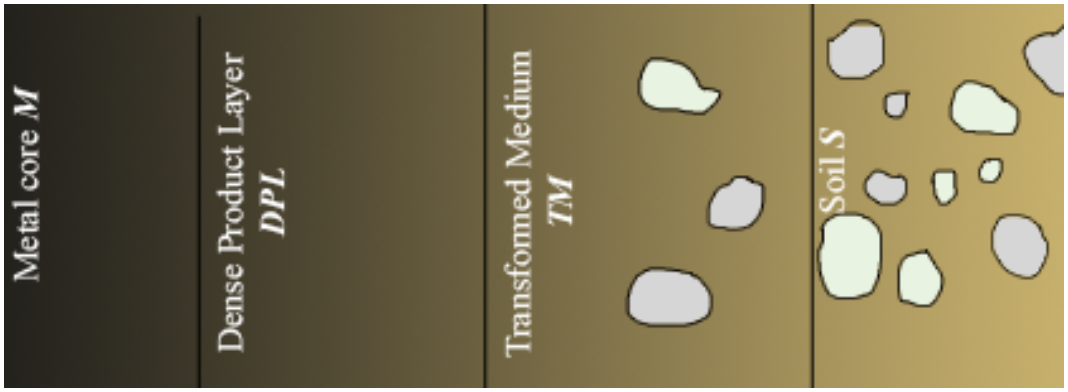

Fig. 4.2 Description of the corrosion layers from the metal core (M) to the incrustation of soil (S) on an archaeological iron artefact, according to *Neff et al.*

It is evident that the identification of the corrosion products can be used to establish the state of conservation of the artefact and, moreover, to understand the outline that led to the corrosion process. In particular, the presence of active phases (i.e. akaganéite) can be the trigger for further degradation actions if conditions change after extraction from the context in which the object has been in equilibrium for a long time. In this case, the development of a measurement protocol for the study of archaeological iron with Raman spectroscopy was developed and tested.

Soil composition of the archaeological site

As mentioned before, the characterization of the surrounding environment is fundamental to correlating the corrosion processes and the characteristics of the soil. The components of the soil of Tharros (with a sandy loam texture) are those typical of a coastal region (according to its geographical position), rich in carbonates, quartz, aggressive elements such as chlorine (from the marine waters), metallic ions (Ca, Fe, Mg, Pb) and a pH of 8.7 [91].

The mineralogical composition of the soil was analyzed by XRD, confirming the presence of different silicates, calcium and magnesium carbonates, quartz, K-feldspars, and calcium chloride. The obtained XRD spectra with the more significant peaks are presented in Figure 4.3. The acquisition of XRD spectra followed the same acquisition parameters described in 2.3.4. It is important to underline that the composition of the soil may have changed during the burial of the artefact, accelerating or decelerating the degradation. Therefore, it is possible to make

hypotheses only based on the analyses carried out on the current soil, which allows having an idea of the type of corrosion that occurred in the past.

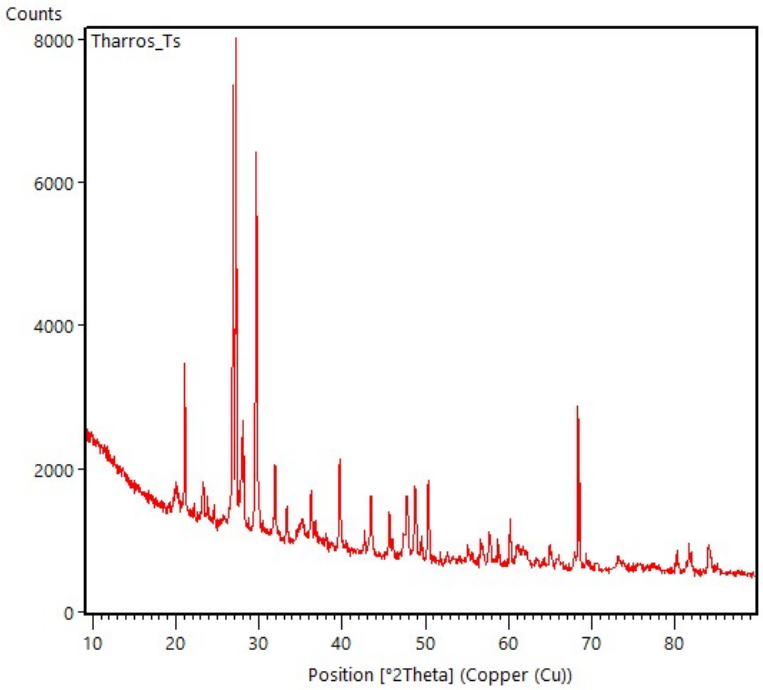

Fig. 4.3 XRD pattern of a Tharros soil sample

4.1.3 Raman spectroscopy

Below, the Raman spectroscopic analysis will be presented; it has returned fundamental data to understand both the state of conservation of the artefacts and, in addition, to suggest best practices for the good conservation of similar artefacts.

Sample preparation

To perform the Raman analyses, four different iron nails from the Phoenician-Punic necropolis were selected. As previously shown in Figure 4.1, they were completely corroded and covered by incrustation of soil. Below, the preparation protocol will be presented:

- Selection of the sample: among all the nails, were selected those that were intact at first glance and with sufficient dimensions;
- Sample cleaning: the selected samples were cleaned using micro-sandblasting to eliminate part of the soil incrustations;
- Resin embedding: the samples were embedded in epoxy-resin;
- Sample cutting: cross-sections have been obtained using a cutting machine with a diamond blade obtaining longitudinal sections;
- Sample documentation: high-resolution images of the nail section were acquired using an IDS UI-1460SE micro-camera.

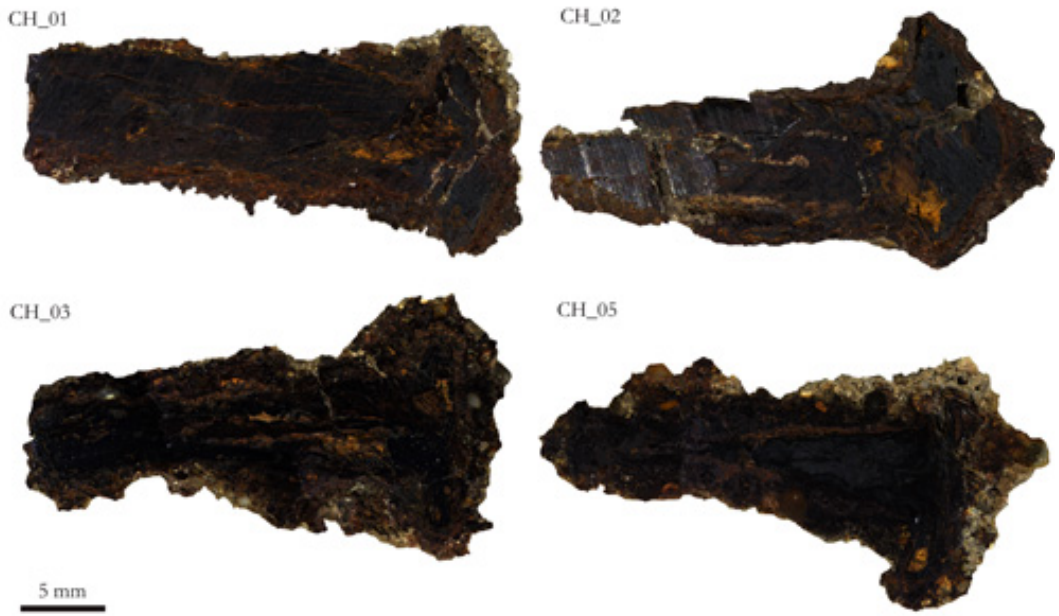

Fig. 4.4 Cross-sections of the selected iron nails after the longitudinal cut and embedded in resin (deleted from the image to better visualize the samples).

Measurement protocol

The Raman measurement areas were selected after the observation under a high-resolution micro camera, according to their different colour or morphology as evident in Figure 4.4.

The acquisition of Raman spectra was carried out by using a BWTEK Raman spectrometer connected to a cooled CCD detector; the 785 nm diode laser is focused on the sample through an Opteka microscope equipped with different objectives (20× magnification, 90 μm laser spot). The instrumental range of acquisition range was in the range of 150-3500 cm^{-1} with a spectral resolution of 5 cm^{-1}. The first parameter that needed to be adapted to the analysis was the laser power, according to literature [53] to avoid any damage to the chemical composition of the corrosion products, changing the obtained results. Concerning the spectra processing, compared with databases available in the literature [55] [86] [84]. The characteristic Raman peaks (expressed in cm^{-1}) used for the identification of each corrosion product are listed in Table 4.1.

hematite	goethite	magnetite	maghemite	lepidocrocite	akaganéite
223,289, 404,496, 607,817, 1310	244,300, 390,685, 980,1100, 1300	538,670	350,512, 670,720	250,380, 528,650, 1298	310,390, 538,720

Table 4.1 Iron corrosion products and their characteristic peaks (cm^{-1}) in Raman spectrum.

The laser power was set to a range of 15-30 mW while the integration time was between 10 s and 20 s, with 5 repetitions. The set parameters avoided the problems of product transformations (i.e. maghemite → hematite, goethite → hematite, lepidocrocite → maghemite, hematite → magnetite [53]). To uniform the measurement protocol were selected the following parameters: 15 mW laser power, 12 s integration time and 5 repetitions.

	Laser power (mW)	Integration time (s)	Repetitions (time)
hematite	20	15	5
goethite	20	10	5
magnetite	15	15	5
maghemite	15	10	5

Table 4.2 Parameters set for the acquisition of Raman spectra of iron corrosion products.

The measurements started from the heart of the artefact and subsequently moved towards the outside to get an overall view of the composition and the conservation state of the iron nails.

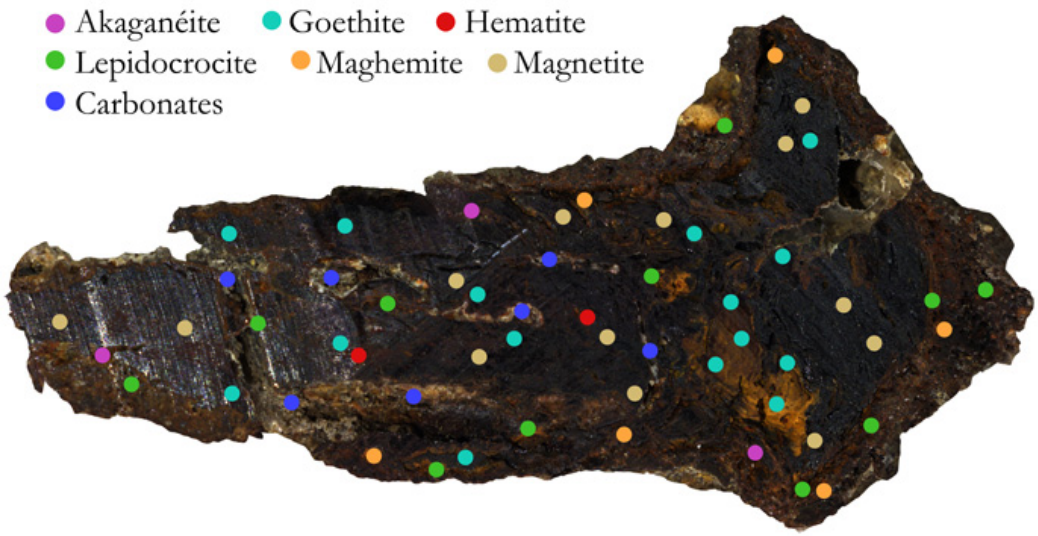

Fig. 4.5 Raman measurements on CH-02 sample.

Results and discussion

The analyzed samples appear almost completely mineralised. The initial metallic heart is no longer present, completely replaced by corrosion products. This is attributable to the long burial period, which allowed the iron oxides and hydroxides to be mineralised. This allowed good discrimination of the mineralogical phases, which is more difficult in the transition zone where the phases are less crystallized. The samples were quite homogeneous, presenting approximately the same phases. The set parameters resulted to be quite effective, avoiding any changes in the chemical structure of the sample. For convenience, the measurement points and Raman results on a single nail (CH-02) are reported in Figure 4.5.

The most present product is magnetite (Fe_3O_4), more compact and present in the innermost part of the nail, and porous goethite (α -FeOOH). In some areas, moving towards the surface, the presence of complex magnetite-goethite mixtures was identified. It is important to underline that magnetite has a weak characteristic peak around 670 cm^{-1} which can be overlapped by one of the characteristic peaks of goetithe at 685 cm^{-1} and sometimes prevent correct identification [85]. In this specific case, given the enormous quantity of magnetite the distinction has always been successful.

In the magnetite-goethite matrix, there are some areas in which the presence of hematite (α-Fe_2O_3) is also highlighted. Lepidocrocite (γ-FeOOH), however, has

been identified in the transition zone, where some less crystallized corrosion products are found together with markers from the soil, such as quartz crystals.

Some whitish areas have been identified in correspondence with some fractures within the structure of the nails. These are probably mixed carbonates precipitated inside the cracks. However, the Raman analysis does not allow to discriminate between calcite ($CaCO_3$) and siderite ($FeCO_3$), which both have a characteristic peak between 1084 cm^{-1} and 1088 cm^{-1}. The presence of calcite in the soil was therefore confirmed by XRD analysis presented before in 4.3.

In the external part of the samples, almost at the boundary between the transformed medium and the incrustation of soil, the presence of akaganèite, an active phase containing chlorine, which has been identified together with goethite, can be correlated to the composition of the soil; the fact that it is found in a complex mixture made the identification more difficult. Briefly, the results obtained for each sample will be resumed below. Some exemplicative spectra of the corrosion products found on the samples are presented in Figure 4.6.

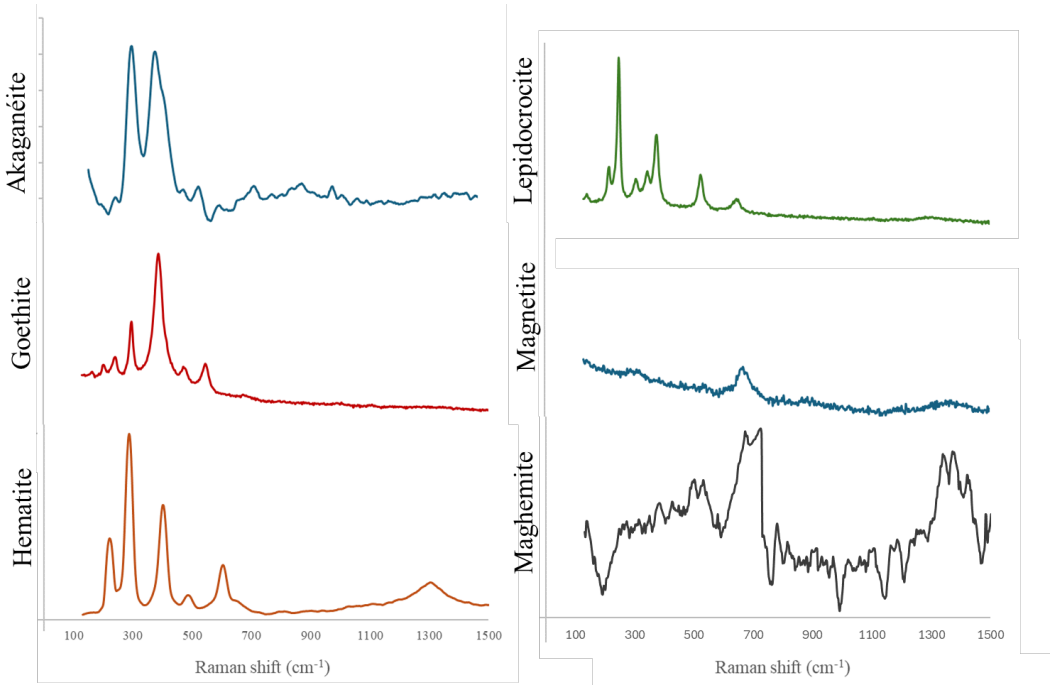

Fig. 4.6 Raman spectra of the iron oxides and hydroxides obtained on the iron nails

4.1.4 Conclusions

The assessment of the conservation state of iron nails and the study of corrosion processes through Raman spectroscopy gave back good results avoiding any changes in the morphology of corrosion. Raman spectroscopy proves to be a versatile analytical technique regarding the study of corrosion products, allowing rapid analysis and easy application even to numerous samples. This technique could be also used eventually for *in situ* analysis directly on the excavation helping to correctly preserve the artefacts immediately after extraction.

In this case study, the technique was used in an invasive way to analyse the internal part of the iron nails. As presented before, the analyzed samples appear almost completely mineralized. The initial metal core (i.e. iron) is replaced by well-mineralised corrosion products. This is attributable to the long burial period, which allowed the complete mineralization of the iron oxides and hydroxides. This allows good discrimination of the mineralogical phases, which is more difficult in the transition zone where the phases are less crystallized.

The study will be used for the indirect study of other iron artefacts (nails, axes, etc.) from the Tharros excavation that can not be sectioned. However, these results can provide preliminary information to archaeologists and conservators about the conservation state and the hypothetical conservation of the artefacts to avoid further modifications to the nature of the artefacts. The main suggestion is about a conservation strategy which predicts a controlled atmosphere (i.e. under nitrogen).

4.2 Development of a protocol for the evaluation of long-term protective effectiveness of protective treatments

The evaluation of a protective method is usually carried out through artificial ageing and subsequent analysis using analytical methodologies that require long analysis times and are sometimes difficult to interpret [95]. In this scenario, a dedicated protocol for the evaluation of the effectiveness of treatments using an unusual technique for the purpose was tested. The protocol was made to test the reliability of treatments after years, in a fast and non-invasive way. A previous study was carried

Fig. 4.7 Iron nails used to test the long-term protective effectiveness.

out on the same samples, shortly after the treatment providing good results for some protectives [96].

The evaluation of the protective effectiveness of a set of iron nails from unknown Piedmontese excavation sites of Roman and Medieval Age (Figure 4.7) submitted twenty-six years ago to different treatments [96] (in situ polymerization of acrylate coatings, primers application, rust converters treatment, rust dissolving solutions treatments) was made by using Raman spectroscopy.

The obtained results with Raman spectroscopy were compared to the old results. In fact, in this case study, Raman spectroscopy was used for the surface analysis of the objects examined in order to evaluate the presence of more or less stable corrosion phases. Briefly, an introduction to treatments for the conservation of metallic artefacts will be presented.

4.2.1 Protective treatments and effectiveness testing

One of the challenges linked to the conservation of metal artefacts is related to their protection. After an object is removed from a specific environment (i.e. the soil of an archaeological site, the seawater for submerged artefacts, the storage box of a Museum warehouse, and so on) is crucial to plan corrosion protection so that they do not alter over time and that they can be preserved and exposed.

The materials and coatings employed for corrosion protection of Cultural Heritage metallic artefacts are numerous [23] [97] but they have to fulfil specific requirements:

- last for a long time without the need of further maintenance;
- be easily removable to allow future tests and possible protective re-treatments
- do not induce change in the appearance
- be harmless for the conservators and the environment

Usually accelerated corrosion tests are carried out in laboratory to evaluate the performances of the different protective treatments applied to reference samples with similar characteristics to artefacts or, rarely, to real artefacts [98]. Briefly, the treatments applied and the first characterization of the effectiveness will be presented.

Different protective treatments were selected for the study, in particular some commercial solutions and an experimental one. Before the applications, the corrosion products were characterized using X-ray diffraction. Some samples were subjected to a chlorinating procedure to evaluate the influence of chlorine in the protective evaluation. The pre-treatments and treatments tested are listed in Table 4.3.

Pre-treatments	Protectives	Application	Class
	Ferox	Brush	Rust converter
H_20	Rust Oleum	Brush	Primer
or	Remox	Brush	Rust dissolving solution
HCl (10wt%)	Metallay	Immersion	Rust dissolving solution
	Acrylates	Immersion	Polymerization

Table 4.3 Pre-treatments and protective treatments applied on the archaeological iron nails to test the short-term effectiveness of the protectives.

After the application, the samples were split into different short-time tests to test their effectiveness. The samples were weighted before and after the exposure to climatic chamber and constant humidity chamber to evaluate the protection effectiveness in terms of weight loss or addition; some samples were analysed by Electrochemical Impedeance Spectroscopy (EIS) [96]. The obtained results are simplified in Table 4.4.

Test	Best results
Climatic chamber	Acrylates, Rust Oleum, Ferox
Constant humidity chamber	Acrylates
EIS measurement	Acrylates, Rust Oleum, Ferox

Table 4.4 Summary of the results obtained in the past after the application of some protective treatments.

Since the evaluation was carried out on potential Cultural Heritage objects, another evaluation was carried out in addition to the evaluation of the protective efficacy. The colour maintenance understood as any modification in the surface. At this evaluation, only the samples treated with *acrylates* passed the test. On the basis of these evaluations carried out in a short timeusing accelerated ageing procedures, a protective efficacy scale was highlighted with the best behaviour shown by the *acrylate* coatings.

4.2.2 Evaluation of long-term protective effectiveness by Raman spectroscopy

After the application of different protective treatments, the nails were stored at room temperature till nowadays and were examined again in order to evidence the effect of a real long-term exposure to the atmosphere. At a visual observation, the nails appear in good condition, although some had already shown a colour change at the time, except the ones covered with the *acrylates* coatings that have been subjected during the years to extensive flaking (Figure 4.8). The surfaces of the nails untreated and treated with the different materials were analyzed utilizing Raman Spectroscopy.

Fig. 4.8 Sample CH-15 treated with acrylates and then exposed to constant humidity chamber.

Raman spectra acquisition

In this case, the Raman analyses followed the measurement protocol presented in 4.1.3. The set parameters were the following: laser power 10 mW, 10 s integration time, and 5 repetitions. The laser was further lowered due to the high fluorescence on the surface caused by the protective treatments. The spectra processing followed the protocol previously presented in 4.1.3.

Unlike the previous case study, the characterization was made only on the surface of the nails, avoiding any sectioning of the samples. As an example, the spectra of the different iron corrosion products found on an untreated sample are presented in Figure 4.9.

A resume of all the obtained results is presented in Table 4.5.

Treatment	Main corrosion products
No treatment	goethite, lepidocrocite, hematite, akaganéite
Ferox	goethite, lepidocrocite
Rust Oleum	hematite
Remox	goethite
Metallay	goethite
Acrylates	hematite, akaganéite, lepidocrocite, goethite

Table 4.5 Main corrosion products found on the surface of iron nails (treated with protective and untreated).

4.2.3 Conclusions

The long-term action of oxygen and humidity has led to the formation of different iron oxide phases, mainly goethite on the nails treated with rust-dissolving solutions,

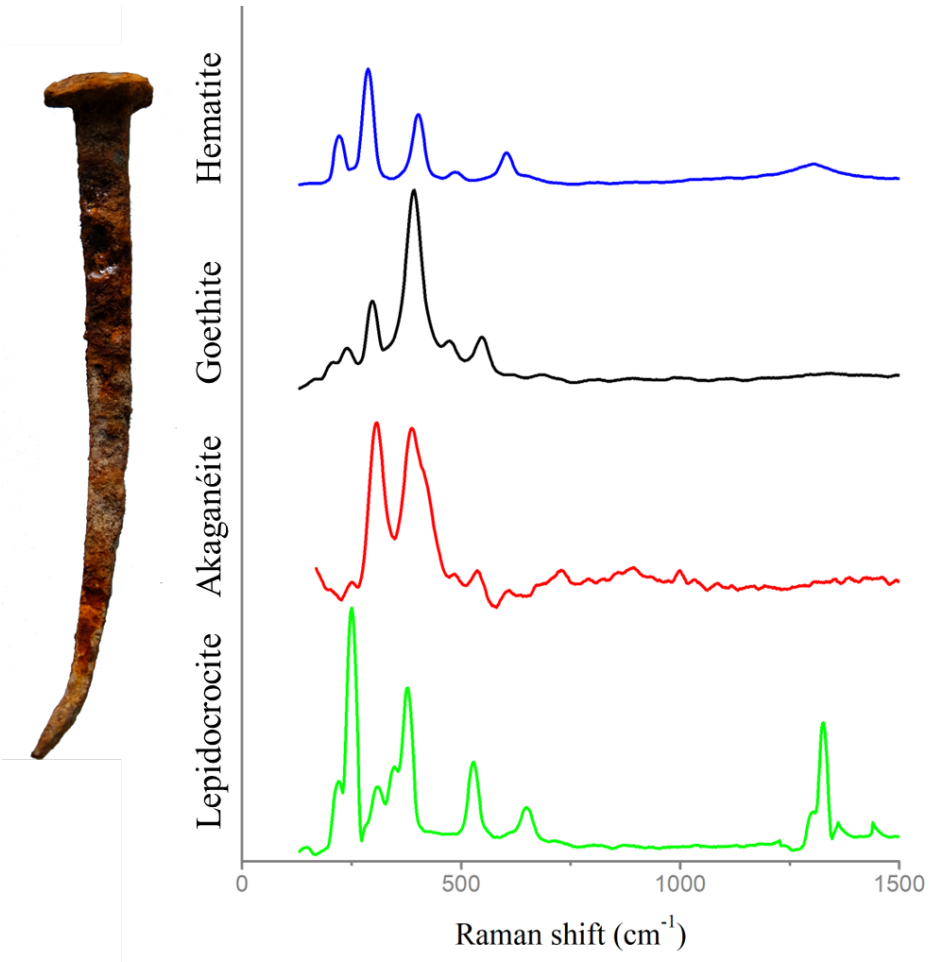

Fig. 4.9 Raman spectra of iron corrosion products found on untreated sample CH-19.

hematite on nails treated with the primer and, among the others, lepidocrocite and akagenéite too on the nails untreated or coated with acrylates.

From these results it is possible to evidence that the protective treatment which showed better protective power immediately after application and efficacy testing (*acrylates*), now appears to have completely lost its effectiveness, leading to the flaking of the surface. The presence of active phases (i.e. akagenéite) is a sign that the corrosion is still active and that it can lead to the complete failure of the sample.

Concerning the other applications, the two which showed good results in the past (leaving aside the colour changes) and confirmed their protective power are *Rust Oleum* and *Ferox*. In fact, the corrosion products are stable and tend to be the result of the chemical transformation that occurs during application. This implies a high stability of the system, avoiding any flaking.

From these preliminary experimental results, it is evident that Raman spectroscopy can be used to check the surface composition of samples in order to assess the corrosion state of the sample.

Chapter 5

Conclusions

At the end of this research work, it is important to summarize all the addressed issues and attempt to resolve any limitations. In the previous Chapters of the PhD thesis, the potential of different diagnostic techniques applied in the study and characterization of metallic artefacts was explored.

The obtained results reveal that the two imaging techniques considered could be easily applied in studying metallic artefacts, despite their limitations.

In particular, while Neutron Imaging provides a complete overview of the composition and structure of metal alloys, further research is needed to better discriminate the small differences in the chemical composition by improving the acquisition of neutron images to a broader number of reference alloys. Additionally, more accurate acquisition of radiographs could provide deeper insights into the chemical and structural identification. Moreover, understanding the factors which influence the calculation of mass attenuation coefficient is crucial for an effective decrease in the associated uncertainty.

As shown in Table 5.1, the main limitations are linked to the difficulty of performing the analysis (high cost, limited availability, limited analysis time, and so on). Concerning the main limitations that emerged during this research work, the main problem lies in the high value of uncertainty associated to the mass attenuation coefficient. The limited acquisition could affect these results and, moreover, the high number of variables must be reviewed. Despite that, it is clear how this technique can provide useful information not otherwise identifiable unless using a greater number of techniques, perhaps even invasive.

Absorption Contrast Neutron Imaging

Pros	Cons
Non-invasive and non-destructive	Expensive technique
High penetration of neutrons	Long time of analysis
High-sensitivity to light elements	Need of a neutron source
Complementary information	limited time of analysis
cross-section, not Z-dependent	Strict radioprotection law

Table 5.1 Pros and cons of the use of Neutron Imaging for the study of Cultural Heritage artefacts.

Reflectance Transformation Imaging

Pros	Cons
Non-invasive and non-destructive	Limited sample size
Low-cost and portable	Need to acquire a database
Automatic acquisition	Importance of focal distance
Surface analysis	
Usable with any smartphone	

Table 5.2 Pros and cons of the use of the developed RTI system for the study of Cultural Heritage artefacts.

It is easy to understand that the limitation related to the radioprotection is not instrument-dependent, so it may limit the application on archaeological artefacts as long as they are treated as radioactive materials. This is the reason why, until now, no historical artefacts have been analysed yet at the LENA centre. Maybe in the near future it will be possible to finally apply the technique on real artefacts to evaluate the real feasibly of the tested method.

The developed RTI system proved to be a low-cost and portable instrumentation, very useful for the characterization of the superficial morphology of artefacts. As it is possible to see in Table 5.2, the system presents several advantages in the study of archaeological artefacts. The main limitation, that could be overcome by developing a bigger dome, is linked to the possibility of analyzing only small objects. This is the main issue that needs to be fixed, given the wide variety of objects in the Cultural Heritage field.

In conclusion, the tested imaging techniques provide useful tools for the characterization and assessment of the conservation state of metallic artefacts. Future research should focus eventually on resolving these limitations, to be able to apply the methodology to the study of archaeological metallic artefacts.

References

[1] Marco Cardinali, Maria Beatrice De Ruggieri, and Claudio Falcucci. *Diagnostica artistica: tracce materiali per la storia dell'arte e per la conservazione*. 2002.

[2] Giovanni Leucci. *Nondestructive testing for archaeology and cultural heritage: A practical guide and new perspectives*. Springer, 2018.

[3] R Fontana and P De Natale. Enriching the metrological toolbox for applications to cultural heritage. *Metrology and Physical Constants*, 185:125, 2013.

[4] C Lahanier, G Amsel, C Heitz, M Menu, and HH Andersen. Editorial of proceedings of the international workshop on ion-beam analysis in the arts and archaeology. *Nuclear Instruments and Methods in Physics Research, B*, 14(1), 1986.

[5] Gilberto Artioli. *Scientific methods and cultural heritage: an introduction to the application of materials science to archaeometry and conservation science*. OUP Oxford, 2010.

[6] Luca Piroddi, Nasser Abu Zeid, Sergio Vincenzo Calcina, Patrizia Capizzi, Luigi Capozzoli, Ilaria Catapano, Marilena Cozzolino, Sebastiano D'Amico, Rosa Lasaponara, and Deodato Tapete. Imaging cultural heritage at different scales: Part i, the micro-scale (manufacts). *Remote Sensing*, 15(10):2586, 2023.

[7] P Triolo, L Marras, G Adinolfi, R Carmagnola, S Legnaioli, S Raneri, and V Palleschi. Imaging for cultural heritage and archaeology. In *2020 IMEKO TC-4 International Conference on Metrology for Archaeology and Cultural Heritage*, pages 512–516, 2020.

[8] Emma Marie Payne. Imaging techniques in conservation. *Journal of conservation and museum studies*, 10(2):17–29, 2012.

[9] Adam P Gibson. Medical imaging applied to heritage. *The British Journal of Radiology*, 96(1152):20230611, 2023.

[10] Alessandro Re, Fauzia Albertin, Chiara Avataneo, Rosa Brancaccio, Jacopo Corsi, Giorgio Cotto, Stefania De Blasi, Giovanni Dughera, Elisabetta Durisi, Walter Ferrarese, et al. X-ray tomography of large wooden artworks: the case study of" doppio corpo" by pietro piffetti. *Heritage Science*, 2:1–9, 2014.

[11] Franz Mairinger. Uv-, ir-and x-ray imaging. In *Comprehensive analytical chemistry*, volume 42, pages 15–71. Elsevier, 2004.

[12] JRJ Van Asperen de Boer. Reflectography of paintings using an infrared vidicon television system. *Studies in Conservation*, 14(3):96–118, 1969.

[13] D Gavrilov, R Gr Maev, and DP Almond. A review of imaging methods in analysis of works of art: Thermographic imaging method in art analysis. *Canadian Journal of Physics*, 92(4):341–364, 2014.

[14] Leila Es Sebar, Luca Lombardo, Marco Parvis, Emma Angelini, Alessandro Re, Sabrina Grassini, Alessandro Bovero, and Alessandro Lo Giudice. Metrological validation of a photogrammetry-based technique. In *2022 IEEE International Instrumentation and Measurement Technology Conference (I2MTC)*, pages 1–6. IEEE, 2022.

[15] Leila Es Sebar, Luca Lombardo, Paola Buscaglia, Tiziana Cavaleri, Alessandro Lo Giudice, Alessandro Re, Matilde Borla, Sara Aicardi, and Sabrina Grassini. 3d multispectral imaging for cultural heritage preservation: the case study of a wooden sculpture of the museo egizio di torino. *Heritage*, 6(3):2783–2795, 2023.

[16] Surface Optics. Hyperspectral imaging for art conservation., 2023. Accessed on 2023-11-08.

[17] Kaori Fukunaga, Emilia Cortes, Antonino Cosentino, Isabel Stuenkel, Marco Leona, Irl N Duling III, and David T Mininberg. Investigating the use of terahertz pulsed time domain reflection imaging for the study of fabric layers of an egyptian mummy. *Journal of the European Optical Society-Rapid Publications*, 6, 2011.

[18] Claudio Giardino et al. *I metalli nel mondo antico. Introduzione all'archeometallurgia*. Editori Laterza, 2010.

[19] Ronald F Tylecote. A history of metallurgy. *British Corrosion Journal*, 12(3):137–140, 1977.

[20] A Mark Pollard and Peter Bray. Chemical and isotopic studies of ancient metals. *Archaeometallurgy in global perspective: Methods and syntheses*, pages 217–238, 2014.

[21] Régis Bertholon. Archaeological metal artefacts and conservation issues: long-term corrosion studies. In *Corrosion of metallic heritage artefacts*, pages 31–40. Elsevier, 2007.

[22] Sara Goidanich, Luciano Lazzari, and Marco Ormellese. Ac corrosion. part 2: Parameters influencing corrosion rate. *Corrosion Science*, 52(3):916–922, 2010.

[23] GW Walter. A critical review of the protection of metals by paints. *Corrosion Science*, 26(1):27–38, 1986.

[24] Arthur Cohen. Corrosion of copper and copper alloys. 2005.

[25] I Constantinides, A Adriaens, and F Adams. Surface characterization of artificial corrosion layers on copper alloy reference materials. *Applied surface science*, 189(1-2):90–101, 2002.

[26] Luc Robbiola, J-M Blengino, and Corros Fiaud. Morphology and mechanisms of formation of natural patinas on archaeological cu–sn alloys. *Corrosion Science*, 40(12):2083–2111, 1998.

[27] SD Rasberry and TE Gills. The certification, development and use of standard reference materials. *Spectrochimica Acta Part B: Atomic Spectroscopy*, 46(12):1577–1582, 1991.

[28] Amina Vietti, Luisa Vigorelli, Sabrina Grassini, Laura Guidorzi, Marta Magalini, Alessandro Re, Alessandro Lo Giudice, Francesco Grazzi, and Nicla Gelli. Realisation and characterisation of cu-based references for neutron imaging calibration purposes and first results. *Acta IMEKO*, 12(4):1–6, 2023.

[29] JC Domanus et al. *Practical neutron radiography*, volume 16. Springer, 1992.

[30] Anna Fedrigo, Markus Strobl, Alan R Williams, Kim Lefmann, Poul Erik Lindelof, Lars Jørgensen, Peter Pentz, Dominik Bausenwein, Burkard Schillinger, Anton Kovyakh, et al. Neutron imaging study of 'pattern-welded' swords from the viking age. *Archaeological and Anthropological Sciences*, 10(6):1249–1263, 2018.

[31] L Jacobson, FC De Beer, and R Nshimirimana. Tomography imaging of south african archaeological and heritage stone and pottery objects. *Nuclear Instruments and Methods in Physics Research Section A: Accelerators, Spectrometers, Detectors and Associated Equipment*, 651(1):240–243, 2011.

[32] David Mannes, Walter Sonderegger, Stefan Hering, Eberhard Lehmann, and Peter Niemz. Non-destructive determination and quantification of diffusion processes in wood by means of neutron imaging. 2009.

[33] James Chadwick. The existence of a neutron. *Proceedings of the Royal Society of London. Series A, Containing Papers of a Mathematical and Physical Character*, 136(830):692–708, 1932.

[34] Nikolay Kardjilov and Giulia Festa. *Neutron methods for archaeology and cultural heritage*. Springer, 2017.

[35] Ian S Anderson, Robert L McGreevy, and Hassina Z Bilheux. *Neutron imaging and applications*. Number 2209. Springer, 2009.

[36] M Strobl, I Manke, N Kardjilov, A Hilger, M Dawson, and J Banhart. Advances in neutron radiography and tomography. *Journal of Physics D: Applied Physics*, 42(24):243001, 2009.

[37] Eberhard H Lehmann, David Mannes, Michael Henss, and Markus Speidel. Ancient buddhist metal statues using neutron tomography. In *Handbook of Cultural Heritage Analysis*, pages 273–303. Springer, 2022.

[38] Lorenzo Giuntini, Lisa Castelli, Mirko Massi, Mariaelena Fedi, Caroline Czelusniak, Nicla Gelli, Lucia Liccioli, Francesca Giambi, Chiara Ruberto, Anna Mazzinghi, et al. Detectors and cultural heritage: The infn-chnet experience. *Applied Sciences*, 11(8):3462, 2021.

[39] M Prata, D Alloni, P De Felice, M Palomba, A Pietropaolo, M Pillon, L Quintieri, A Santagata, and P Valente. Italian neutron sources. *The European Physical Journal Plus*, 129:1–15, 2014.

[40] A Salvini, D Alloni, S Altieri, N Protti, and M Clemenza. Design, implementation and future utilization of the pgnaa facility at the university of pavia–lena laboratory. In *Research Reactors: Addressing Challenges and Opportunities to Ensure Effectiveness and Sustainability. Summary of an International Conference. Supplementary Files*, 2020.

[41] Daniele Alloni, Giovanni Magrotti, Massimo Oddone, Michele Prata, Andrea Salvini, et al. Nuclear education & training activity experience at the university of pavia. In *16th IGORR 2014/IAEA Technical Meeting*, pages 1–8, 2014.

[42] Daniele Alloni, Giovanni Magrotti, Massimo Oddone, Michele Prata, Salvinii Andrea, et al. Lena-laboratory of applied nuclear energy (university of pavia)-neutron facilities & main activities. In *Book of Abstracts*, pages 44–44. ITA, 2015.

[43] N Gelli, L Giuntini, F Cantini, O Sans-Planell, M Magalini, M Manetti, L Sodi, M Massi, L Castelli, C Czelusniak, et al. The new infn-chnet neutron imaging facility. *Nuclear Instruments and Methods in Physics Research Section A: Accelerators, Spectrometers, Detectors and Associated Equipment*, 1051:168189, 2023.

[44] F Grazzi, F Cantini, O Sans-Planell, M Magalini, L Vigorelli, G Marcucci, M Clemenza, M Morigi, A Re, D Alloni, et al. A work-horse neutron imaging station at the laboratorio energia nucleare applicata (lena) in pavia (italy): Instrumental components and applications in the frame of the chnet-niche infn experiment. In *Journal of Physics: Conference Series*, volume 2605, page 012006. IOP Publishing, 2023.

[45] Paul T Craddock. The composition of the copper alloys used by the greek, etruscan and roman civilizations: 3. the origins and early use of brass. *Journal of Archaeological Science*, 5(1):1–16, 1978.

[46] David A Scott. *Metallography and microstructure in ancient and historic metals*. Getty publications, 1992.

[47] H Gleiter. The segregation of copper at high angle grain boundaries in lead. *Acta Metallurgica*, 18(1):117–121, 1970.

[48] Astm-e407-07 - standard practice for microetching metals and alloys. ASTM International: West Conshohocken, PA, USA.

[49] Copper.org. Copper development association inc., 2022. Accessed on 2022-09-21.

[50] David A Scott. Metallography and microstructure of ancient and historic metals, the getty conservation institute, the j. *Paul Getty Museum*, 1991.

[51] G Di Carlo, C Giuliani, C Riccucci, M Pascucci, E Messina, G Fierro, M Lavorgna, and GM Ingo. Artificial patina formation onto copper-based alloys: Chloride and sulphate induced corrosion processes. *Applied Surface Science*, 421:120–127, 2017.

[52] Katarina Marušić, Helena Otmačić-Ćurković, Šefka Horvat-Kurbegović, Hisasi Takenouti, and Ema Stupnišek-Lisac. Comparative studies of chemical and electrochemical preparation of artificial bronze patinas and their protection by corrosion inhibitor. *Electrochimica Acta*, 54(27):7106–7113, 2009.

[53] Monika Hanesch. Raman spectroscopy of iron oxides and (oxy) hydroxides at low laser power and possible applications in environmental magnetic studies. *Geophysical Journal International*, 177(3):941–948, 2009.

[54] Paul HC Eilers and Hans FM Boelens. Baseline correction with asymmetric least squares smoothing. *Leiden University Medical Centre Report*, 1(1):5, 2005.

[55] Barbara Lafuente, Robert T Downs, Hexiong Yang, and Nate Stone. 1. the power of databases: The rruff project. In *Highlights in mineralogical crystallography*, pages 1–30. De Gruyter (O), 2015.

[56] Valerie Hayez, Joseph Guillaume, Annick Hubin, and Herman Terryn. Micro-raman spectroscopy for the study of corrosion products on copper alloys: setting up of a reference database and studying works of art. *Journal of Raman spectroscopy*, 35(8-9):732–738, 2004.

[57] Francesca Ospitali, Cristina Chiavari, Carla Martini, Elena Bernardi, Fabrizio Passarini, and Luc Robbiola. The characterization of sn-based corrosion products in ancient bronzes: a raman approach. *Journal of Raman Spectroscopy*, 43(11):1596–1603, 2012.

[58] T Laetsch and R Downs. Software for identification and refinement of cell parameters from powder diffraction data of minerals using the rruff project and american mineralogist crystal structure databases. In *19th General Meeting of the International Mineralogical Association, Kobe, Japan*, volume 23, page e28, 2006.

[59] Amina Vietti, Marco Parvis, Nicola Donato, Sabrina Grassini, and Luca Lombardo. Development of a low-cost and portable device for reflectance transformation imaging. In *2023 IEEE International Instrumentation and Measurement Technology Conference (I2MTC)*, pages 1–6. IEEE, 2023.

[60] Thomas Malzbender, Dan Gelb, Hans Wolters, and Bruce Zuckerman. Enhancement of shape perception by surface reflectance transformation. In *VMV*, page 183, 2004.

[61] David Selmo, Fraser Sturt, James Miles, Philip Basford, Tom Malzbender, Kirk Martinez, Charlie Thompson, Graeme Earl, and George Bevan. Underwater reflectance transformation imaging: a technology for in situ underwater cultural heritage object-level recording. *Journal of Electronic Imaging*, 26(1):011029–011029, 2017.

[62] Tom Malzbender, Dan Gelb, and Hans Wolters. Polynomial texture maps. In *Proceedings of the 28th annual conference on Computer graphics and interactive techniques*, pages 519–528, 2001.

[63] Hendrik Hameeuw, Geert Willems, Frank Verbiest, Wim Moreau, Karel Van Lerberghe, and Luc Van Gool. Easy and cost-effective cuneiform digitizing. In *The 6th International Symposium on Virtual Reality, Archaeology and Cultural Heritage (VAST 2005)*, pages 73–80. Eurographics Association, 2005.

[64] Øyvind Hammer, Stefan Bengtson, Tom Malzbender, and Dan Gelb. Imaging fossils using reflectance transformation and interactive manipulation of virtual light sources. *Palaeontologia Electronica*, 5(1):1–9, 2002.

[65] Sarah E Newman. Applications of reflectance transformation imaging (rti) to the study of bone surface modifications. *Journal of Archaeological Science*, 53:536–549, 2015.

[66] Gianpaolo Palma, M Baldassarri, M Favilla, and R Scopigno. Storytelling of a coin collection by means of rti images: the case of the simoneschi collection in palazzo blu. In *Museums and the Web*, volume 2, pages 15–16, 2014.

[67] Eleni Kotoula. Application of rti in museum conservation. In *Archaeology in the Digital Era. Papers from the 40th Annual Conference of Computer Applications and Quantitative Methods in Archaeology (CAA). Amsterdam University Press, Amsterdam*, pages 232–240, 2012.

[68] Marta Díaz-Guardamino, Leonardo García Sanjuán, David Wheatley, and Víctor Rodríguez Zamora. Rti and the study of engraved rock art: A re-examination of the iberian south-western stelae of setefilla and almadén de la plata 2 (seville, spain). *Digital Applications in Archaeology and Cultural Heritage*, 2(2-3):41–54, 2015.

[69] Jacqueline F DiBiasie Sammons. Application of reflectance transformation imaging (rti) to the study of ancient graffiti from herculaneum, italy. *Journal of Archaeological Science: Reports*, 17:184–194, 2018.

[70] James Miles, Mike Pitts, Hembo Pagi, and Graeme Earl. New applications of photogrammetry and reflectance transformation imaging to an easter island statue. *Antiquity*, 88(340):596–605, 2014.

[71] Amalia Siatou, Marvin Nurit, Yuly Castro, Gaëtan Le Goïc, Laura Brambilla, Christian Degrigny, and Alamin Mansouri. New methodological approaches in reflectance transformation imaging applications for conservation documentation of cultural heritage metal objects. *Journal of Cultural Heritage*, 58:274–283, 2022.

[72] Yariv Goldman, Ravit Linn, Orit Shamir, and Mina Weinstein-Evron. Micro-rti as a novel technology for the investigation and documentation of archaeological textiles. *Journal of Archaeological Science: Reports*, 19:1–10, 2018.

[73] Mark Mudge, Tom Malzbender, Carla Schroer, and Marlin Lum. New reflection transformation imaging methods for rock art and multiple-viewpoint display. In *Ioannides, M.; Arnold, D.; Niccolucci, F. & Mania, K., eds., The 7th International Symposium on Virtual Reality, Archaeology and Cultural Heritage*, volume 6, pages 195–202.

[74] JF Murray-Coleman and AM Smith. The automated measurement of brdfs and their application to luminaire modeling. *Journal of the Illuminating Engineering Society*, 19(1):87–99, 1990.

[75] Stephen H Westin, James R Arvo, and Kenneth E Torrance. Predicting reflectance functions from complex surfaces. In *Proceedings of the 19th annual conference on Computer graphics and interactive techniques*, pages 255–264, 1992.

[76] Eric PF Lafortune, Sing-Choong Foo, Kenneth E Torrance, and Donald P Greenberg. Non-linear approximation of reflectance functions. In *Proceedings of the 24th annual conference on Computer graphics and interactive techniques*, pages 117–126, 1997.

[77] Pascal Gautron, Jaroslav Krivánek, Sumanta N Pattanaik, and Kadi Bouatouch. A novel hemispherical basis for accurate and efficient rendering. *Rendering Techniques*, 2004:321–330, 2004.

[78] Fred Edwin Nicodemus, J C Richmond, and H H Hsia. *Geometrical considerations and nomenclature for reflectance*, volume 160. National Bureau of Standards, 1977.

[79] PJRC. Teensy 3.2 development board, 2022. Accessed on 2022-12-08.

[80] AM Pollard and Ruiliang Liu. Bronze alloying practice in ancient china-evidence from pre-qin coin analyses. *Journal of archaeological science*, 126:105322, 2021.

[81] Ling He, Junyan Liang, Xiang Zhao, and Baolian Jiang. Corrosion behavior and morphological features of archeological bronze coins from ancient china. *Microchemical Journal*, 99(2):203–212, 2011.

[82] Amina Vietti, Nicola Donato, Emma Angelini, Sabrina Grassini, et al. Caratterizzazione di manufatti in ferro di epoca fenicio-punica mediante spettroscopia raman. *La Metallurgia Italiana*, page 8, 2021.

[83] A Vietti, E Angelini, S Grassini, and N Donato. Raman spectroscopic characterization of corrosion products of archaeological iron. In *Journal of Physics: Conference Series*, volume 2204, page 012066. IOP publishing, 2022.

[84] Ludovic Bellot-Gurlet, Delphine Neff, Solenn Réguer, Judith Monnier, Mandana Saheb, and Philippe Dillmann. Raman studies of corrosion layers formed on archaeological irons in various media. *Journal of Nano Research*, 8:147–156, 2009.

[85] Delphine Neff, Solenn Reguer, Ludovic Bellot-Gurlet, Philippe Dillmann, and Régis Bertholon. Structural characterization of corrosion products on archaeological iron: an integrated analytical approach to establish corrosion forms. *Journal of Raman Spectroscopy*, 35(8-9):739–745, 2004.

[86] Richard J Thibeau, Chris W Brown, and Robert H Heidersbach. Raman spectra of possible corrosion products of iron. *Applied spectroscopy*, 32(6):532–535, 1978.

[87] Tilde de Caro. The ancient metallurgy in sardinia (italy) through a study of pyrometallurgical materials found in the archaeological sites of tharros and montevecchio (west coast of sardinia). *Journal of Cultural Heritage*, 28:65–74, 2017.

[88] Enrico Acquaro and Sabatino Moscati. Gli insediamenti fenici e punici in italia. *Itinerari*, 1, 1988.

[89] Anna Chiara Fariselli et al. Tipologie tombali e rituali funerari a tharros, tra africa e sardegna. *L'Africa romana. Le ricchezze dell'Africa. Risorse, produzioni, scambi. Atti del XVII convegno di studio (Sevilla, 14-17 dicembre 2006), III. Roma: Carocci*, pages 1707–1718, 2008.

[90] Alessio Mezzi, EMMA Angelini, Cristina Riccucci, Sabrina Grassini, Tilde De Caro, Federica Faraldi, and Paolo Bernardini. Micro-structural and microchemical composition of bronze artefacts from tharros (western sardinia, italy). *Surface and interface analysis*, 44(8):958–962, 2012.

[91] Emma Angelini, Francesco Rosalbino, S Grassin, GM Ingo, Tilde DE CARO, et al. Simulation of corrosion processes of buried archaeological bronze artefacts. In *Corrosion of Metallic Heritage Artefacts*, pages 203–218. Elsevier, 2007.

[92] Manuel Morcillo, José M González-Calbet, José Antonio Jiménez, Iván Díaz, J Alcántara, Belén Chico, A Mazarío-Fernández, A Gómez-Herrero, Irene Llorente, and D De la Fuente. Environmental conditions for akaganeite formation in marine atmosphere mild steel corrosion products and its characterization. *Corrosion*, 71(7):872–886, 2015.

[93] Rochelle M Cornell, Udo Schwertmann, et al. *The iron oxides: structure, properties, reactions, occurrences, and uses*, volume 664. Wiley-vch Weinheim, 2003.

[94] D Neff, Enrique Vega, Philippe Dillmann, M Descostes, Ludovic Bellot-Gurlet, and G Béranger. Contribution of iron archaeological artefacts to the estimation of average corrosion rates and the long-term corrosion mechanisms of low-carbon steel buried in soil. In *Corrosion of Metallic Heritage Artefacts*, pages 41–76. Elsevier, 2007.

[95] Emilio Cano, Diana Lafuente, and David M Bastidas. Use of eis for the evaluation of the protective properties of coatings for metallic cultural heritage: a review. *Journal of Solid State Electrochemistry*, 14:381–391, 2010.

[96] EMMA Angelini, P Bianco, Francesco Rosalbino, et al. In-situ polymerization for consolidation and protection of iron artifacts. In *Proceedings of 1st Int. Congress on Science and Technology for the safeguard of cultural heritage in the Mediterranean basin*, pages 759–762, 1995.

[97] Gösta Wranglén. An introduction to corrosion and protection of metals. *Anti-corrosion methods and materials*, 19(11):5–5, 1972.

[98] Robert Abbott Hadfield. The corrosion of iron and steel. *Proceedings of the Royal Society of London. Series A, Containing Papers of a Mathematical and Physical Character*, 101(713):472–486, 1922.